Doctoral Thesis

Fluid-structure interaction approach to thermal residual stress development in laser materials processing

Haram Yeo

Department of Mechanical Engineering

Graduate School of UNIST

2020

Fluid-structure interaction approach to thermal residual stress development in laser materials processing

Haram Yeo

Department of Mechanical Engineering

Graduate School of UNIST

Fluid-structure interaction approach to thermal residual stress development in laser materials processing

A thesis/dissertation
submitted to the Graduate School of UNIST
in partial fulfillment of the
requirements for the degree of
Doctor of Philosophy

Haram Yeo

06. 19. 2020 of submission
Approved by

_____

Advisor
Hyungson Ki

Fluid-structure interaction approach to thermal residual stress development in laser materials processing

Haram Yeo

This certifies that the thesis/dissertation of Haram Yeo is approved.

06. 19. 2020 of submission

signature

_____

Advisor: Hyungson Ki

signature

_____

Sung Youb Kim: Thesis Committee Member #1

signature

_____

Jae Hwa Lee: Thesis Committee Member #2

signature

_____

Jun Choi: Thesis Committee Member #3

signature

_____

Sangwoo So: Thesis Committee Member #4;

signature

Fluid-structure interaction approach to thermal residual stress development in laser materials processing

ABSTRACT

Recently, laser materials processing has attracted attention in the industry due to various advantages. However, in laser processing, thermal residual stresses are inevitably generated and product defects, such as distortions and fractures may occur. Consequently, accurate prediction of residual stresses is very important for improving product quality. In this research, we developed a novel numerical model for computing thermal residual stresses. we focused on fluid-structure interactions (FSI) that occur during melting and solidification by laser processing. The fluid-structure interaction has a significant effect on residual stress development but has been simplified or neglected in traditional numerical models. To verify our numerical method, residual stresses are also experimentally investigated.

In Chapter 1, background and motivation are discussed. Literature reviews and overview of this research are presented. In Chapter 2, a fundamental numerical model for FSI problems is presented. The unified momentum equation is derived from the elastodynamic equation for linear elastic structures and the Navier-Stokes equation for incompressible Newtonian fluids. This numerical method is applied to stationary interface FSI problems. In Chapter 3, the unified momentum equation approach is extended to moving interface FSI problems. The level set method combined with a displacement field extension procedure is used to describe the moving interfaces in a fully Eulerian way. Owing to the way the unified momentum equation is formulated, both the velocity and stress fields can be computed for both the structure and the fluid. In Chapter 4, the numerical model for computing thermal residual stresses is presented based on the unified momentum equation approach. Using this numerical method, the fluid-structure interactions during melting and solidification are naturally considered in the residual stress development. The simple two-dimensional laser melting problem is considered with plane stress assumption to test the proposed numerical model. In Chapter 5, we analyze the laser heat treatment process numerically and experimentally. The unified momentum equation approach is improved to predict actual residual stresses of laser heat treatment process. A three-dimensional numerical model is used, and all major causes of residual stress formation are taken into account. In the experiments, a 2 kW fiber laser with rectangular top-hat profile is used and the processing material is a $50\times30\times8$ mm^3 AH36 carbon steel. The residual stresses are measured using the contour method. In Chapter 6, summary and future works are described. The unified momentum equation approach can be easily applied to other laser materials processing such as laser cladding and laser welding.

TABLE OF CONTENTS

LIST OF FIGURES

LIST OF TABLES

1. Background and motivation

In the modern industry, laser processes are widely used due to its advantages such as high intensity, selective treatment, and minimal deformation [1-6]. Laser processing involves Multiphysics phenomena where melting and solidification occur, thermal stress and fluid flow are developed, microstructures are transformed, and fluid and structure interact. Figure 1 shows the schematic drawing of laser processing. The laser heat source is applied to the surface of specimen and the melt pool is formed. Due to the Marangoni effect, the fluid flow occurs in the melt pool. Usually, the liquid-solid interface is not sharp because of the alloy composition, and the interface exists as a widened region called a mushy zone. The mushy zone is located between the liquid state and solid state of the specimen.

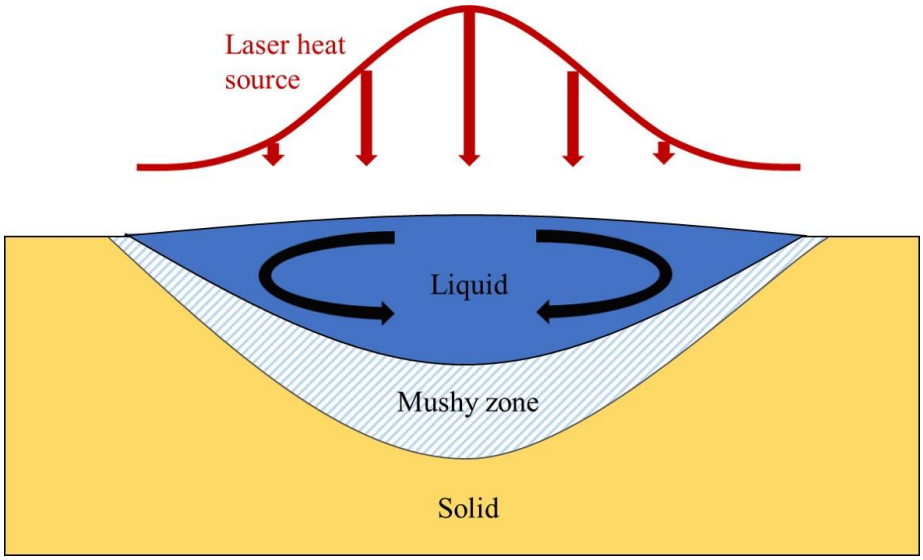

Figure 1. Schematic drawing of laser processing

In order to predict residual stress, it is important to consider all the physical phenomena because they are strongly coupled during the laser processing. However, fluid-structure interaction (FSI) has been ignored in laser processing residual stress simulations because of complexity and difficulty. In Figure 2, the actual in-process image of laser welding experiment is presented. In the laser irradiation area, the liquid state appears, and on the back side there is the mushy zone where liquid and solid coexist. After the laser irradiation is finished, the molten part solidifies, and residual stresses are developed by an elasto-plastic behavior of structure. Accurate prediction of residual stresses around the fusion zone where the material has undergone melting is significant to prevent mechanical defects.

In this study, a novel numerical approach for residual stresses caused by laser processing is proposed. Especially, the research focuses on the laser processing involving material melting and solidification. This numerical model is developed based on the fluid-structure interaction. The laser processing experiments are also performed to validate the numerical results.

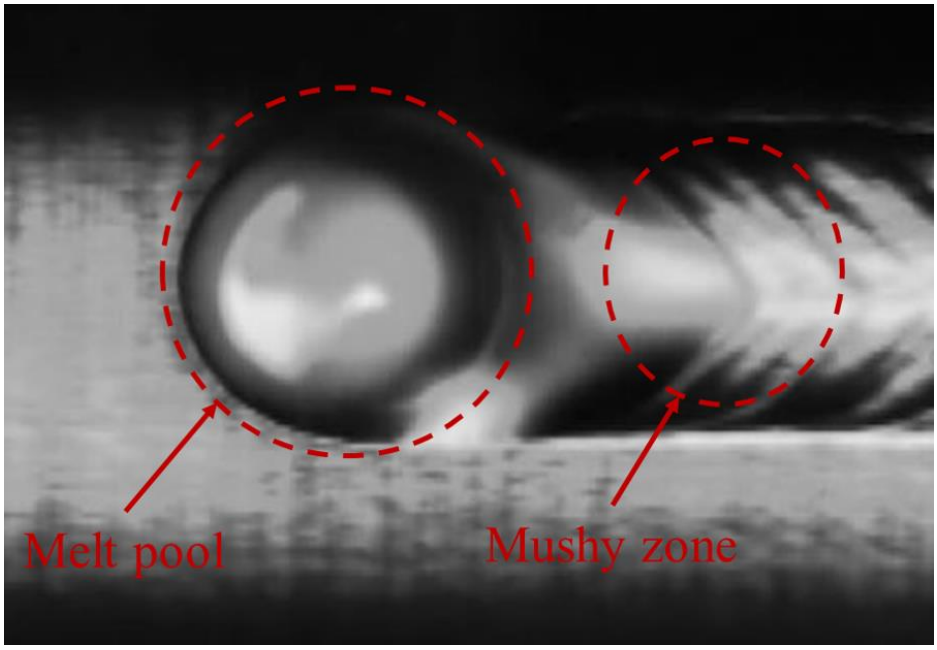

Figure 2. Laser welding experiment where the melt pool and the mushy zone is indicated as red circles.

1.1 Fluid structure interaction (FSI)

1.1.1 FSI coupling method

Fluid-structure interactions are at the heart of many important engineering problems [7-10]. Because of its complexity, the numerical approach is the most practical, and there has been a lot of interest in creating accurate and efficient numerical algorithms [11]. In general, there are two coupling methods for fluid and structure: partitioned method and monolithic method. In the partitioned method, fluid and structure are solved separately using different solvers and the information is transferred through the interface [12-14]. This method has been traditionally preferred because it allows the use of existing codes for each fluid and structure. On the other hand, the monolithic method solves the fluid-structure system with a single numerical algorithm. Although the development of a well-conditioned system is difficult due to the completely different characteristics of fluids and structures, this method is more robust than the partitioned method. Accordingly, many monolithic methods have been developed with various coupling strategies [15-18].

1.1.2 Moving interface

Another important issue is how to handle moving interfaces. Generally, the structure problems are described in a Lagrangian way. In this method, a body-fitted grid which is aligned with the interface is used. On the other hand, the fluid problems are described in a Eulerian way and a fixed grid is used. Figure 3 shows the schematic drawing of the body-fitted grid and the fixed grid. In numerical methods for FSI problem, implementing the moving interface is an important topic. Based on the strategy used to describe the moving interface, it can be divided into several categories including interface tracking methods, Eulerian-Lagrangian methods, and fully Eulerian methods [19].

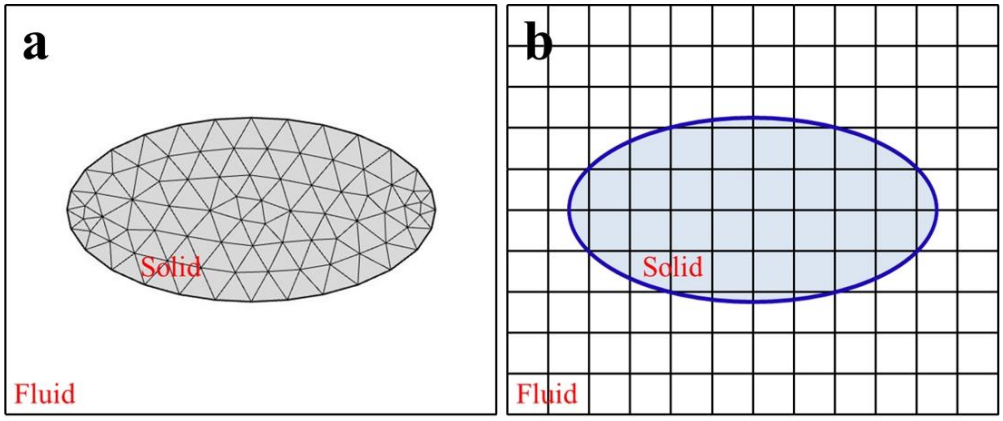

Figure 3. Schematic drawing of two grid types. (a) body-fitted grid, (b) fixed grid.

In the interface tracking methods, the body-fitted grid is employed for the computation. Commonly used method is the arbitrary Lagrangian Eulerian (ALE) method [20-22] where the fluid-structure interface is explicitly tracked, and an artificial domain is introduced for the fluid while the structure is formulated in Lagrangian coordinates. The representative method of the Eulerian-Lagrangian approach is the immersed boundary method [23-25] which was originally developed to compute blood flow in heart valves and the structure is represented by adding a momentum forcing term to the Navier-Stokes equation. In this method, the fluid is described in Eulerian way and the structure is represented in Lagrangian way. Although numerical methods that fall into these numerical categories are traditionally popular and have been successfully applied to many FSI problems, the Lagrangian description for structure requires the re-meshing procedure which is sometimes troublesome and increases the computational cost.

Although not as popular as the other methods, the fully Eulerian methods have recently attracted attention to avoid the difficulty from the grid handling. In the fully Eulerian methods, a single Eulerian coordinate system is used for both fluid and structure, making it easy to consider FSI problems involving large deformation or movement of structure without the mesh generation procedure [19, 26-31]. However, most of the previously performed researches were based on the hyperelastic structure models where relatively soft materials were considered such as biological systems. Moreover, these studies focused primarily on the motions of the fluid-structure interfaces rather than on the internal stress fields developed from the fluid-structure interactions.

1.1.3 Unified momentum equation

The interaction of linear elastic structures with fluids is common in many engineering problems, especially laser processing such as laser heat treatment, laser cladding, and laser welding where the processing material is mainly metal, and during the process, liquid and solid phases interacts around the melt pool. However, there are few fully Eulerian FSI models for linear elastic structures.

In this study, in order to develop the numerical method suitable for computing residual stress caused from laser processing, a novel monolithic fully Eulerian method for FSI problems is proposed by using the unified momentum equation approach [32-35], where the elastodynamic equation for linear elastic structures and the Navier–Stokes equation for incompressible Newtonian fluids are unified into a single velocity-based momentum equation. Gattu and Ki [32] first proposed this approach, and Yeo and Ki improved this method to apply to FSI problems with stationary arbitrarily shaped interfaces [33], thermal residual stresses problems during the thermal processes of metals [34], and FSI problems with moving interfaces involving linear elastic structures [35]. On account of the way the unified momentum equation is formulated, a tight coupling of fluid and structure can be

obtained, and this method can not only simulate the dynamic interactions between fluid and structure, but also calculate the stress fields in both phases. The unified momentum equation can be solved with a suitable numerical method for CFD (Computational Fluid Dynamics), and the SIMPLE algorithm (Semi-Implicit Method for Pressure Linked Equations) is used in this study. The level set method is introduced to capture the moving interface. In order to describe the structure in the Eulerian way, we employed a displacement extrapolation procedure. Various FSI numerical examples and validation problems are considered in Chapter 2 and Chapter 3.

1.2 Residual stress during laser processing

1.2.1 Traditional residual stress prediction method

Although the laser processing has various advantages, the mechanical failures may occur without a deep understanding of residual stress development. However, an accurate prediction of residual stresses is challenging task because complex physical phenomena are strongly coupled. Generally, the thermal residual stress computation consists of three parts: thermal analysis, metallurgical analysis, and mechanical analysis. In thermal analysis and mechanical analysis, energy and stress are computed respectively. In metallurgical analysis, the microstructures of the alloy are investigated. According to the heating and cooling of the material, phase transformations occur, and microstructures change. The solid-state phase transformation plays an important role in the residual stresses. Figure 4 shows the continuous cooling transformation (CCT) diagram of AH36 carbon steel. The phase transformation in the cooling cycle can be determined by using the CCT diagram where the maximum phase fraction and transformation start temperature can be predicted according to the cooling rate.

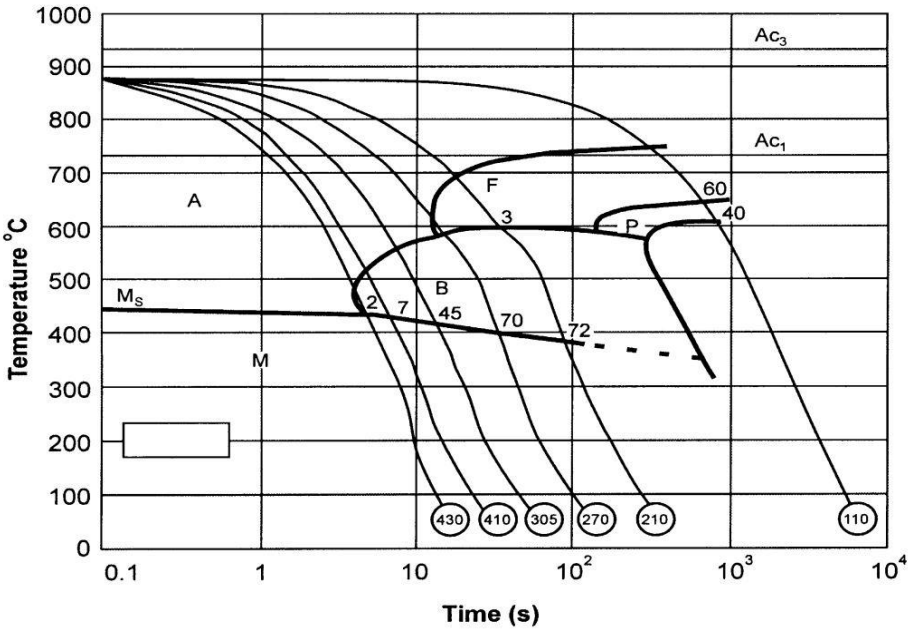

Figure 4. CCT diagram of AH36 carbon steel (from [36])

Traditionally, the finite element model based on the commercial software has been used to compute residual stress in laser processing and successfully applied to laser heat treatment [37-39], laser cladding [40-42], and laser welding [43-45]. In these methods, thermal, metallurgical, and mechanical simulations are sequentially performed. Figure 5. (a) shows the schematic drawing of sequential

calculation. First, the transient temperature history caused by laser irradiation is computed. The thermal analysis results are then applied to the metallurgical analysis and the mechanical analysis to calculate the residual stresses. Due to the separate calculations of each numerical analysis, there is a limit to accurately predicting residual stresses. Furthermore, in existing numerical models, fluid-structure interactions during melting and solidification are neglected in the mechanical analysis.

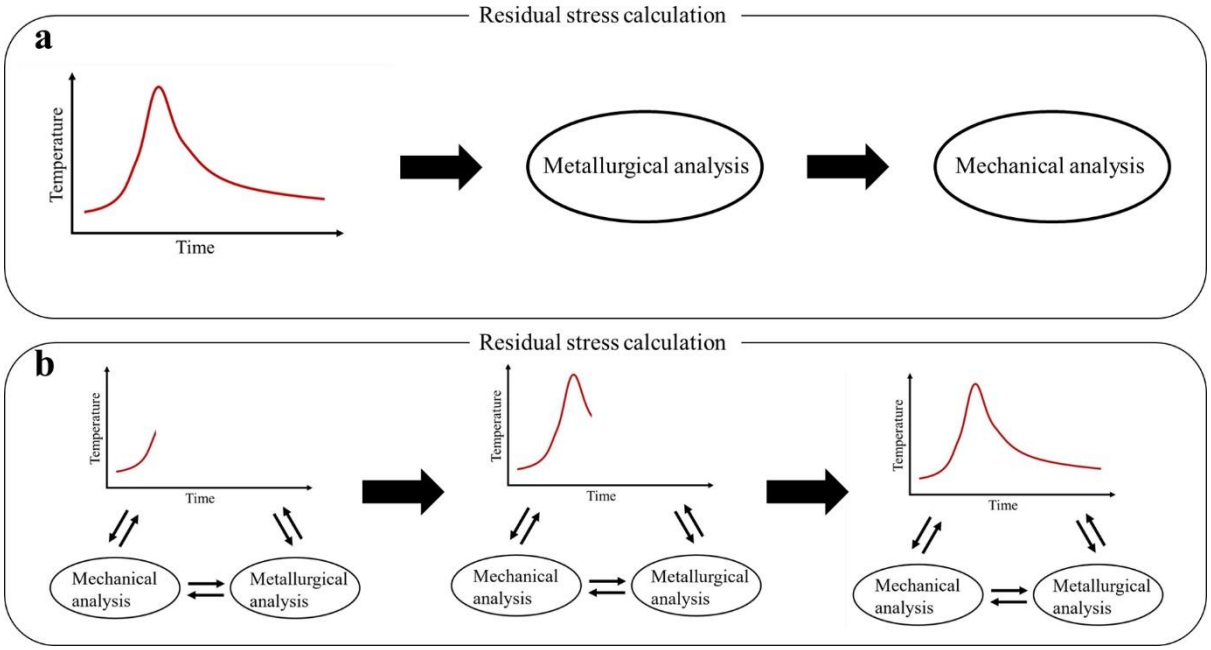

Figure 5. Schematic drawing of residual stress calculation. (a) sequential calculation, (b) simultaneous calculation

1.2.2 Residual stress computation using unified momentum equation

In order to obtain high precision residual stresses caused by laser processing, the development of fully coupled numerical model is necessary. We extend the unified momentum equation approach for FSI to a numerical model for residual stress computation. In this numerical model, thermal-metallurgical-mechanical analysis are performed simultaneously and interact each other. Residual stresses are computed following the actual in-process stress development during laser processing, so the intermediate processes such as melting and solidification, existence of mushy zone, and fluid-structure interaction are taken into account. Figure 5. (b) shows the schematic drawing of simultaneous calculation. In thermal analysis, an enthalpy-based energy equation that also includes the convection due to melt flow is solved. In metallurgical analysis, the microstructure changes are predicted by using the CCT diagram. In mechanical analysis, all the main causes of residual stress formation such as thermal expansion, plasticity, and solid-state phase transformation are considered.

By using the unified momentum equation, the whole solid-liquid system including the mushy zone is treated as a single continuum, and the interactions between them are naturally taken into account in a monolithic way. To experimentally investigate residual stresses, laser processing experiments of AH36 carbon steel are conducted. The residual stress is measured by using the contour method and microstructures are examined by the optical microscopy. The numerical and experimental results of laser processing are compared in Chapter 4 and Chapter 5.

2. Unified momentum equation approach for stationary interface FSI problems

This chapter includes the published contents:

H. Yeo, H. Ki*, Commun. Comput. Phys. 22 (2017) 39-63, Copyright © 2017 Global-Science Press.

This chapter presents a fundamental numerical model of the unified momentum equation and considers stationary interface FSI problems.

2.1. Mathematical model

2.1.1. Fluid equation

The governing equations for incompressible Newtonian fluids consist of the Navier-Stokes equation and the continuity equation as follows:

$$\frac{D(\rho\mathbf{u})}{Dt} = \nabla\cdot\boldsymbol{\sigma}_f + \mathbf{f} \tag{1}$$

$$\nabla\cdot\mathbf{u} = 0 \tag{2}$$

Here, ρ is density, $\mathbf{u}$ is the velocity vector, $\mathbf{f}$ is the body force, and the stress tensor $\boldsymbol{\sigma}_f$ is written as

$$\boldsymbol{\sigma}_f = -p\mathbf{I} + \eta\left(\nabla\mathbf{u} + \nabla\mathbf{u}^T\right) \tag{3}$$

where p, $\mathbf{I}$, and η are the pressure, identity tensor, and viscosity, respectively. From Eqs. (1), (2), and (3), the following momentum equation for fluids is obtained.

$$\frac{\partial(\rho\mathbf{u})}{\partial t} + \nabla\cdot(\rho\mathbf{u}\mathbf{u}) = \nabla\cdot\left(\eta\left(\nabla\mathbf{u} + \nabla\mathbf{u}^T\right) - p\mathbf{I}\right) + \mathbf{f} \tag{4}$$

2.1.2. Structure equation

For structures, the elastodynamic equation is used.

$$\frac{D(\rho\mathbf{u})}{Dt} = \nabla\cdot\boldsymbol{\sigma}_s + \mathbf{f} \tag{5}$$

The stress tensor of linear elastic structures, $\boldsymbol{\sigma}_s$ is written as

$$\boldsymbol{\sigma}_s = \mu\left(\nabla\mathbf{d} + \nabla\mathbf{d}^T\right) + \left(\lambda\,\mathrm{Tr}(\nabla\mathbf{d} + \nabla\mathbf{d}^T)\right)\mathbf{I} \tag{6}$$

where Tr is the trace, **d** is the displacement vector, and μ and λ are Lame constants, which are written in terms of Young's modulus (E) and Poisson's ratio (ν) as

$$\mu = \frac{E}{2(1+\nu)} \quad \text{and} \quad \lambda = \frac{E\nu}{(1+\nu)(1-2\nu)}. \tag{7}$$

To obtain a velocity-based momentum equation for structures, the displacement vector **d** is expressed in terms of the velocity. For each computational cell, the displacement is obtained by integrating the velocity over time where a first-order implicit scheme is used as follow:

$$\mathbf{d} = \int_{t^o}^{t} \mathbf{u}\,dt + \mathbf{d}^o \approx \mathbf{u}\Delta t + \mathbf{d}^o \tag{8}$$

The superscript o represents the previous time step. From Eqs. (5), (6), and (8), the momentum equation for structures is expressed as.

$$\frac{\partial(\rho\mathbf{u})}{\partial t} + \nabla\cdot(\rho\mathbf{u}\mathbf{u}) = \nabla\cdot\left(\mu\Delta t\left(\nabla\mathbf{u} + \nabla\mathbf{u}^T\right) + \lambda\Delta t\left(\nabla\cdot\mathbf{u}\right)\mathbf{I} + \mathbf{b}\right) + \mathbf{f} \tag{9}$$

where

$$\mathbf{b} = \mu\left(\nabla\mathbf{d}^o + \nabla\mathbf{d}^{oT}\right) + \lambda\left(\nabla\cdot\mathbf{d}^o\right)\mathbf{I}. \tag{10}$$

2.1.3. Unified momentum equation

Observing Eqs. (4) and (9) closely, we can notice that they are very similar. This momentum equations for both phases can be cast into a unified momentum equation.

$$\frac{\partial(\rho\mathbf{u})}{\partial t} + \nabla\cdot(\rho\mathbf{u}\mathbf{u}) = \nabla\cdot\left(\bar{\mu}\left(\nabla\mathbf{u} + \nabla\mathbf{u}^T\right) + \bar{\lambda}\left(\nabla\cdot\mathbf{u}\right)\mathbf{I} + \bar{\mathbf{b}}\right) + \mathbf{f} \tag{11}$$

where $\bar{\mu}$, $\bar{\lambda}$, and $\bar{\mathbf{b}}$ are given as

$$\bar{\mu} = \begin{cases} \eta, & \text{for fluids} \\ \mu\Delta t, & \text{for solids} \end{cases}, \tag{12}$$

$$\bar{\lambda} = \begin{cases} 0, & \text{for fluids} \\ \lambda\Delta t, & \text{for solids} \end{cases}, \tag{13}$$

$$\bar{\mathbf{b}} = \begin{cases} -p\mathbf{I}, & \text{for fluids} \\ \mu\left(\nabla\mathbf{d}^o + \nabla\mathbf{d}^{oT}\right) + \lambda\left(\nabla\cdot\mathbf{d}^o\right)\mathbf{I}, & \text{for solids} \end{cases}. \tag{14}$$

The above equation is highly discontinuous because the properties change sharply at the fluid–structure interface. Therefore, material properties are smoothed out using the level set function (ϕ) [46], which is defined as the signed normal distance from the interface as follows.

$$\phi = \begin{cases} +\text{distance}, & \text{for fluids} \\ 0, & \text{for interfaces} \\ -\text{distance}, & \text{for solids} \end{cases} \tag{15}$$

The smoothed Heaviside function is then defined as

$$\mathrm{H}_\alpha(\phi) = \begin{cases} 1, & \text{if } \phi > \alpha \\ \frac{1}{2}\left(1 + \frac{\phi}{\alpha} + \frac{1}{\pi}\sin\left(\frac{\pi\phi}{\alpha}\right)\right) & \text{if } |\phi| \le \alpha \\ 0, & \text{if } \phi < -\alpha \end{cases} . \tag{16}$$

The density and Eqs. (12)-(14) are then smoothed over the fluid-structure interface as follows:

$$\begin{aligned} \rho &= \rho_{\text{solid}} + (\rho_{\text{fluid}} - \rho_{\text{solid}})\mathrm{H}_\alpha(\phi) \\ \bar{\mu} &= \mu\Delta t + (\eta - \mu\Delta t)\mathrm{H}_\alpha(\phi) \\ \bar{\lambda} &= \lambda\Delta t(1 - \mathrm{H}_\alpha(\phi)) \\ \bar{\mathbf{b}} &= \left\{\frac{\bar{\mu}}{\Delta t}\left(\nabla\mathbf{d}^o + \nabla\mathbf{d}^{oT}\right) + \frac{\bar{\lambda}}{\Delta t}\left(\nabla\cdot\mathbf{d}^o\right)\mathbf{I}\right\}(1 - \mathrm{H}_\alpha(\phi)) + (-p\mathbf{I})\mathrm{H}_\alpha(\phi) \end{aligned} \tag{17}$$

Note that the smeared interface has a thickness of 2α, and the pressure term of the fluid and the displacement term of the structure coexist within the smeared interface region. In this study, $\alpha = 1.5\Delta x$ was used. By using the unified momentum equation, the interfacial conditions such as the velocity continuity and the stress continuity are automatically satisfied.

2.2. Numerical algorithm

The unified momentum equation (11) looks similar to the Navier–Stokes equation, and can be solved using a proper numerical algorithm for CFD. The continuity equation (Eq. (2)) is solved only in the fluid region because the pressure is not defined in the solid region. In this study, the unified momentum equation is discretized using a finite volume approach on a uniform staggered grid. To explain the discretization procedure, the x-component of Eq. (11) will be considered in two dimensions.

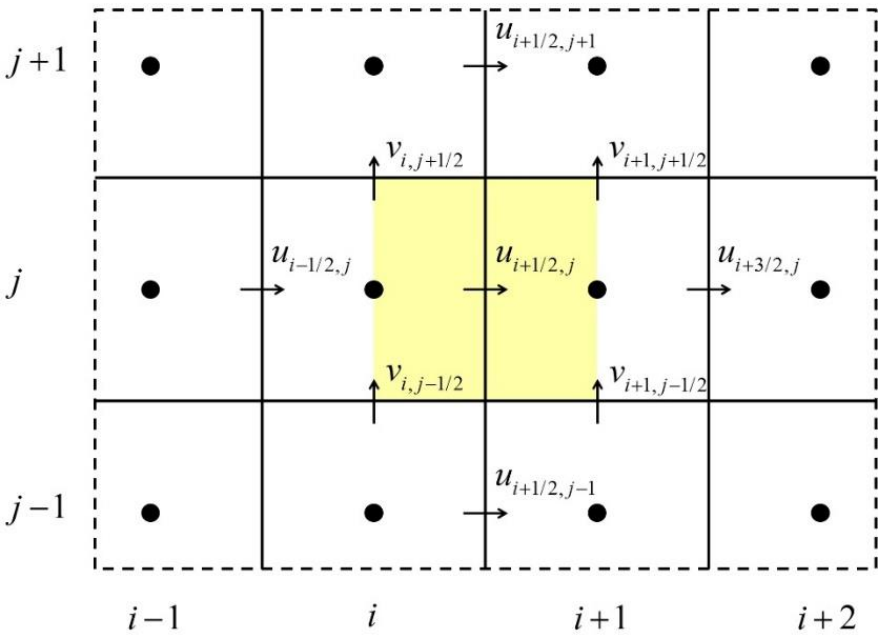

Figure 6. Schematic drawing of a uniform staggered grid where a u-velocity control volume is represented as a yellow square.

Figure 6 shows a schematic drawing of a uniform staggered grid where scalar variables are defined at the cell centers (black solid circles), and the velocities are defined at the cell faces (arrows). The yellow square indicates a u-velocity control volume at (i+1/2, j). Integrating the x-component of the unified momentum equation (Eq. (11)) over the control volume, the following equation is obtained.

$$\frac{\partial(\rho u)_{i+1/2,j}}{\partial t}\Delta V_{i+1/2,j} = F_{i+1,j} - F_{i,j} + F_{i+1/2,j+1/2} - F_{i+1/2,j-1/2} + f_x \tag{18}$$

Here, ΔV is the volume of the cell, f_x is the x-component of the external body force, which is zero in this work, and F represents the momentum fluxes at the respective cell faces:

$$
\begin{aligned}
F_{i+1,j} &= \left\{ \left(-\rho uu\right) + \left(2\bar{\mu} + \bar{\lambda}\right)\left(\frac{\partial u}{\partial x}\right) + \bar{\lambda}\left(\frac{\partial v}{\partial y}\right) + \bar{b} \right\}_{i+1,j} \Delta A_{i+1,j} \\
F_{i,j} &= \left\{ \left(-\rho uu\right) + \left(2\bar{\mu} + \bar{\lambda}\right)\left(\frac{\partial u}{\partial x}\right) + \bar{\lambda}\left(\frac{\partial v}{\partial y}\right) + \bar{b} \right\}_{i,j} \Delta A_{i,j} \\
F_{i+1/2,j+1/2} &= \left\{ \left(-\rho vu\right) + \bar{\mu}\left(\frac{\partial u}{\partial y} + \frac{\partial v}{\partial x}\right) + \bar{b} \right\}_{i+1/2,j+1/2} \Delta A_{i+1/2,j+1/2} \\
F_{i+1/2,j-1/2} &= \left\{ \left(-\rho vu\right) + \bar{\mu}\left(\frac{\partial u}{\partial y} + \frac{\partial v}{\partial x}\right) + \bar{b} \right\}_{i+1/2,j-1/2} \Delta A_{i+1/2,j-1/2}
\end{aligned}
\tag{19}
$$

Here, ΔA is the cell face area. Eqs. (18) and (19) can be easily discretized and following discretized equation is obtained:

$$
\begin{aligned}
&\frac{(\rho u)_{i+1/2,j} - (\rho u)^{o}_{i+1/2,j}}{\Delta t} \Delta V_{i+1/2,j} \\
&= \left\{ (-\rho uu)_{i+1,j} + \left(2\bar{\mu}_{i+1,j} + \bar{\lambda}_{i+1,j}\right)\left(\frac{u_{i+3/2,j} - u_{i+1/2,j}}{\Delta x}\right) + \bar{\lambda}_{i+1,j}\left(\frac{v_{i+1,j+1/2} - v_{i+1,j-1/2}}{\Delta y}\right) + \bar{b}_{i+1,j} \right\} \Delta A_{i+1,j} \\
&- \left\{ \left(-\rho uu\right)_{i,j} + \left(2\bar{\mu}_{i,j} + \bar{\lambda}_{i,j}\right)\left(\frac{u_{i+1/2,j} - u_{i-1/2,j}}{\Delta x}\right) + \bar{\lambda}_{i,j}\left(\frac{v_{i,j+1/2} - v_{i,j-1/2}}{\Delta y}\right) + \bar{b}_{i,j} \right\} \Delta A_{i,j} \\
&+ \left\{ \left(-\rho vu\right)_{i+1/2,j+1/2} + \bar{\mu}_{i+1/2,j+1/2}\left(\frac{u_{i+1/2,j+1} - u_{i+1/2,j}}{\Delta y} + \frac{v_{i+1,j+1/2} - v_{i,j+1/2}}{\Delta x}\right) + \bar{b}_{i+1/2,j+1/2} \right\} \Delta A_{i+1/2,j+1/2} \\
&- \left\{ \left(-\rho vu\right)_{i+1/2,j-1/2} + \bar{\mu}_{i+1/2,j-1/2}\left(\frac{u_{i+1/2,j} - u_{i+1/2,j-1}}{\Delta y} + \frac{v_{i+1,j-1/2} - v_{i,j-1/2}}{\Delta x}\right) + \bar{b}_{i+1/2,j-1/2} \right\} \Delta A_{i+1/2,j-1/2}
\end{aligned}
\tag{20}
$$

Here, the second-order central difference scheme for space and the first-order backward Euler scheme for time are used.

The discretized x-component momentum equation (20) can be written as

$$
a_{i+1/2,j} u_{i+1/2,j} = \sum_{nb} a_{nb} u_{nb} + \left\{ p_{i,j}\, \mathrm{H}_{\alpha}\left(\phi_{i,j}\right) - p_{i+1,j}\, \mathrm{H}_{\alpha}\left(\phi_{i+1,j}\right) \right\} \Delta A_{i+1/2,j} + S_{i+1/2,j} \,, \tag{21}
$$

where

$$
\begin{aligned}
S_{i+1/2,j} &= \frac{(\rho u)^{o}_{i+1/2,j}}{\Delta t}\Delta V_{i+1/2,j} + \bar{\lambda}_{i+1,j}\left(\frac{v_{i+1,j+1/2}-v_{i+1,j-1/2}}{\Delta y}\right)\Delta A_{i+1,j} - \bar{\lambda}_{i,j}\left(\frac{v_{i,j+1/2}-v_{i,j-1/2}}{\Delta y}\right)\Delta A_{i,j} \\
&+ \bar{\mu}_{i+1/2,j+1/2}\left(\frac{v_{i+1,j+1/2}-v_{i,j+1/2}}{\Delta x}\right)\Delta A_{i+1/2,j+1/2} - \bar{\mu}_{i+1/2,j-1/2}\left(\frac{v_{i+1,j-1/2}-v_{i,j-1/2}}{\Delta x}\right)\Delta A_{i+1/2,j-1/2} \\
&+ \left\{\frac{\left(2\bar{\mu}_{i+1,j}+\bar{\lambda}_{i+1,j}\right)}{\Delta t}\left(\frac{d^{o}_{x,(i+3/2,j)}-d^{o}_{x,(i+1/2,j)}}{\Delta x}\right)+\frac{\bar{\lambda}_{i+1,j}}{\Delta t}\left(\frac{d^{o}_{y,(i+1,j+1/2)}-d^{o}_{y,(i+1,j-1/2)}}{\Delta y}\right)\right\}\left(1-H_{\alpha}\left(\phi_{i+1,j}\right)\right)\Delta A_{i+1,j} \\
&- \left\{\frac{\left(2\bar{\mu}_{i,j}+\bar{\lambda}_{i,j}\right)}{\Delta t}\left(\frac{d^{o}_{x,(i+1/2,j)}-d^{o}_{x,(i-1/2,j)}}{\Delta x}\right)+\frac{\bar{\lambda}_{i,j}}{\Delta t}\left(\frac{d^{o}_{y,(i,j+1/2)}-d^{o}_{y,(i,j-1/2)}}{\Delta y}\right)\right\}\left(1-H_{\alpha}\left(\phi_{i,j}\right)\right)\Delta A_{i,j} \\
&+ \left\{\frac{\bar{\mu}_{i+1/2,j+1/2}}{\Delta t}\left(\frac{d^{o}_{x,(i+1/2,j+1)}-d^{o}_{x,(i+1/2,j)}}{\Delta y}+\frac{d^{o}_{y,(i+1,j+1/2)}-d^{o}_{y,(i,j+1/2)}}{\Delta x}\right)\right\}\left(1-H_{\alpha}\left(\phi_{i+1/2,j+1/2}\right)\right)\Delta A_{i+1/2,j+1/2} \\
&- \left\{\frac{\bar{\mu}_{i+1/2,j-1/2}}{\Delta t}\left(\frac{d^{o}_{x,(i+1/2,j)}-d^{o}_{x,(i+1/2,j-1)}}{\Delta y}+\frac{d^{o}_{y,(i+1,j-1/2)}-d^{o}_{y,(i,j-1/2)}}{\Delta x}\right)\right\}\left(1-H_{\alpha}\left(\phi_{i+1/2,j-1/2}\right)\right)\Delta A_{i+1/2,j-1/2}
\end{aligned}
, \quad (22)
$$

$$
\sum\nolimits_{nb} a_{nb}u_{nb} = a_{i+3/2,j}u_{i+3/2,j} + a_{i-1/2,j}u_{i-1/2,j} + a_{i+1/2,j+1}u_{i+1/2,j+1} + a_{i+1/2,j-1}u_{i+1/2,j-1}, \quad (23)
$$

in which

$$
\begin{aligned}
a_{i+3/2,j} &= \left\{\frac{\left(2\bar{\mu}_{i+1,j}+\bar{\lambda}_{i+1,j}\right)}{\Delta x}+C_{i+1,j}\right\}\Delta A_{i+1,j} \\
a_{i-1/2,j} &= \left\{\frac{\left(2\bar{\mu}_{i,j}+\bar{\lambda}_{i,j}\right)}{\Delta x}+C_{i,j}\right\}\Delta A_{i,j} \\
a_{i+1/2,j+1} &= \left\{\frac{\bar{\mu}_{i+1/2,j+1/2}}{\Delta y}+C_{i+1/2,j+1/2}\right\}\Delta A_{i+1/2,j+1/2} \\
a_{i+1/2,j-1} &= \left\{\frac{\bar{\mu}_{i+1/2,j-1/2}}{\Delta y}+C_{i+1/2,j-1/2}\right\}\Delta A_{i+1/2,j-1/2}
\end{aligned}
, \quad (24)
$$

and

$$
a_{i+1/2,j} = a_{i+3/2,j} + a_{i-1/2,j} + a_{i+1/2,j+1} + a_{i+1/2,j-1} + \frac{\rho_{i+1/2,j}}{\Delta t}\Delta V_{i+1/2,j}. \quad (25)
$$

Here, C in Eq. (24) represents the discretized convection term. In the same way, the y-component momentum equation is discretized and written in the following form.

$$
a_{i,j+1/2}v_{i,j+1/2} = \sum\nolimits_{nb} a_{nb}v_{nb} + \left(p_{i,j}\,\mathrm{H}_{\alpha}\left(\phi_{i,j}\right) - p_{i,j+1}\,\mathrm{H}_{\alpha}\left(\phi_{i,j+1}\right)\right)\Delta A_{i,j+1/2} + S_{i,j+1/2} \quad (26)
$$

The continuity equation for the fluid phase (Eq. (2)) is also discretized in a finite volume framework as follows:

$$
(u\Delta A)_{i+1/2,j} - (u\Delta A)_{i-1/2,j} + (v\Delta A)_{i,j+1/2} - (v\Delta A)_{i,j-1/2} = 0. \quad (27)
$$

In this study, the discretized momentum and continuity equations (Eqs. (21), (26), and (27)) are solved using the semi-implicit method for pressure linked equations (SIMPLE) algorithm [47]. In the SIMPLE algorithm, the discretized momentum equations (Eqs. (21) and (26)) are solved using an estimated pressure field p^*, and u^* and v^* are obtained. These intermediate pressure and velocity values are corrected by solving the pressure correction equation,

$$a_{i,j}p'_{i,j} = a_{i+1,j}p'_{i+1,j} + a_{i-1,j}p'_{i-1,j} + a_{i,j+1}p'_{i,j+1} + a_{i,j-1}p'_{i,j-1} + b_{i,j} \tag{28}$$

which is derived from the combination of Eqs. (21), (26), and (27). Here,

$$\begin{aligned}
&a_{i,j} = a_{i+1,j} + a_{i-1,j} + a_{i,j+1} + a_{i,j-1}, \\
&a_{i+1,j} = \frac{\left(\Delta A_{i+1/2,j}\right)^2}{\left(a_{i+1/2,j}\right)_f}, \quad a_{i-1,j} = \frac{\left(\Delta A_{i-1/2,j}\right)^2}{\left(a_{i-1/2,j}\right)_f}, \\
&a_{i,j+1} = \frac{\left(\Delta A_{i,j+1/2}\right)^2}{\left(a_{i,j+1/2}\right)_f}, \quad a_{i,j-1} = \frac{\left(\Delta A_{i,j-1/2}\right)^2}{\left(a_{i,j-1/2}\right)_f}, \\
&b_{i,j} = u^*_{i-1/2,j}\Delta A_{i-1/2,j} - u^*_{i+1/2,j}\Delta A_{i+1/2,j} + v^*_{i,j-1/2}\Delta A_{i,j-1/2} - v^*_{i,j+1/2}\Delta A_{i,j+1/2}
\end{aligned} \tag{29}$$

This pressure correction equation is solved in the fluid and smeared interface regions because the continuity constraint is only required for a fluid. Note that the terms with the subscript *f* are evaluated using the fluid properties. Once the pressure correction p' is obtained from Eq. (28), p^*, u^*, and v^* are corrected as follows:

$$p = p^* + p' \tag{30}$$

$$u_{i+1/2,j} = u^*_{i+1/2,j} + \frac{\Delta A_{i+1/2,j}}{a_{i+1/2,j}}\left\{p'_{i,j}\,\mathrm{H}_\alpha\left(\phi_{i,j}\right) - p'_{i+1,j}\,\mathrm{H}_\alpha\left(\phi_{i+1,j}\right)\right\} \tag{31}$$

$$v_{i,j+1/2} = v^*_{i,j+1/2} + \frac{\Delta A_{i,j+1/2}}{a_{i,j+1/2}}\left\{p'_{i,j}\,\mathrm{H}_\alpha\left(\phi_{i,j}\right) - p'_{i,j+1}\,\mathrm{H}_\alpha\left(\phi_{i,j+1}\right)\right\} \tag{32}$$

The overall algorithm is shown in Figure 7.

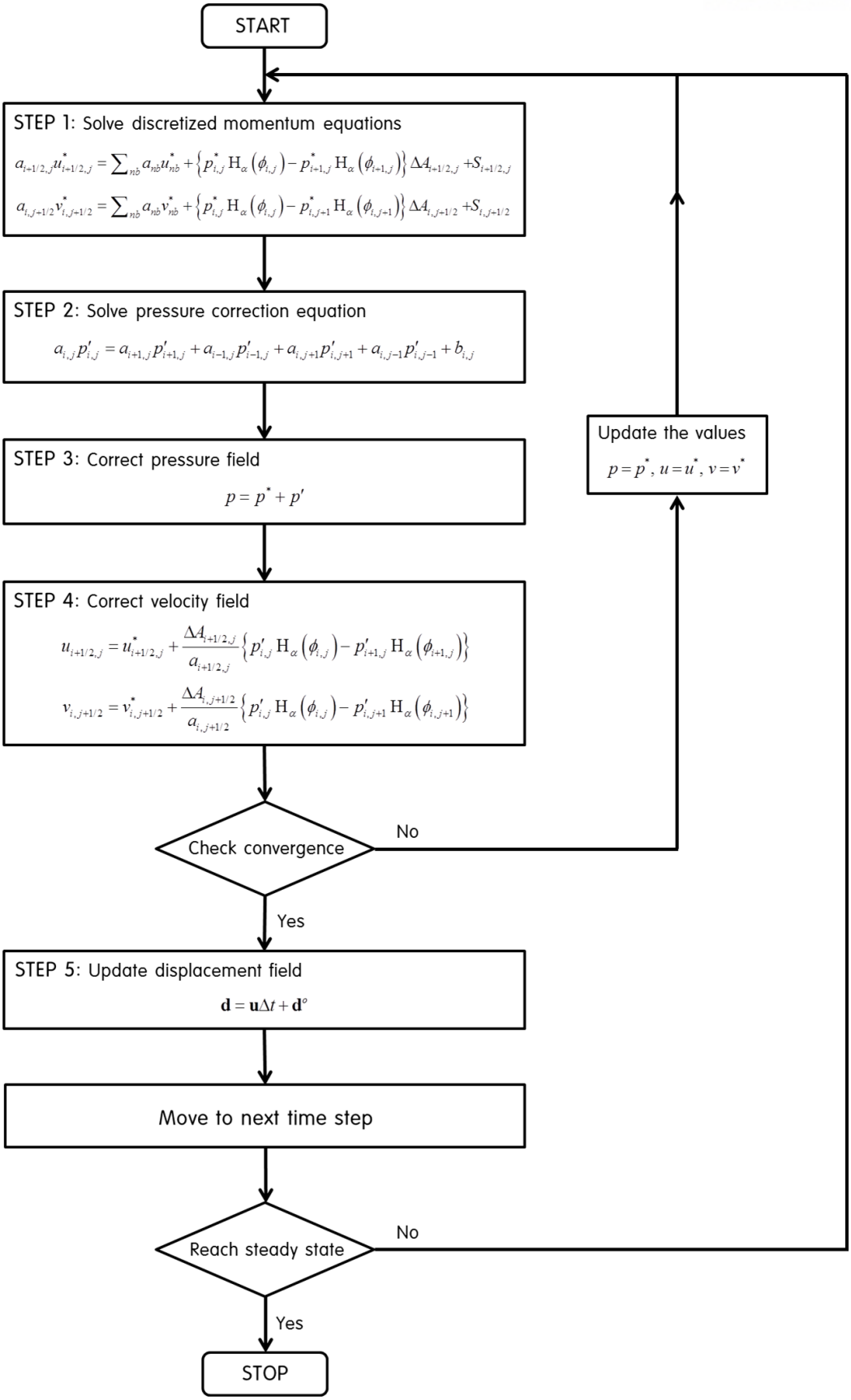

Figure 7. The SIMPLE algorithm applied to the unified momentum equation

2.3. Numerical examples

In this section, three stationary interface FSI problems are simulated on a uniform Cartesian grid. Here, a shifted Heaviside function of $h_\alpha(\phi) \equiv H_\alpha(\phi+\alpha)$ is used instead of the original one given in Eq. (16).

2.3.1. Lid-driven cavity flow inside a solid container (square cavity)

A 0.12 m × 0.12 m square cavity is located inside a 0.2 m × 0.16 m solid. The shape of cavity is fixed, and the container-structure boundary is stationary. The fluid flow is driven by a lid moving at a constant velocity of 8.333×10^{-3} m/s. The outer boundary of solid container is roller supported. Figure 8 shows a schematic of the problem. The fluid is assumed as water, which has a density of 1000 kg/m^3 and a viscosity of 1×10^{-3} kg/m·s. The Reynolds number of the problem is 1000. The solid container is made of aluminum, which has a density of 2700 kg/m^3, Young's modulus of 6.9×10^{10} N/m^2, and Poisson's ratio of 0.33. In this problem, 500 × 400 grid and time step of 0.005 s are used.

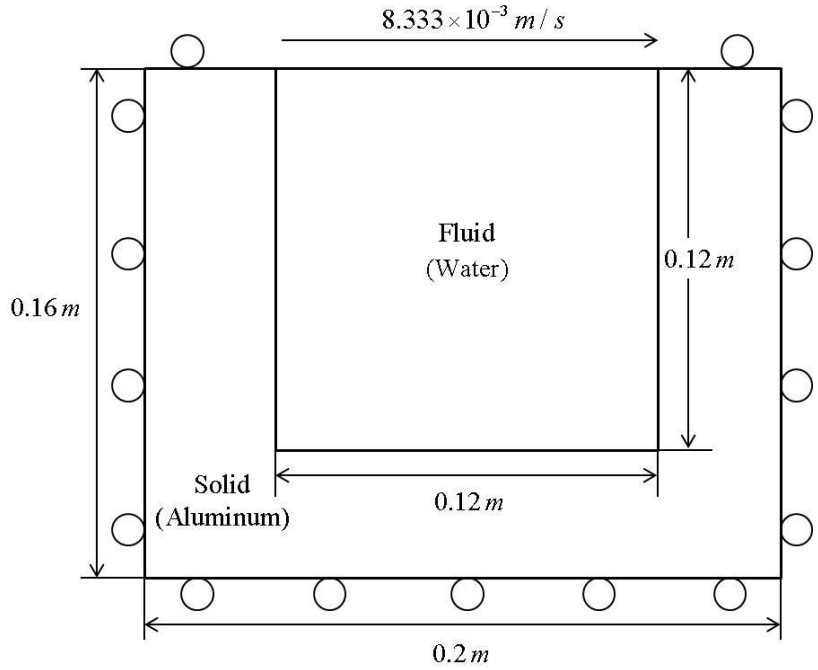

Figure 8. The schematic of the lid-driven rectangular cavity flow problem

Figure 9 ~ Figure 11 show the temporal evolution of stress distributions for both fluid and structure until the steady-state is reached. The normal stresses in x- and y-directions are presented in Figure 9 and Figure 10, respectively. As shown in the figures, stresses are generated starting from the upper

right corner of the interface due to the flow direction. Over time, a circularly shaped stress distribution appears inside a fluid region, indicating that a circular flow field is being developed there. As expected from these figures, stress continuity is clearly observed at the interface. At the vertical interfaces, the normal stress in the x-direction (σ_{xx}) is continuous along the x-direction; at the horizontal interface, the normal stress in the y-direction (σ_{yy}) is also continuous along the y-direction. Figure 11 presents shear stress distributions. Similar to the normal stress distributions, shear stress is the largest at the upper right corner of the interface, where the flow suddenly changes direction at the wall and a large shear stress is developed. Also, because the flow is generated by the moving lid at the top, shear stress is more pronounced right below the moving lid. From the figure, it can be observed that the stress field inside the solid container is fully established over time, confirming that the flow induced stress is well transferred to the structure by the presented algorithm.

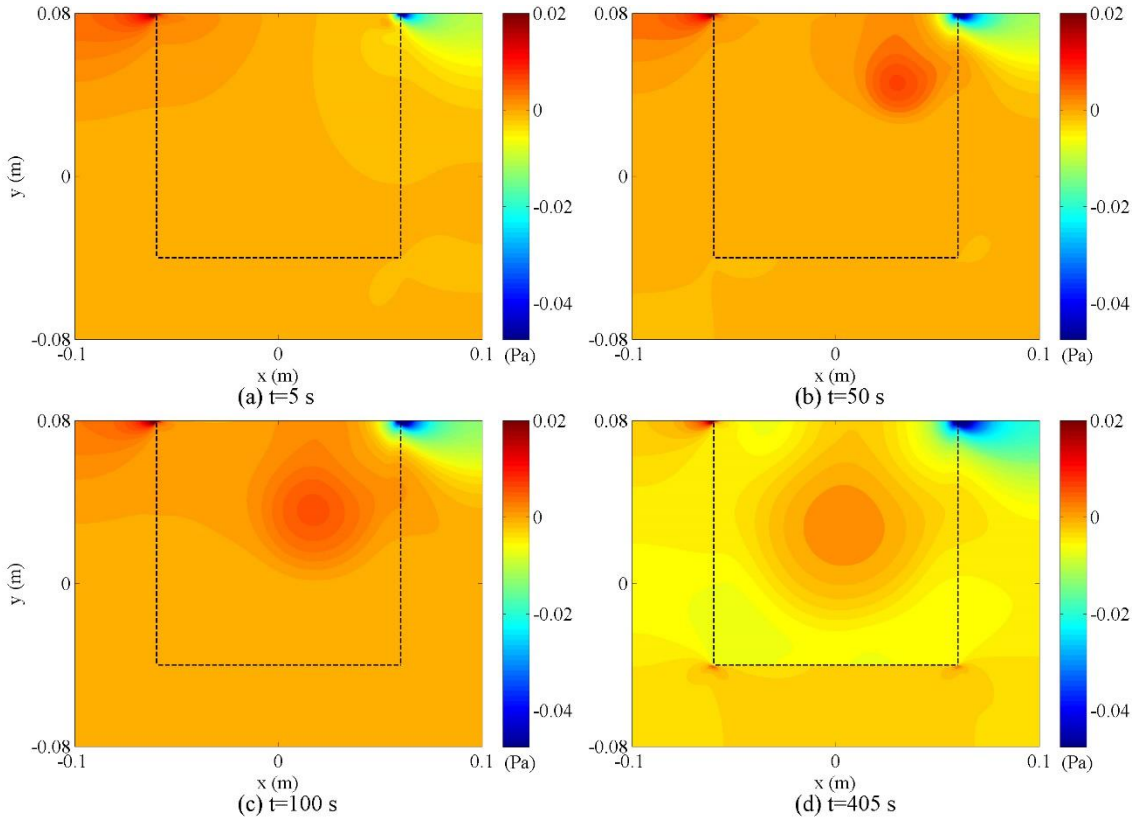

Figure 9. Evolution of normal stress (σ_{xx}): (a) t=5 s, (b) t=50 s, (c) t=100 s, and (d) t=405 s (steady-state)

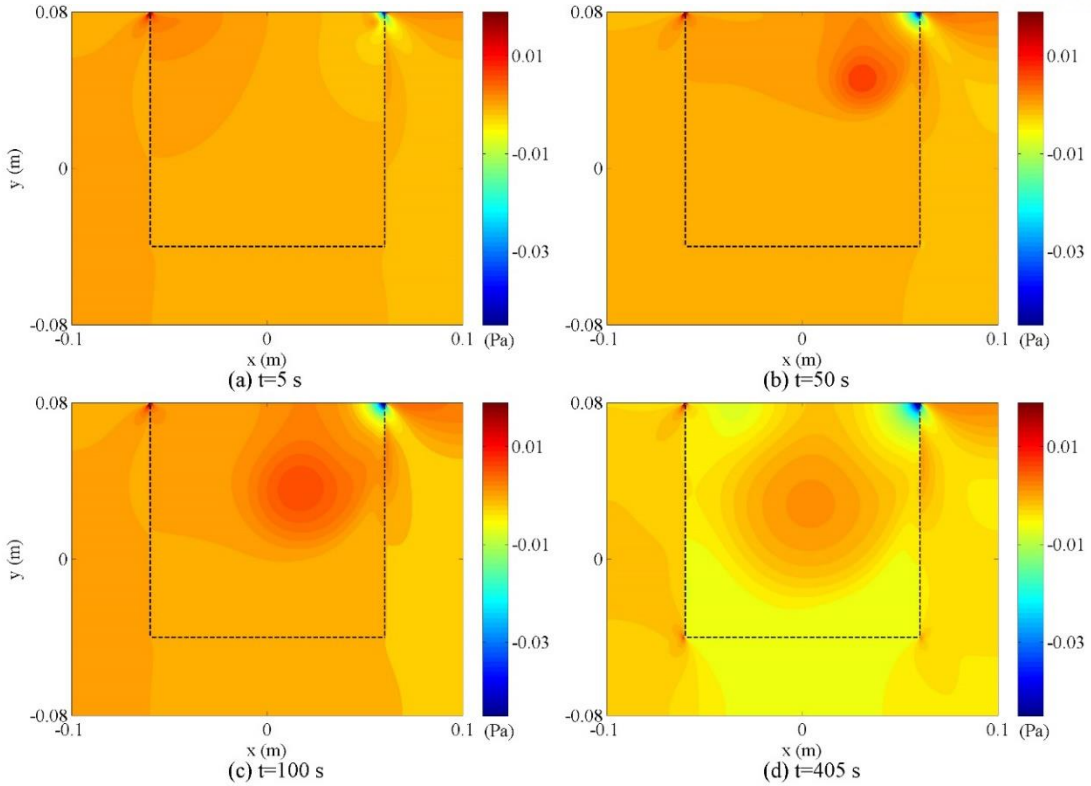

Figure 10. Evolution of normal stress (σ_{yy}): (a) t=5 s, (b) t=50 s, (c) t=100 s, and (d) t=405 s (steady-state)

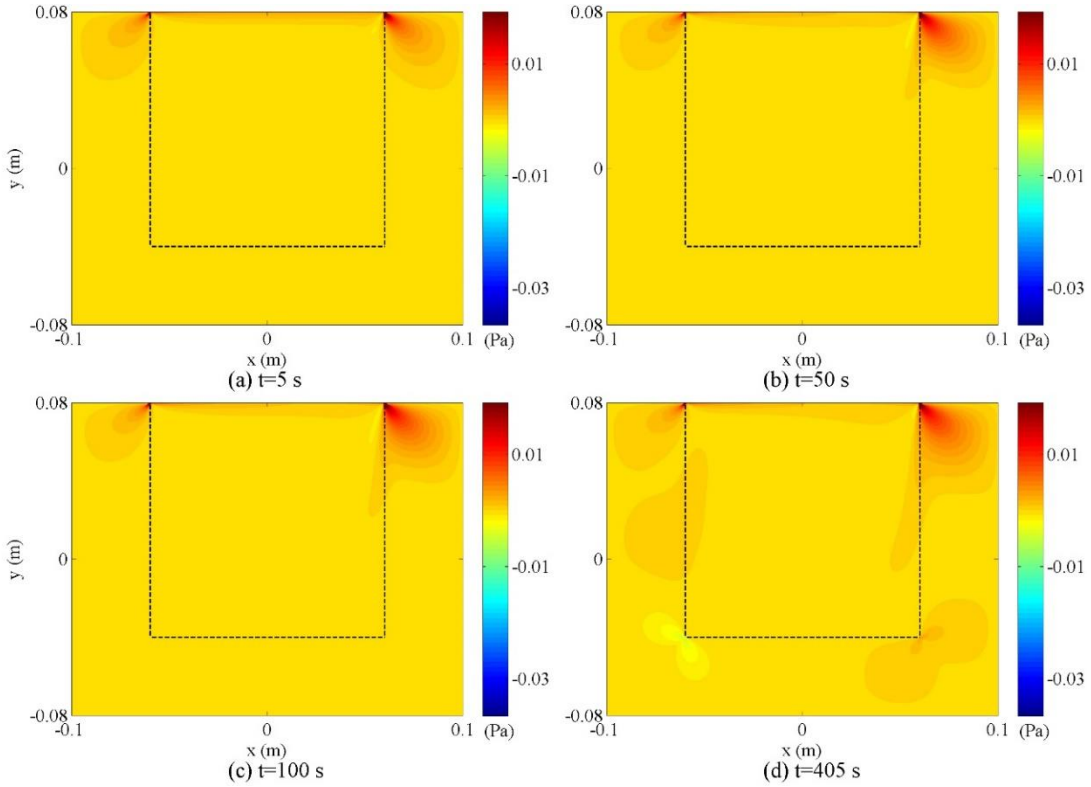

Figure 11. Evolution of shear stress (σ_{xy}): (a) t=5 s, (b) t=50 s, (c) t=100 s, and (d) t=405 s (steady-state)

The streamline distributions for both phases are presented in Figure 12. The velocity of the solid region is extremely small compared to the fluid velocity, but it can still define the streamline. Vorticity development is obviously shown in the fluid domain. Initially, the primary vortex is formed, and two secondary vortices are developed in the bottom-left and bottom-right corners of the interface. At the steady state (Figure 12. (d)), streamlines in the solid region have all disappeared, which means that the container is fully deformed due to the well-established flow field.

Figure 13 shows a grid refinement study where the spatial error norms in the velocity field are plotted versus the number of x-direction grid points. Figure 13. (a) and (b) respectively show the x-directional and y-directional velocity results. For the analysis, 125 × 100, 250 × 200, and 500 × 400 uniform Cartesian grids were used, and the error norms in the velocity field were computed over the whole domain at steady state. As shown, the algorithm shows largely a second-order convergence.

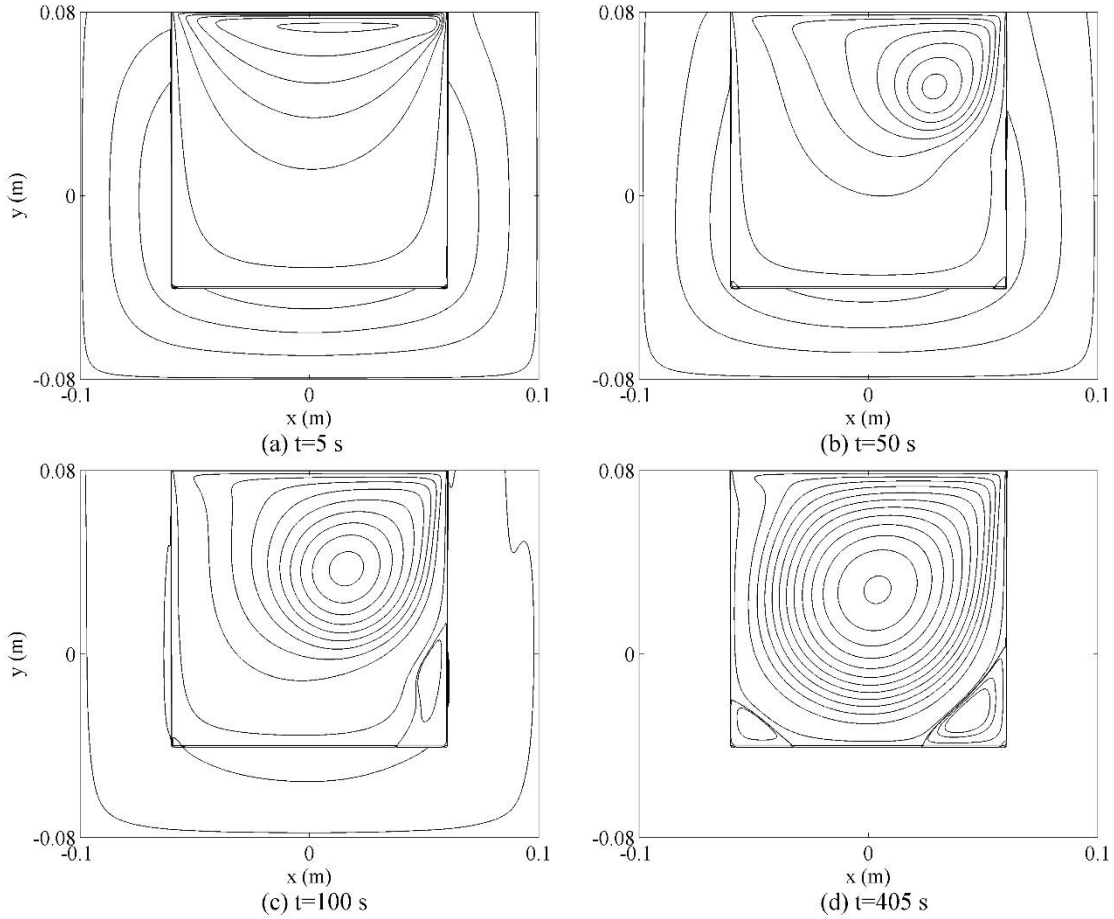

Figure 12. Evolution of streamlines: (a) *t*=5 s, (b) *t*=50 s, (c) *t*=100 s, and (d) *t*=405 s (steady-state)

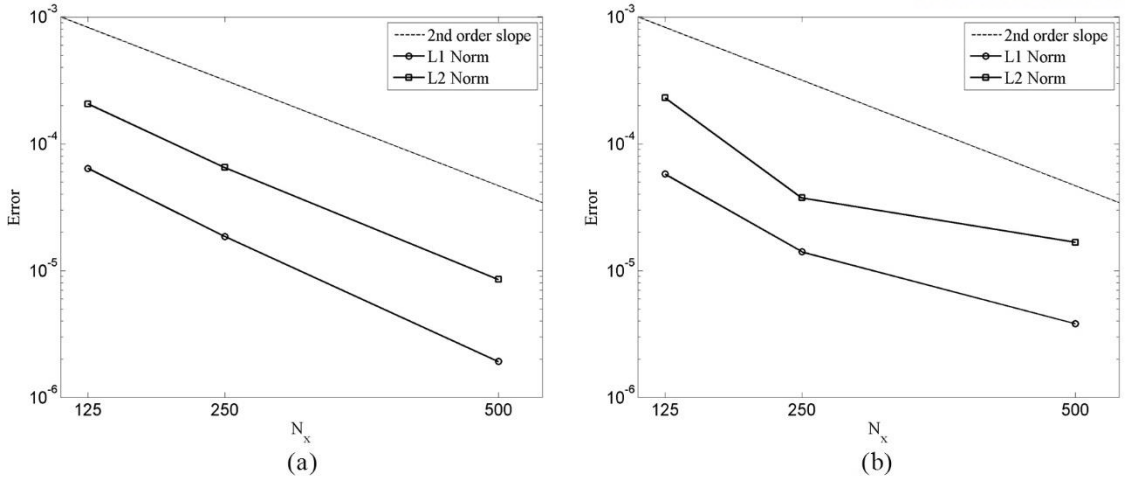

Figure 13. Grid convergence study result: (a) x-directional velocity, (b) y-directional velocity

In order to validate the accuracy of the algorithm, the same problem was simulated with COMSOL Multiphysics®. The steady-state stress field plots on the left side of Figure 14 are obtained from COMSOL Multiphysics® simulations, which are qualitatively very similar to the corresponding figures in Figure 9 ~ Figure 11. For more quantitative comparison, the stress distributions along the two horizontal lines (the locations shown as dashed and solid lines in the left figures) are calculated using the two methods and compared in the right figures, where the interface locations are indicated by vertical lines. The current simulation results agree well with the COMSOL Multiphysics® results although the interface is not sharp due to the level set function. Figure 15 shows the velocity field inside the cavity compared with the data available in reference [48]. Figure 15. (a) and (b) respectively show the x-directional velocity profile along the middle vertical line of the cavity and the y-directional velocity profile along the middle horizontal line of the cavity. As shown, a good agreement is observed.

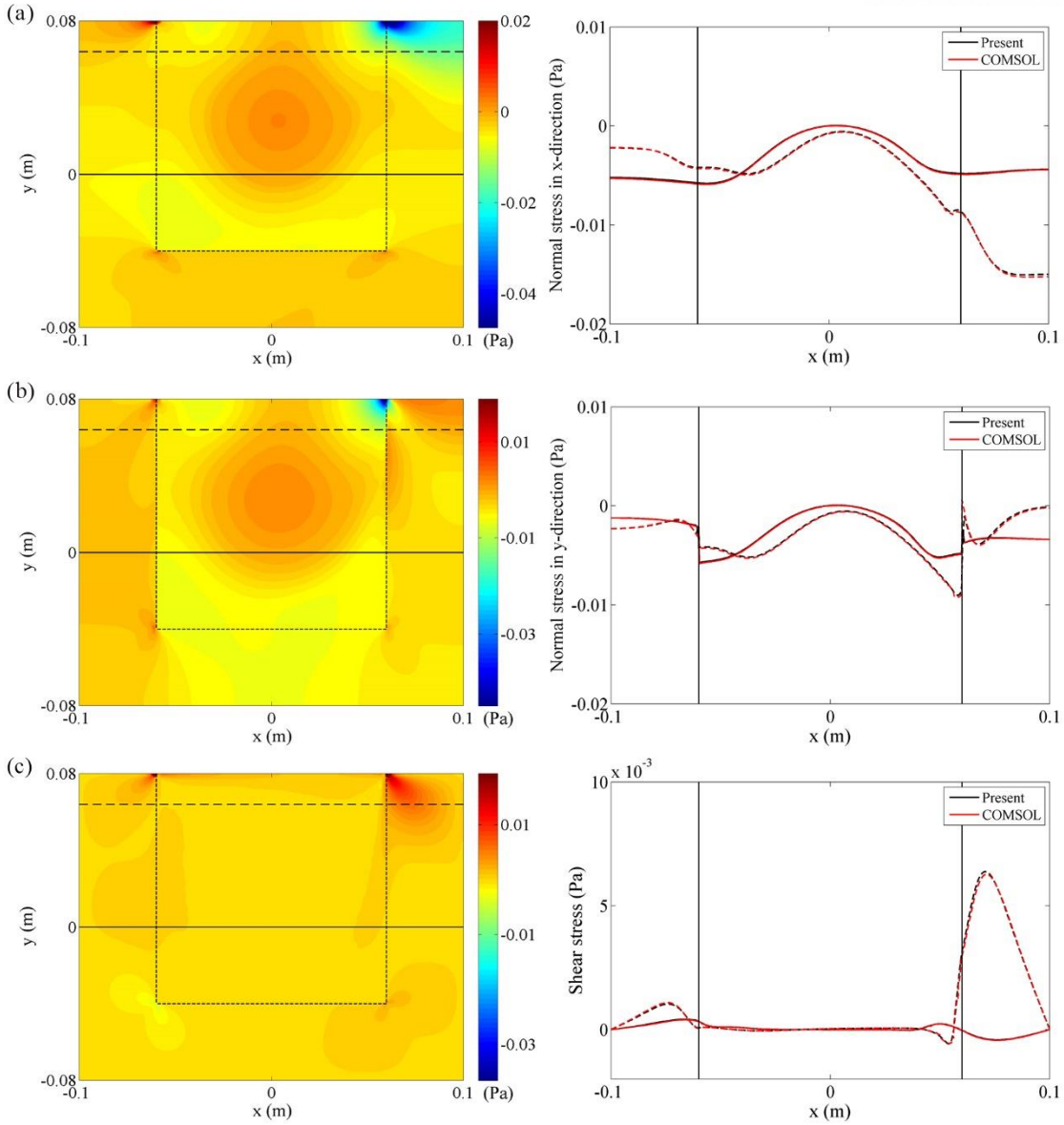

Figure 14. [Left figures] Steady-state (t = 405 s) stress fields obtained by COMSOL Multiphysics®. [Right figures] Comparison between the present study and COMSOL along the solid (y= 0 m) and dashed (y=0.064 m) horizontal lines shown in the left figures. [From top to bottom] (a) Normal stress in the x-direction, (b) normal stress in the y-direction and (c) shear stress

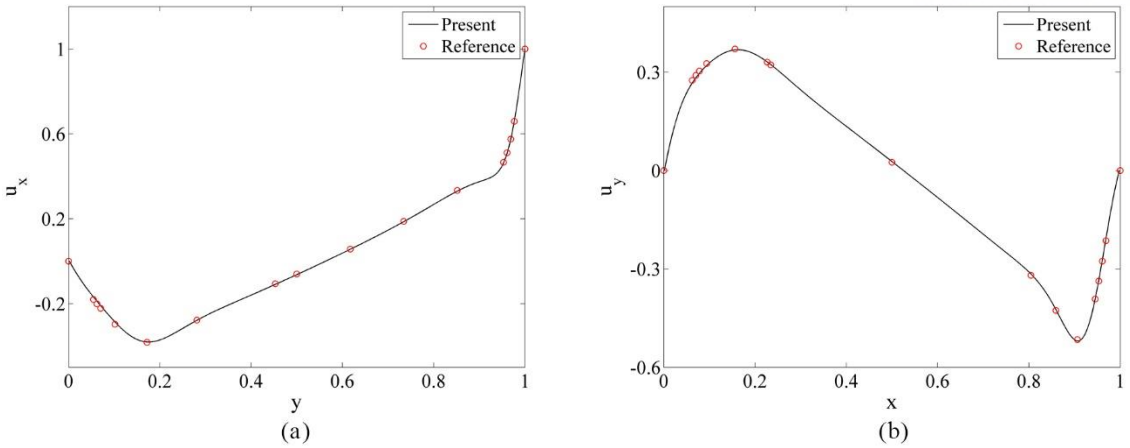

Figure 15. Comparison of fluid velocity profiles with the data in reference [48] where the values of velocity and location are scaled with the reference problem. (a) x-directional fluid velocity along the middle vertical line of the cavity, (b) y-directional fluid velocity along the middle horizontal line of the cavity.

2.3.2. Lid-driven cavity flow inside a solid container (semi-circular cavity)

A solid container with dimensions of 0.2 m × 0.1 m has a semi-circular cavity with a radius of 0.08 m. In this problem, unlike the previous example, the fluid-structure interface is not aligned with the grid lines. Just like the previous problem, the cavity is filled with water and the solid container is made of aluminum. The flow is driven by a lid at the top that moves at a velocity of 6.25×10^{-3} m/s, and the solid container is roller supported at the outer boundary. The Reynolds number of the problem is 1000. Figure 16 shows a schematic of the problem. This simulation is performed using a 512 × 256 grid, with a time step of 0.005 s.

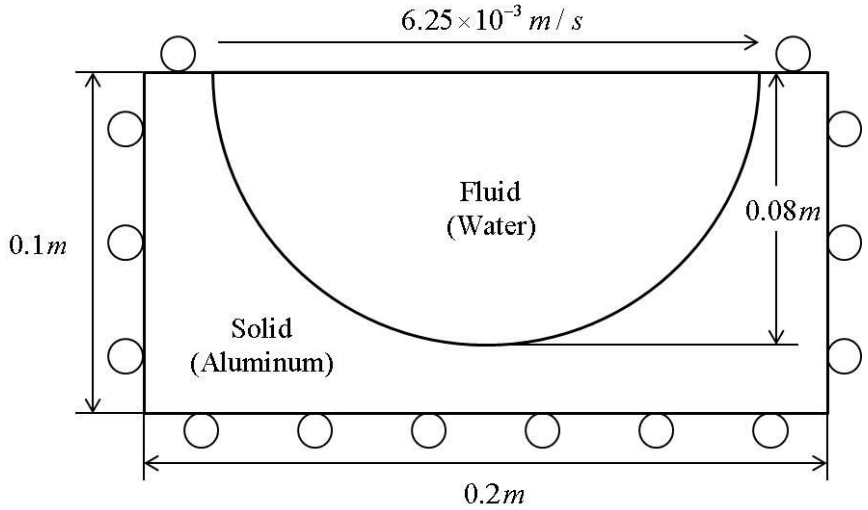

Figure 16. The schematic of the lid-driven semi-circular cavity flow problem

The stress fields for the entire domain are shown at four different times in Figure 17 ~ Figure 19, and the last ones are the steady-state results. The results show the similar behavior as the previous example. As shown in the figures, the results look reasonably good with this curved interface, and the obtained stress fields are as predicted. The flow induced stresses are developed in the structure as time progresses (which shows that the stress is well transferred to the structure in the numerical algorithm), and the stress is highly concentrated in the top-right corner of the interface. Because the fluid-structure interface is not aligned with the grid lines, stress continuity is less obvious in the figures. In this case, the normal stress in the x-direction (σ_{xx}) is continuous along the x-direction at the top-right and top-left interface and the normal stress in the y-direction (σ_{yy}) is continuous along the y-direction at the bottom interface. In addition, the stress fields indicate that there is circularly shaped flow structure inside the flow region, which is more clearly seen in the streamline plots in Figure 20. As shown in Figure 20, while the deformation is progressing in the solid domain, well-shaped streamlines exist even for solids, which all disappear completely when the fluid-induced deformation is finalized.

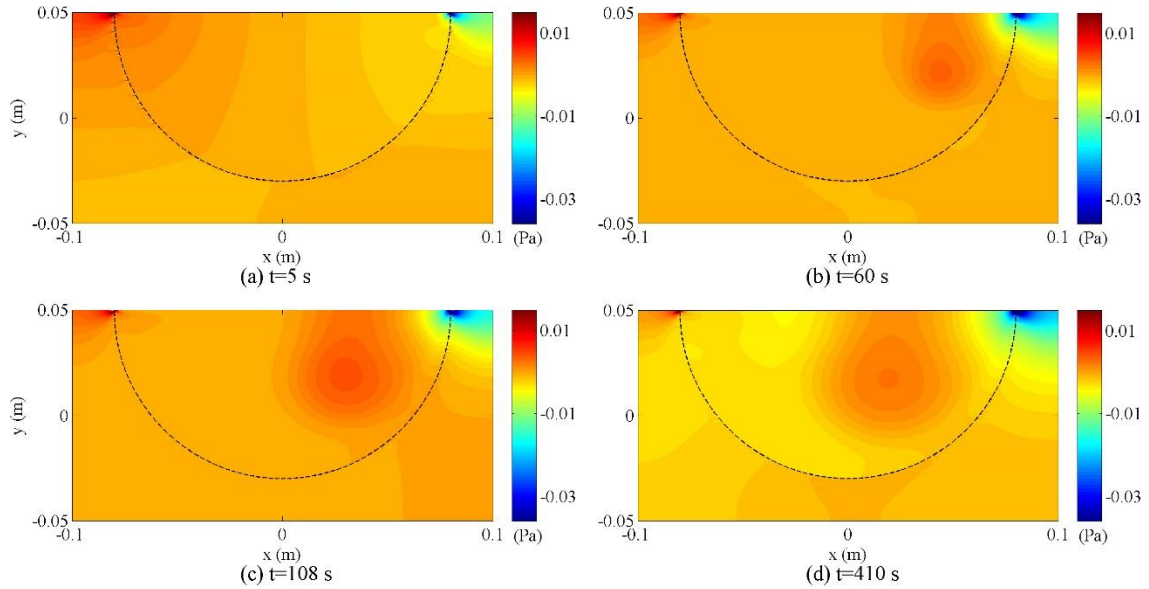

Figure 17. Evolution of normal stress (σ_{xx}): (a) t=5 s, (b) t=60 s, (c) t=108 s, and (d) t=410 s (steady-state)

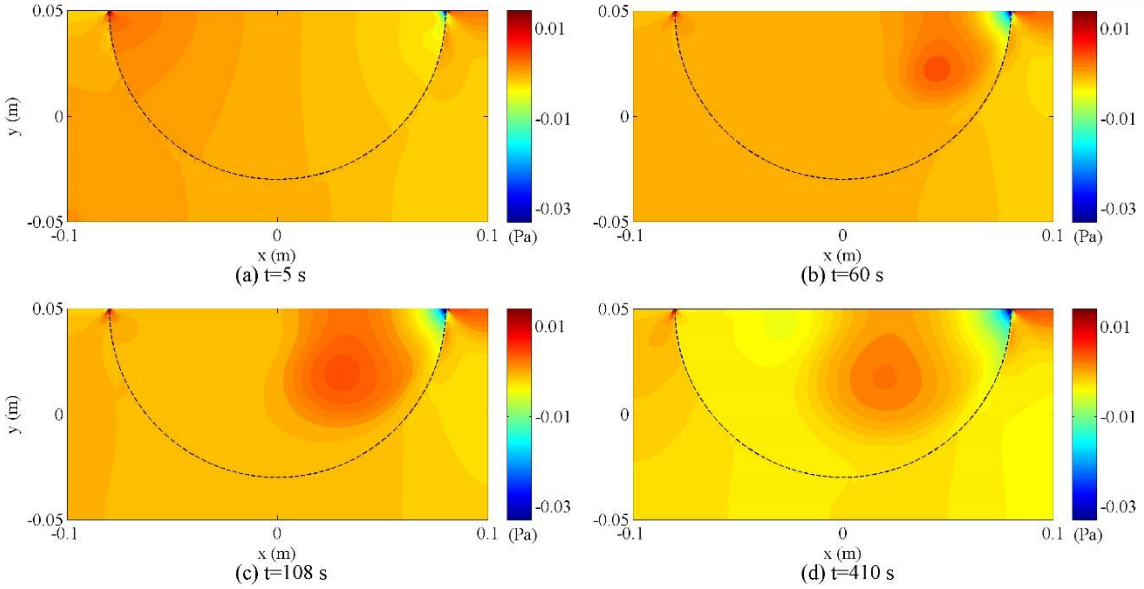

Figure 18. Evolution of normal stress (σ_{yy}): (a) t=5 s, (b) t=60 s, (c) t=108 s, and (d) t=410 s (steady-state)

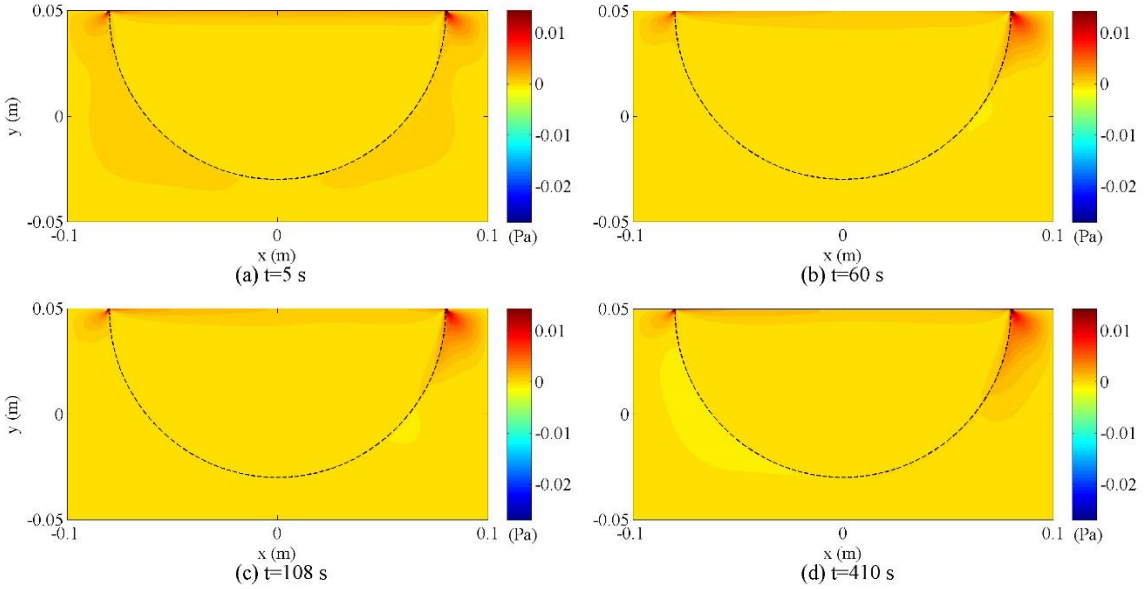

Figure 19. Evolution of shear stress (σ_{xy}): (a) t=5 s, (b) t=60 s, (c) t=108 s, and (d) t=410 s (steady-state)

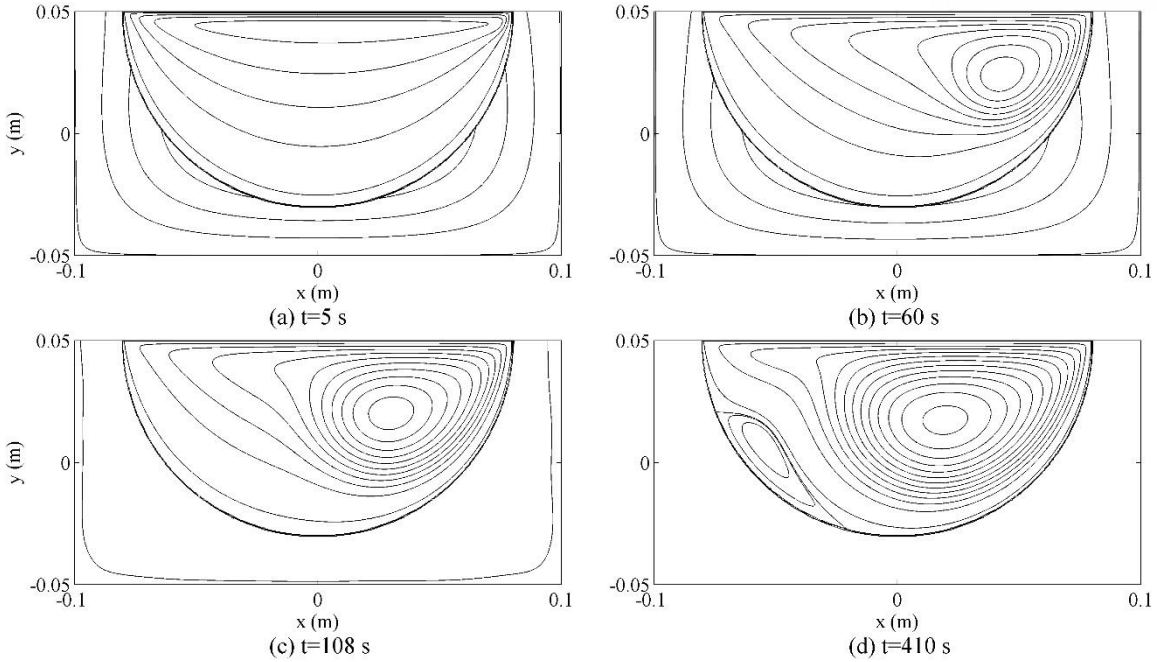

Figure 20. Evolution of streamlines: (a) *t*=5 s, (b) *t*=60 s, (c) *t*=108 s, and (d) *t*=410 s (steady-state)

For validation purposes, we simulated the same problem using COMSOL Multiphysics®. The obtained steady-state stress fields are presented in the left side of Figure 21. The stress fields from both simulations are reasonably similar, and as the stress distributions along the reference lines are compared in the right side of Figure 21. Slight spikes are observed in the smeared interface area, but even for the curved boundary problems, the current simulation results agree well with the COMSOL Multiphysics® results. Note that COMSOL Multiphysics® are based on a partitioned approach and the interfaces are aligned with the grid lines. Figure 22 shows the velocity field inside the cavity compared with the data available in reference [49]. Figure 22. (a) and (b) respectively show the x-directional fluid velocity along the middle vertical line of the cavity and the y-directional fluid velocity along the horizontal line which is one fourth of the cavity depth below from the surface. As shown, a good agreement is observed.

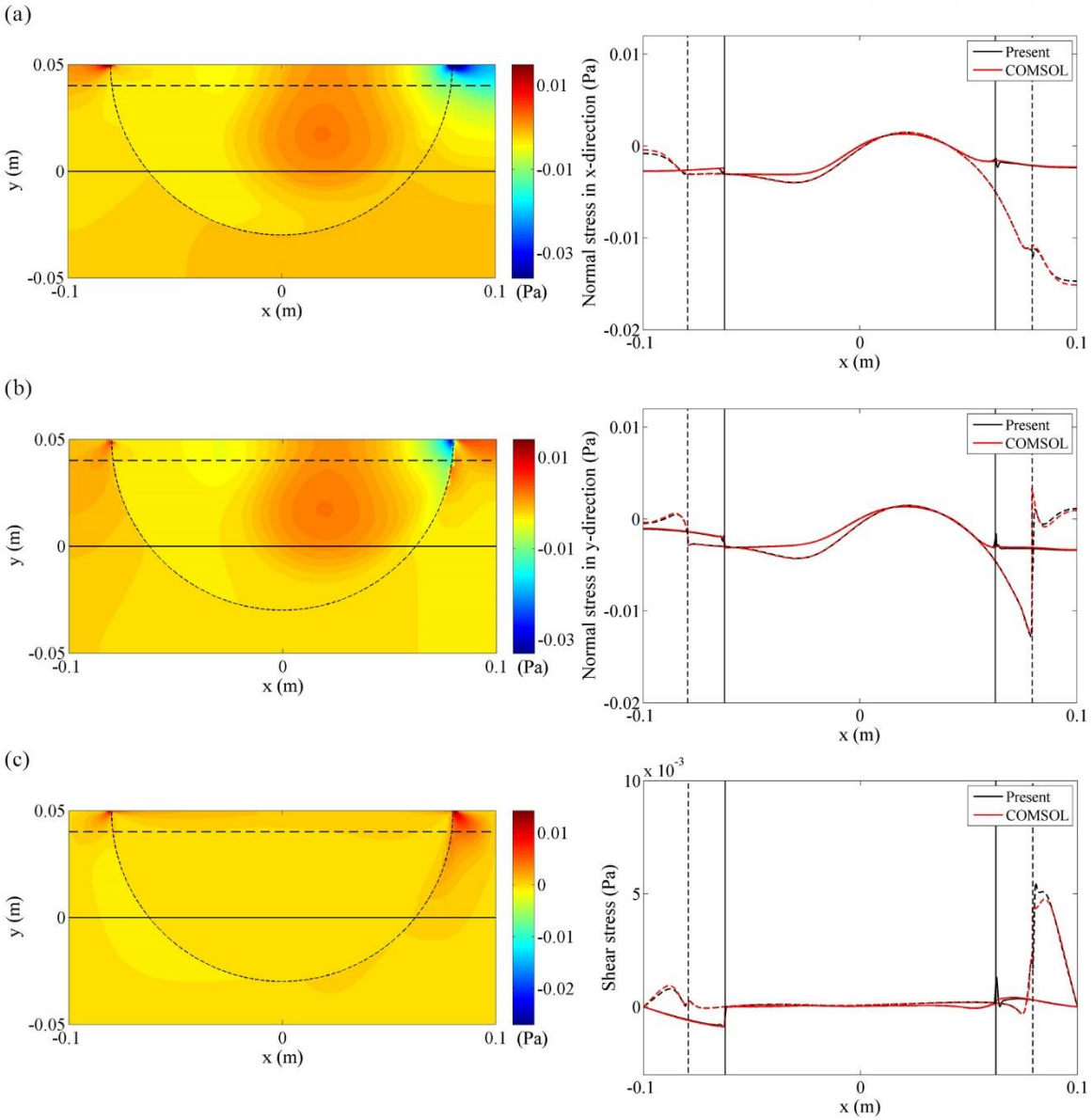

Figure 21. [Left figures] Steady-state (t=410 s) stress fields obtained by COMSOL Multiphysics®. [Right figures] Comparison between the present study and the COMSOL simulation along the solid (y= 0 m) and dashed (y=0.04 m) horizontal lines shown in the left figures. [From top to bottom] (a) Normal stress in the x-direction, (b) normal stress in the y-direction and (c) shear stress

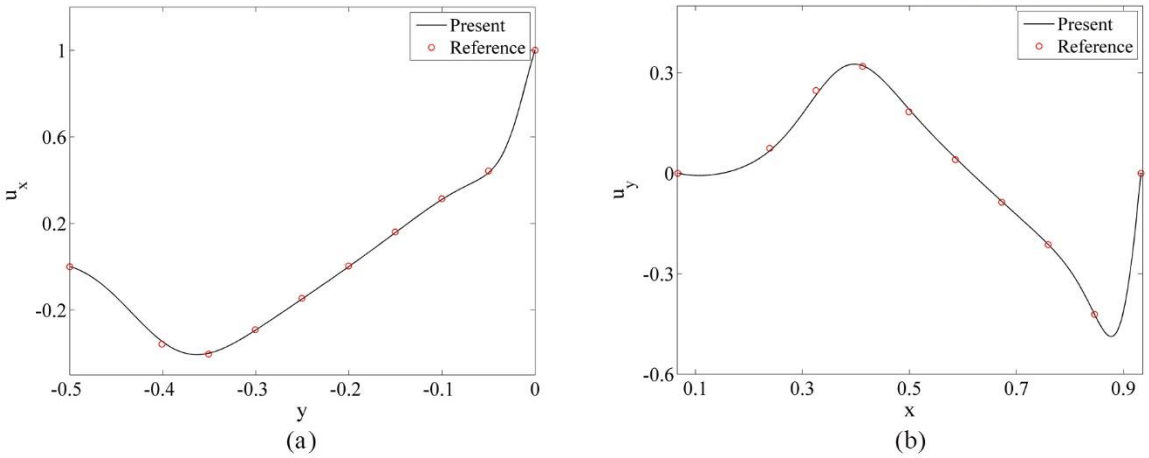

Figure 22. Comparison of fluid velocity profiles with the data in reference [49]. (a) x-directional fluid velocity along the middle vertical line of the cavity, (b) y-directional fluid velocity along the horizontal line which is one fourth of the cavity depth below from the surface.

2.3.3. Flow over a circular cylinder

The flow past a circular cylinder is considered, where the stress field inside the cylinder that is also made of aluminum, is solved simultaneously with the flow field in terms of velocity. A circular cylinder with a diameter (D) of 0.3 m is placed at $x = -8D$, $y = 0$ when the computational domain has a size of $32D \times 16D$ ($-16D \le x \le 16D$, $-8D \le y \le 8D$). A fluid with a density of 1 kg/m^3 and a viscosity is 3×10^{-3} kg/m·s flows from left at $U_\infty = 1$ m/s, and the solid cylinder is fixed at two points, $x = -8D$, $y = \pm 0.34D$. In Figure 23, The schematic of the problem is presented together with the boundary conditions. The Reynolds number of the flow is 100. This simulation is tested on a 512 × 256 grid, using a time step of 0.005 s.

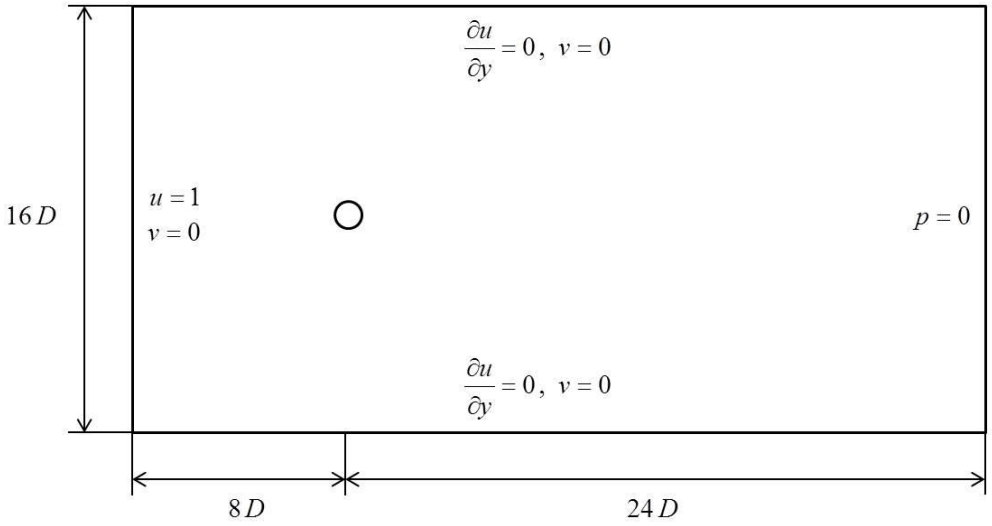

Figure 23. Computational domain and boundary conditions for the flow-over-a-cylinder problem

In Figure 24, the normal stresses and vorticity distributions at t = 113 s are shown. To resist the drag force due to the flow, stress is concentrated at the two fixed points inside the cylinder, and as the vorticity distribution shows, the von Karman vortex street is generated behind the cylinder. Figure 25 shows the enlarged views of normal stress fields around the cylinder, and the normal stress distributions along the horizontal central line are compared with COMSOL simulation results in Figure 26, where two vertical lines indicate the boundaries of the cylinder. As seen from the figure, the two results reasonably well match each other. Although the difference seems to be a bit larger than the previous two examples due to the relatively larger smeared interface region compared to the structure size, the two results are still reasonably close.

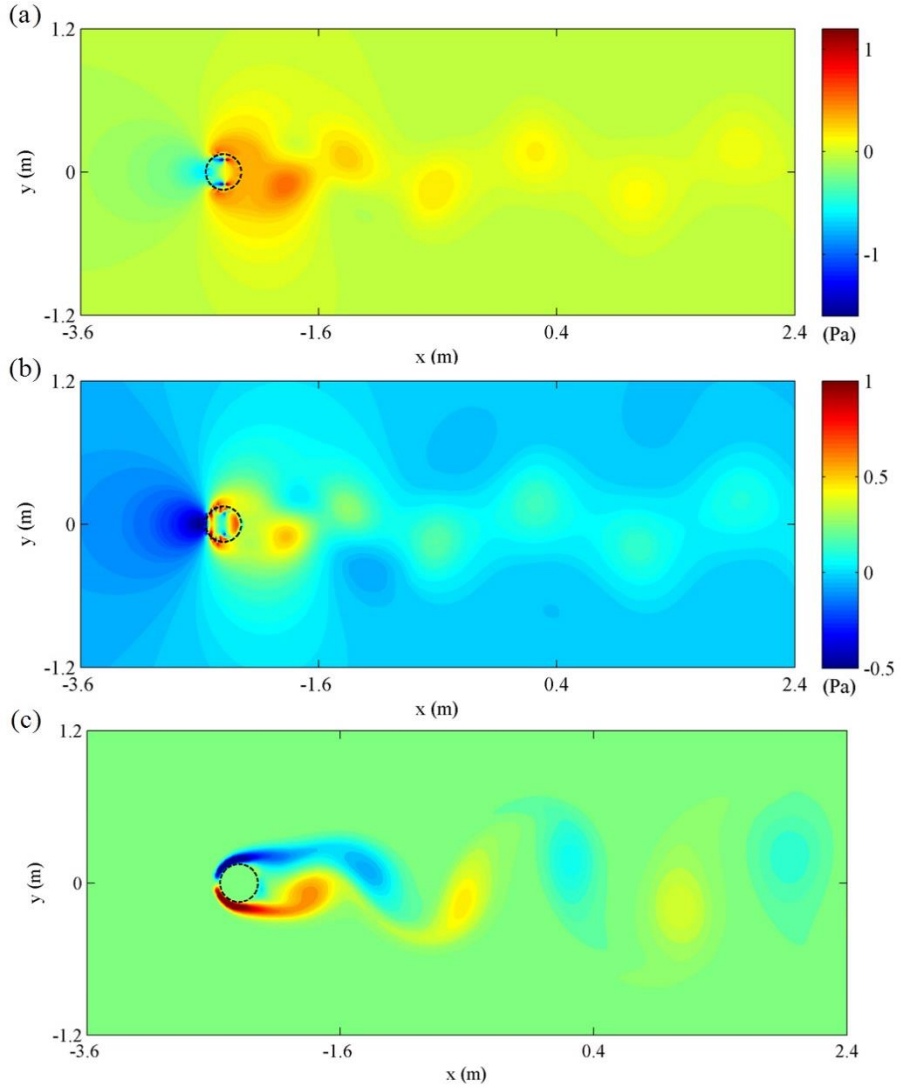

Figure 24. Simulation results of the flow over a circular cylinder at $t = 113\text{s}$: (a) normal stress in the x-direction, (b) normal stress in the y-direction and (c) vorticity field

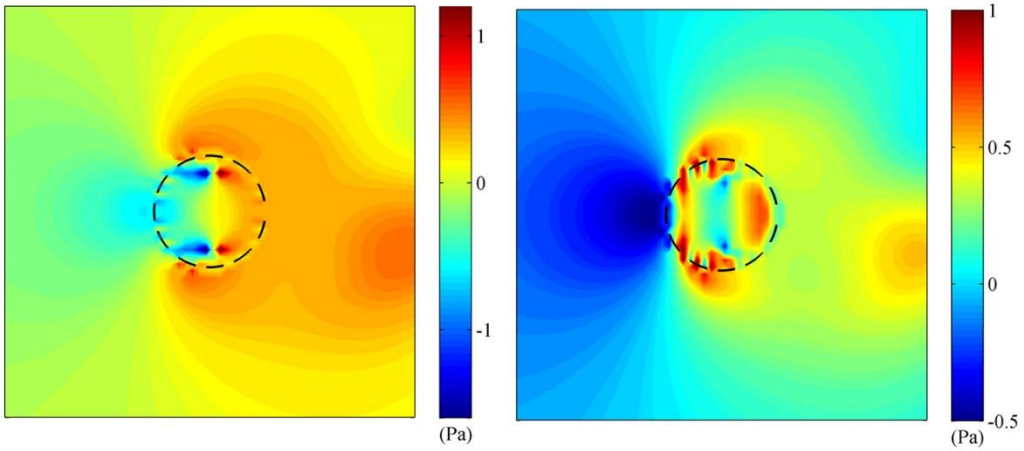

Figure 25. Stress fields magnified around the cylinder: (a) normal stress in the x-direction and (b) normal stress in the y-direction

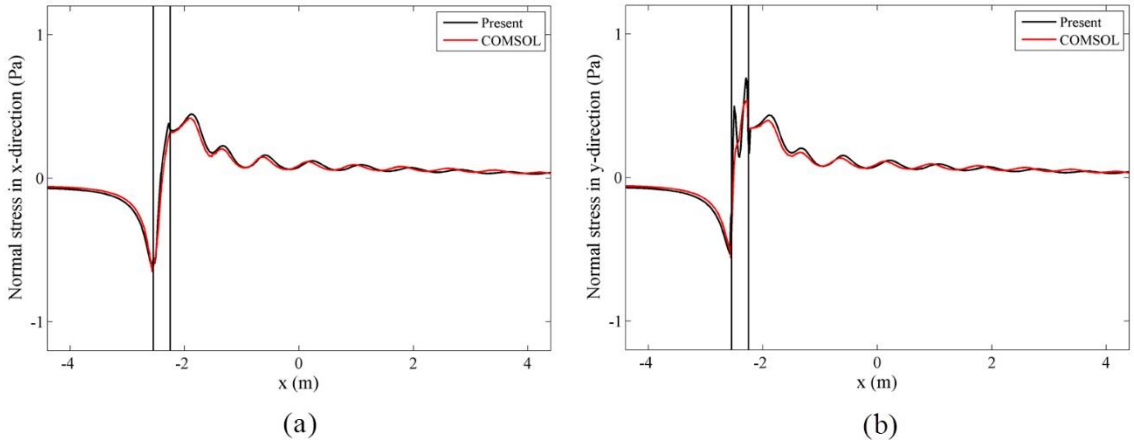

Figure 26. Comparison between the present study and the COMSOL simulation along the central horizontal line: (a) Normal stress in the x-direction, (b) normal stress in the y-direction

2.4. Conclusions

A novel monolithic method for computing flow induced stresses in structures with arbitrarily-shaped stationary boundaries has been presented. In this work, a unified momentum equation that is valid for both fluids and solids is derived in terms of velocity, and the momentum equations for fluids and solids are hybridized around the interface using the level set function. In order to solve the governing equations numerically, the SIMPLE algorithm is used. Three numerical examples has been successfully tested using the proposed method, and we believe that this method is simple to implement and can be easily applied to many other similar problems.

3. Unified momentum equation approach for moving interface FSI problems

This chapter includes the published contents:

H. Yeo, H. Ki*, J. Comput. Phys. (2020), Copyright © 2020 Elsevier Inc.

In this chapter, the unified momentum equation approach presented in Chapter 2 is extended to moving interface FSI problems.

3.1. Mathematical model

In order to capture the moving interface, we employed the accurate conservative level set method [50]. This method was developed by improving the conservative level set method [51, 52] by introducing the re-distancing algorithm to obtain accurate interface normals. In the conservative level set method, the signed distance function is replaced by a hyperbolic tangent profile.

$$\psi = \frac{1}{2}\left(\tanh\left(\frac{\phi}{2\varepsilon} \right) + 1 \right) \tag{33}$$

Here, ε is the interface thickness parameter and $\varepsilon = 0.5\,\Delta x$ is used in this study.

The interface is represented as a $\psi = 0.5$ iso-surface and evolves according to the velocity field using the following advection equation:

$$\frac{\partial \psi}{\partial t} + \nabla \cdot \left(\mathbf{u}\psi \right) = 0 . \tag{34}$$

Note that the hyperbolic tangent function is only used for the advection and re-initialization step of the interface, and the signed distance function reconstructed from the hyperbolic tangent function during the accurate conservative level set algorithm [50] is used for the other numerical steps. When updating the interface using the level set equation, however, some numerical difficulties arise due to the Eulerian nature of this formulation. In Figure 27, a schematic drawing of a moving fluid–solid interface at two successive time steps is shown, where the yellow and green regions respectively represent a moving structure at the previous time step (t^0) and current time step (t). The white region is a fluid.

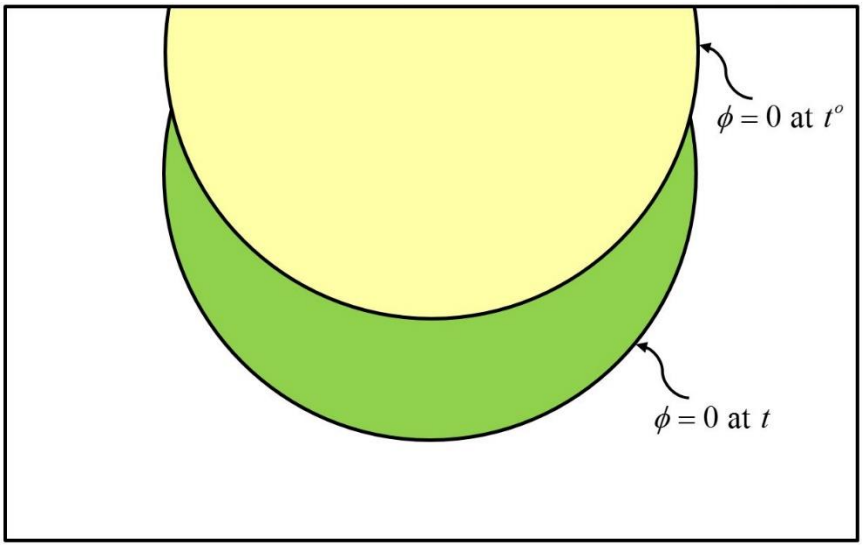

Figure 27. Schematic drawing of a moving fluid–structure interface, where the yellow and green regions represent a moving structure at time steps t^0 and t, respectively.

Obviously, the computational cells inside the yellow region are structure cells where the displacement field is continuous and well defined. As the interface moves, however, newly formed structure cells (those inside the green region) are formed and do not have proper displacement values. To avoid this problem, in this study, we used an extrapolation method [53], where the solid displacement field in the yellow region is extended to the nearby fluid cells by solving the following equation:

$$\frac{\partial \mathbf{d}}{\partial \tau} + U(\phi)\mathbf{n} \cdot \nabla \mathbf{d} = 0 . \tag{35}$$

Here, τ is the fictitious time, U is the unit Heaviside function, which is defined as

$$U = \begin{cases} 1 & \text{if } \phi \geq \alpha \\ 0 & \text{if } \phi < \alpha \end{cases} \tag{36}$$

and $\mathbf{n}$ is the unit normal vector perpendicular to the interface:

$$\mathbf{n} = \frac{\nabla \phi}{|\nabla \phi|} . \tag{37}$$

3.2. Numerical algorithm

In this section, numerical algorithms for solving the previously described equations are described. The overall procedure is shown as a flowchart in Figure 28.

First, the unified momentum equation presented in Chapter 2 (Eq. (11)) is solved by using the SIMPLE algorithm. Once the velocity and pressured fields are updated, the displacement field is calculated from Eq. (8) and extended to the fluid region by solving Eq. (35). In this study, Eq. (35) is solved using a second-order upwind scheme, and the unit normal vector **n** is calculated using a second-order central difference scheme [53]. Note that the use of only a few iterations is sufficient because an extended displacement is required only near the interface. To capture the interface, the advection equation (Eq. (34)) is solved using a fifth-order high order upstream central (HOUC) scheme [50]. Then, a fast marching method [54] is applied to reconstruct the signed distance function (ϕ) from the hyperbolic tangent function (ψ).

$$\left\|\nabla\phi\right\| = 1 \tag{38}$$

Using the reconstructed signed distance function, the smoothed Heaviside function and interface normals are computed (Eqs. (16) and (37)). Finally, the following re-initialization equation was solved [52].

$$\frac{\partial\psi}{\partial\tau} + \nabla\cdot\left(\psi\left(1-\psi\right)\mathbf{n}\right) = \nabla\cdot\left(\varepsilon\left(\nabla\psi\cdot\mathbf{n}\right)\mathbf{n}\right) \tag{39}$$

This re-initialization equation is discretized using the second-order finite difference method in space and the semi-implicit Crank–Nicolson method in time [50]. The numerical details on the accurate conservative level set method can be found in [50].

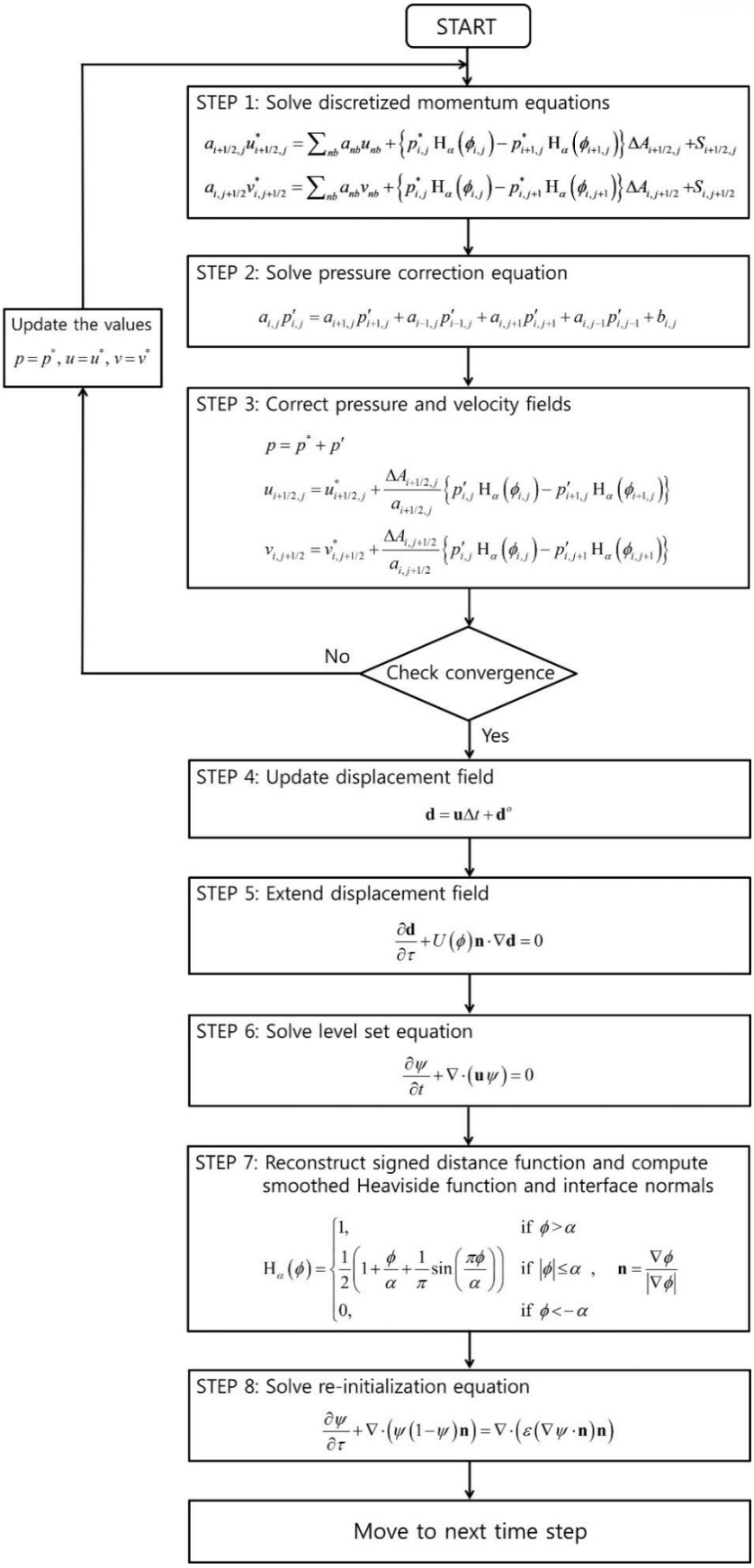

Figure 28. Flowchart showing the overall numerical algorithms for moving interface FSI problems

3.3. Numerical examples

In this section, moving interface FSI problems including validation examples are considered. The simulations are performed on a uniform Cartesian grid. Here, the $b_{i,j}$ term in Eq. (29) is set to zero for $\phi < 0.5\alpha$.

3.3.1. Falling disk in a fluid

As the first example, a well-known benchmark problem in which a circular disk falls due to the gravitational force inside a rectangular channel filled with an incompressible Newtonian was considered. To verify the proposed method, in this study, the same parameters (including the dimensions and material properties) used in Hachem et al.'s study [55] were adopted, except for the material properties of the solid disk. In Hachem et al.'s study, the disk was assumed as a rigid body and the Young's modulus and Poisson's ratio were not given; however, in the present study, we modeled the disk as an elastic body having a Young's modulus of 2×10^7 g/cm·s^2 and a Poisson's ratio of 0.35.

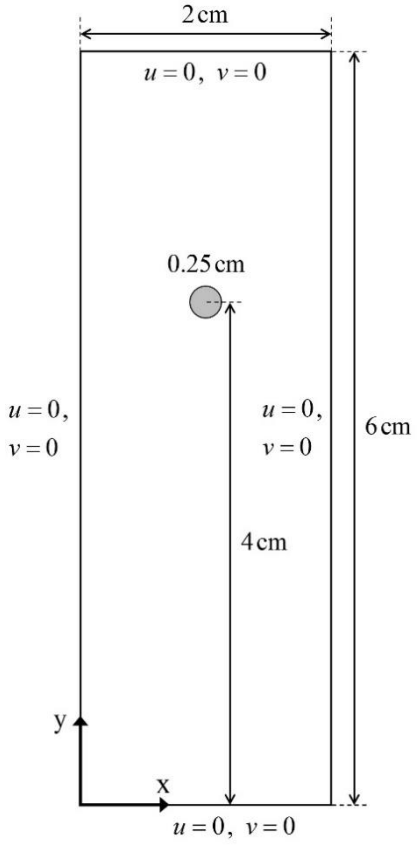

Figure 29. Schematic drawing of the falling disk problem. The coordinate system, boundary conditions, and dimensions are shown in the figure.

In Figure 29, a schematic drawing of the falling disk problem is shown. The height and width of the domain are 2 cm × 6 cm, and the diameter of the disk is 0.25 cm. The density and viscosity of the fluid are assumed to be 1 g/cm^3 and 0.1 g/cm·s, respectively, and the density of the disk is 1.25 g/cm^3. The acceleration due to gravity is 9.8 m/s^2. The disk is located 4 cm above the floor, and the fluid and disk are initially at rest. A no-slip condition is applied on the boundaries. This simulation was conducted using a 200 × 600 grid, and a time step of 0.0001 s was used.

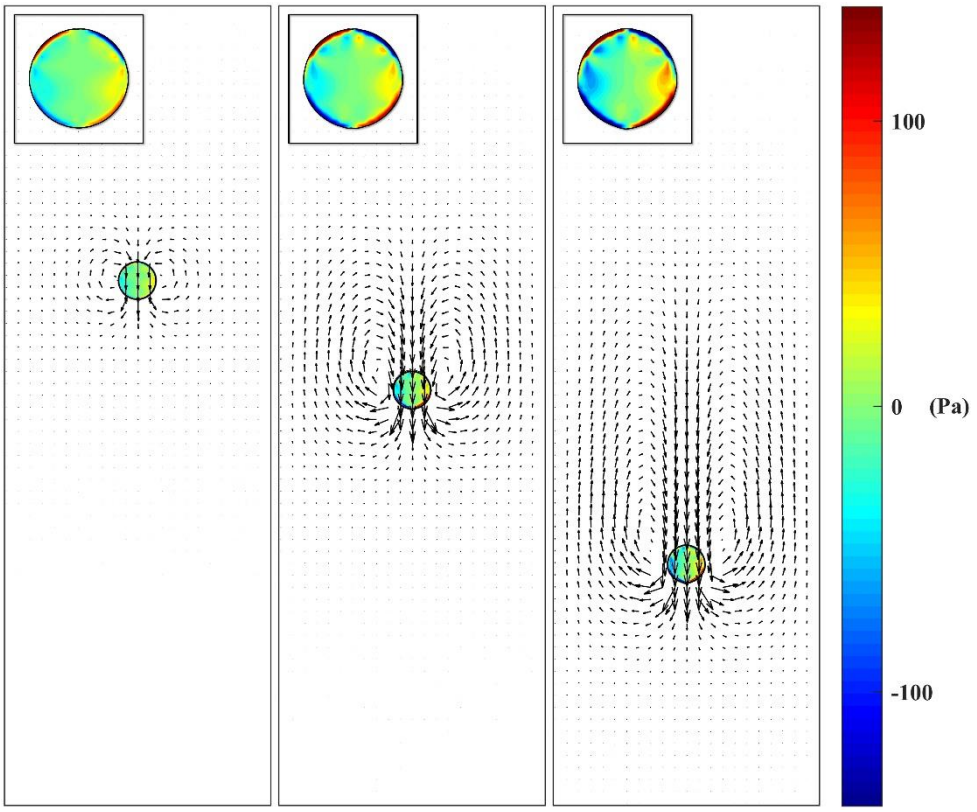

Figure 30. Velocity and shear stress distributions predicted from the simulation. From left to right, the elapsed times are 0.05, 0.25, and 0.5 s.

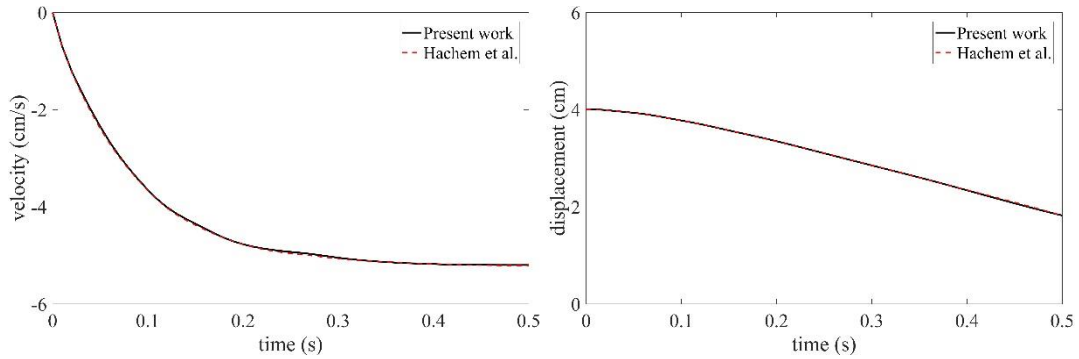

Figure 31. Velocity and displacement of the disk versus time. Black solid lines, results obtained by the present method; red dashed lines, results obtained by Hachem et al. [55]

The simulation results of the falling disk problem are shown in Figure 30. The velocity field in the entire domain and the shear stress inside the solid disk are shown together at t = 0.05, 0.25, and 0.5 s. In each figure, the magnified shear stress distribution inside the disk is presented as an inset. As shown in the figure, a flow develops around the disk as the disk moves down from the gravitational pull. From the interaction with the developed flow, shear stresses are also generated inside the disk, particularly near the surface. As the disk is pulled down further, the interaction and shear stress field both become stronger. Owing to the downward motion of the falling disk, the fluid also moves down and then upward around the disk to satisfy the continuity constraint. This type of FSI leads to the formation of vortices behind the falling disk.

In Figure 31, the simulation results (black solid lines) are compared with the results by Hachem et al. [55] (red dashed lines), where a stabilized three-field finite element method was applied with an anisotropic mesh adaptation. As shown in the left figure, the disk is initially at rest and then accelerates downward. In this problem, three external forces, namely, the gravitational force, buoyancy force, and drag force, act on the disk. The gravitational force pulls the disk down in proportion to the disk weight, whereas the buoyancy force acts on the immersed structure in the opposite direction of the gravitational force. The drag force is developed by the fluid viscosity and resists the motion of the immersed structure. Because the drag force is proportional to the velocity, the acceleration of the disk gradually decreases. When the net force acting on the disk becomes zero due to the increasing drag force, the disk reaches the terminal velocity. Accordingly, the elevation of the disk decreases from the initial height. Overall, as shown in the figures, our simulation results agree very well with those by Hachem et al.

3.3.2. Oscillation of a flexible rod in a channel

As the second example, a flexible rod oscillating from the pressure oscillation was simulated, where the deformation of the rod is relatively large. Note that this method employs a linear elastic model, and a large deformation problem may not be a suitable application. However, we considered this problem to demonstrate the capabilities of the presented method. The flexible rod problem has been used as a test example in several FSI studies, although the rod has generally been modeled as an extremely thin structure [56], or the internal stress distribution of the rod has not been investigated [57]. Note that this method is capable of computing not only the dynamic motions of fluid–structure interfaces but also the stress fields in both the fluid and structure.

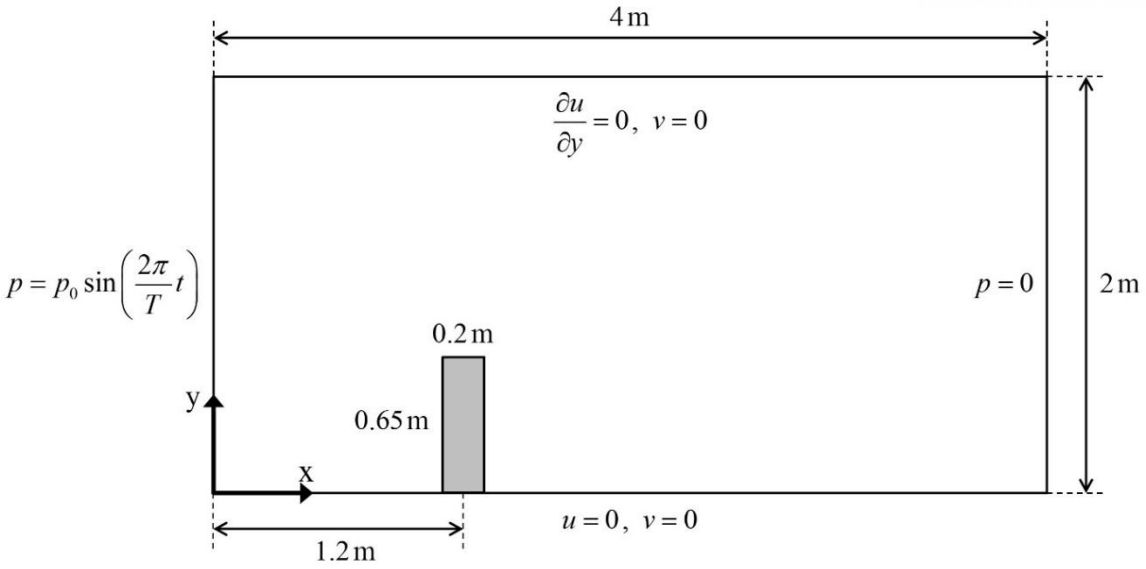

Figure 32. Schematic drawing of the flexible rod problem. The coordinate system, boundary conditions, and dimensions are shown in the figure.

Figure 32 shows a schematic drawing of the problem. The channel is filled with water with a density of 1,000 kg/m^3 and a viscosity of 10^{-3} kg/m·s. The size of the channel is 4 m × 2 m, and a rod with dimensions of 0.2 m × 0.65 m is fixed to the bottom wall 1.2 m from the front. The rod has a density of 1,250 kg/m^3, Young's modulus of 10^6 N/m^2, and Poisson's ratio of 0.48. A temporally periodic pressure is applied at the inlet plane ($p = p_0\sin(2\pi t/T)$) and zero pressure is imposed at the outlet plane. Initially, the fluid and structure are both stationary.

Table 1. Four simulation cases of the flexible rod problem

Case	***E***	p_0	***T***
A	10^6 N/m^2	1.0×10^4 Pa	1 s
B	10^6 N/m^2	1.5×10^4 Pa	1 s
C	0.5×10^6 N/m^2	1.5×10^4 Pa	1 s
D	10^6 N/m^2	1.0×10^4 Pa	0.5 s

In this study, four cases were simulated to see the effects of the Young's modulus, inlet pressure, and period of the inlet pressure, as summarized in Table 1. Case A is the reference case, and in Case B, the amplitude of the inlet pressure was increased by 50% from Case A, whereas in Case C, the Young's modulus was decreased by 50% from Case B, and in Case D, the period of the inlet pressure was reduced by 50% from Case A. This example was tested on a 512 x 256 grid, with a time step of 0.0005 s.

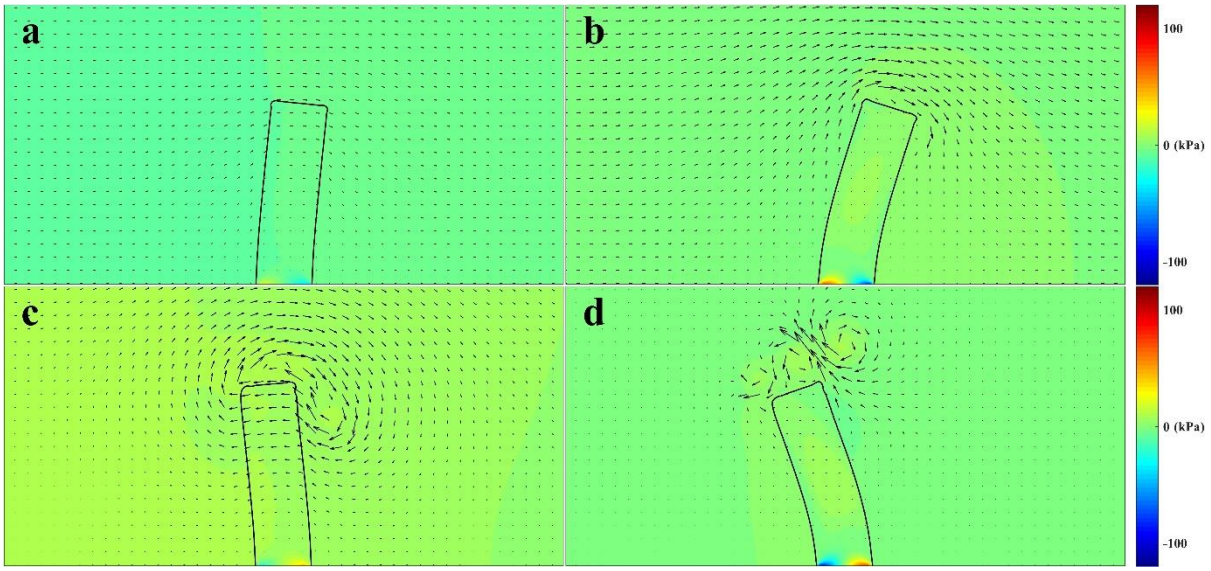

Figure 33. Results of Case A: Shapes of the rod shown with the velocity and x-component normal stress (σ_{xx}) fields in the entire domain at t = (a) 0.25, (b) 0.5, (c) 0.75, and (d) 1 s.

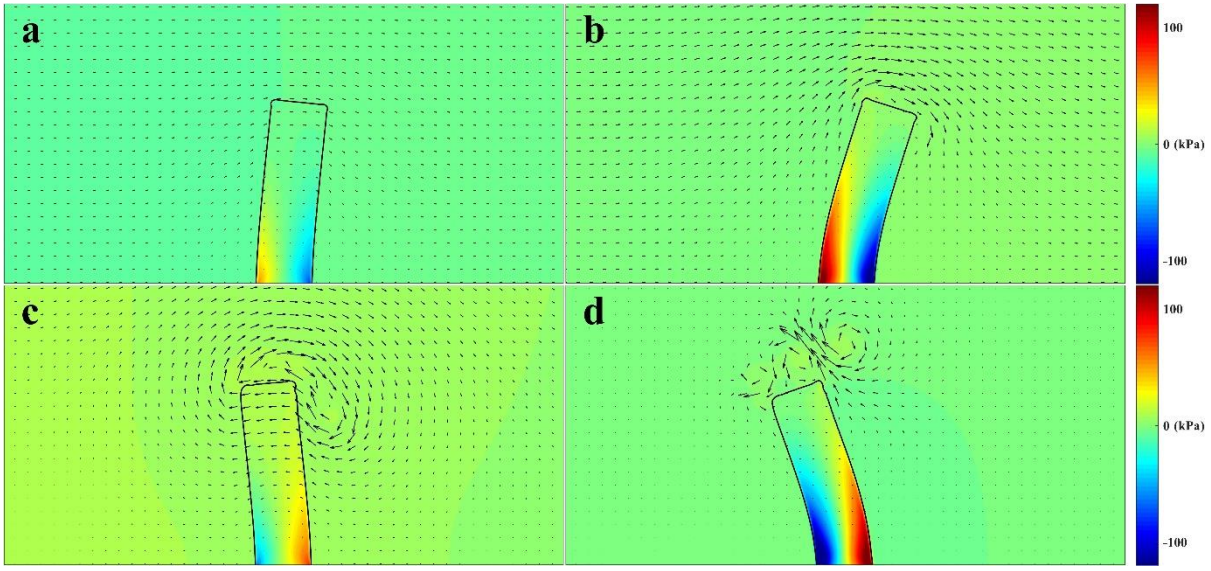

Figure 34. Results of Case A: Shapes of the rod shown with the velocity and y-component normal stress (σ_{yy}) fields in the entire domain at t = (a) 0.25, (b) 0.5, (c) 0.75, and (d) 1 s.

Figure 33 shows the shapes of the rod at t = 0.25, 0.5, 0.75, and 1 s, as shown with the x-component normal stress fields for Case A. The y-component normal stress fields are shown in Figure 34. As the pressure increases at the inlet, the fluid starts to flow from left to right. The rod also bends in the flow direction owing to the increasing flow, and the stress concentration is observed at the bottom of the rod where it is fixed. It is shown that the normal stress of the y-component (Figure 34) is more

prominent than that of the x-component (Figure 33) because the flow tries to pull the rod out in the y-direction. In addition, tensile stresses are developed on the opposite side of the rod bending direction, as the rod is stretched there, and the strength of the stress is proportional to the degree of bending. For example, the stress field at t = 0.5 s is stronger than at t = 0.25 s, which is also the case for the fluid velocity. From t = 0.25 to 0.5 s, the elastic energy stored in the rod continues increasing as the rod experiences a continuous deformation. At some point, the elastic force built into the rod (which tends to restore its original shape) becomes larger than the force from the fluid pushing the rod in the flow direction. Then, the moving direction of the rod starts to be reversed, although the fluid still flows from left to right.

Note that, after t = 0.5 s, the inlet pressure becomes negative, and at t = 0.75 s, the inlet pressure reaches its maximum negative value (Figure 33. (c) and Figure 34. (c)). However, the flow is still mainly to the right and shows a complicated pattern. The fluid above the top of the rod continues to flow from left to right owing to the inertial force, whereas the fluid on the right side of the rod flows to the left following the bending motion of the rod. From this dynamic fluid–structure interaction, a vortex is formed. According to the bending direction of the rod, the stress field is reversed, and tensile stresses are observed on the right side. Eventually, the rod returns to its original shape overcoming the fluid flow; this rod motion can be seen in Figure 33. (d) and Figure 34. (d).

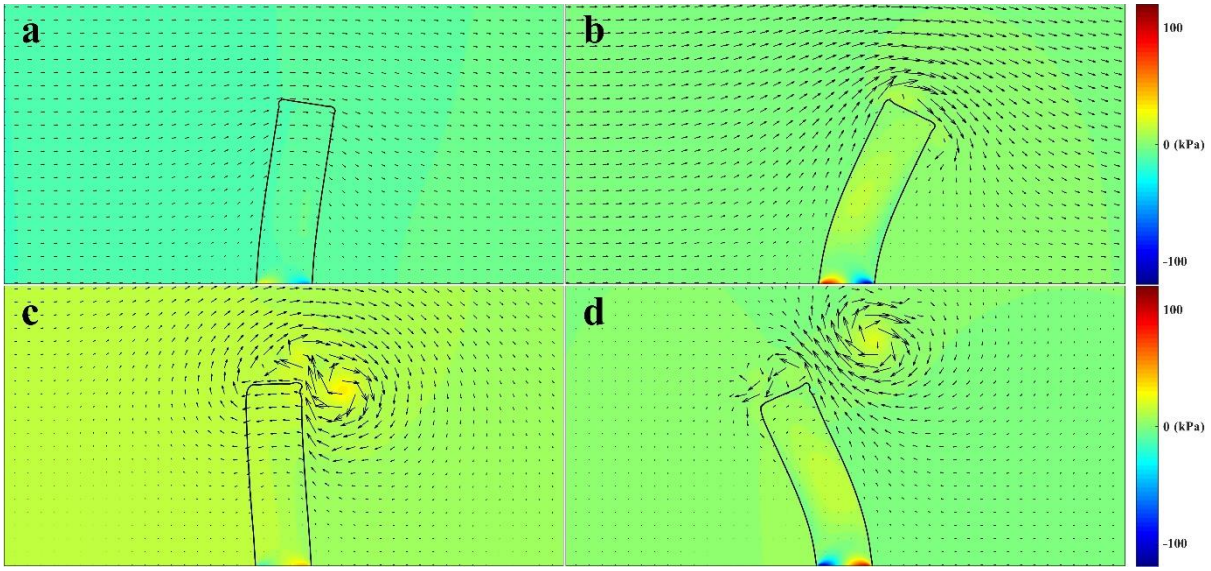

Figure 35. Results of Case B: Shapes of the rod shown with the velocity and x-component normal stress (σ_{xx}) fields in the entire domain at t = (a) 0.25, (b) 0.5, (c) 0.75, and (d) 1 s.

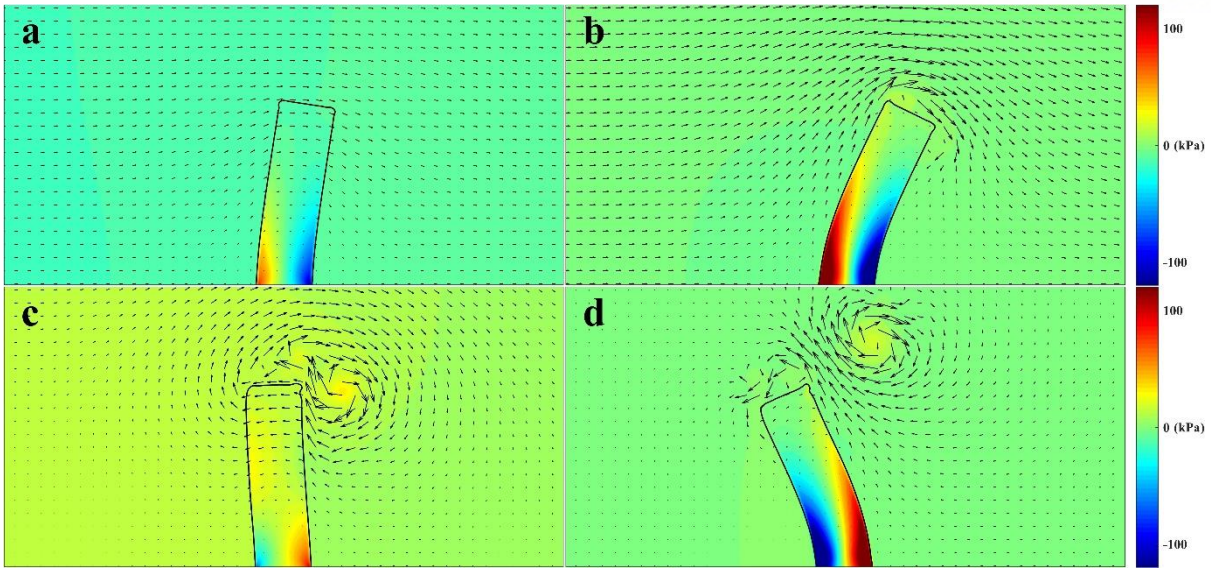

Figure 36. Results of Case B: Shapes of the rod shown with the velocity and y-component normal stress (σ_{yy}) fields in the entire domain at t = (a) 0.25, (b) 0.5, (c) 0.75, and (d) 1 s.

Figure 35 shows the shapes of the rod at t = 0.25, 0.5, 0.75, and 1 s, as indicated through the x-component normal stress fields for Case B. The y-component normal stress fields are shown in Figure 36. For Case B, the amplitude of the inlet pressure is increased to 1.5×10^4 Pa (a 50% increase). As shown in the figures, the results obtained (including the rod behavior, the flow field, and the stress field) are qualitatively similar to those of Case A. Quantitatively, however, the flow velocity and rod deformation are larger than in Case A because the magnitude of the inlet pressure is increased, and consequently, the stresses in the rod become more prominent, i.e., stronger tensile and compressive stresses are observed on both sides of the rod. Note that, because the rod is more deformed than in Case A, more elastic energy is stored, and the restoring motion of the rod is more dynamic, providing evidence that the structure is fully coupled and interacts with the flow field.

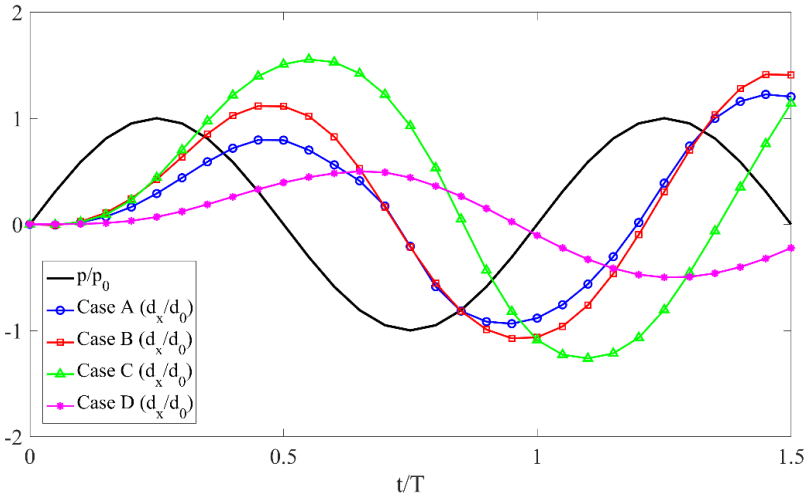

Figure 37. Normalized x-directional displacement of the rod tip versus normalized time.

The velocity and stress fields of Cases C and D are not presented here, but the dynamics of the rod for all cases are compared in Figure 37. In this figure, the normalized maximum x-directional displacement of the rod (i.e., the x-component displacement of the rod tip divided by a rod width d_0 of 0.2 m) is plotted versus the normalized time (i.e., the elapsed time divided by the period of the inlet pressure T) for Case A (blue), Case B (red), Case C (green), and Case D (pink). The normalized pressure is shown as a solid black line as well.

As mentioned before, a larger amplitude is observed in Case B than in Case A owing to the increased inlet pressure, although their difference decreases as the time elapses. The oscillation periods for Cases A and B are close (i.e., 0.47 and 0.48 when measured from the wave crest to the wave trough) to that of the inlet pressure (0.5), but a phase lag is observed between the inlet pressure and the motions of the rod. For Case C, the same can be said of the oscillation period (0.52 when measured from the crest to the trough); however, when compared with Case B, a larger phase lag and a larger amplitude are observed, apparently owing to the 50% reduction in the modulus. In Case D, the period of the inlet pressure is reduced to half that of Case A. When the dynamics of the rod are shown versus the normalized time (note that this time, T, is 0.5 s and not 1 s), a much smaller amplitude and a dramatically increased phase lag are noted. This is because the rod does not respond well to such a high inlet pressure oscillation.

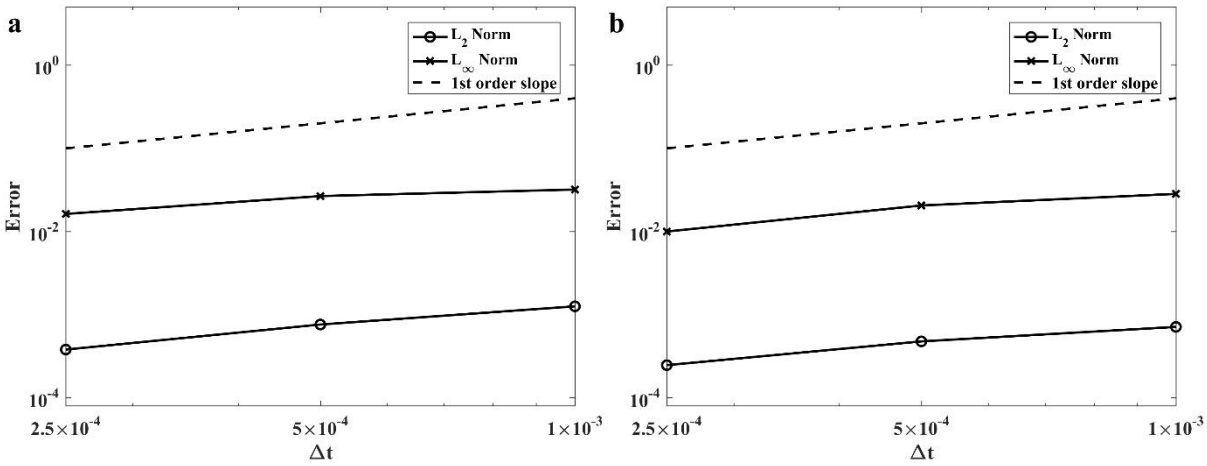

Figure 38. Temporal convergence results showing L_2 and L_∞ norms at t = 0.4 s for Case A: (a) x- and (b) y-component velocities

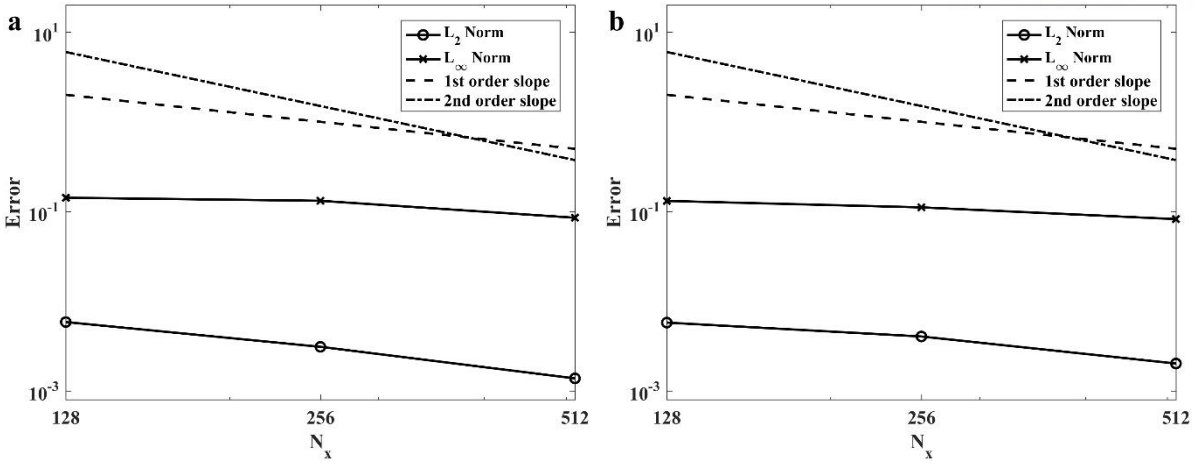

Figure 39. Grid refinement study results showing L_2 and L_∞ norms at t = 0.4 s for Case A: (a) x- and (b) y-component velocities

In this study, convergence tests for time and space were performed. Figure 38 shows the convergence rate in time. The results were obtained with a time step of 1×10^{-3} s, 5×10^{-4} s, 2.5×10^{-4} s, and 1.25×10^{-4} s. Here, the L_2 and L_∞ norms of the velocity field are calculated for Case A as

$$\|L_2\|(\Delta t) = \left(\frac{1}{N_x N_y} \sum_{i=1}^{N_x} \sum_{j=1}^{N_y} \left(\mathbf{u}(\Delta t) - \mathbf{u}(\Delta t = 1.25\times10^{-4}) \right)^2 \right)^{\frac{1}{2}}$$
$$\|L_\infty\|(\Delta t) = \max \left| \mathbf{u}(\Delta t) - \mathbf{u}(\Delta t = 1.25\times10^{-4}) \right| \quad (40)$$

where N_x and N_y are the numbers of grid points in the x- and y-directions. The error norms were computed over the entire domain at t = 0.4 s at which the fluid and rod both actively interact. The results show nearly first-order convergence in time as expected. A grid refinement was conducted using 128 × 64, 256 × 128, 512 × 256, and 1024 × 512 uniform Cartesian grids, the results of which are presented in Figure 39. In the same manner, the L_2 and L_∞ norms were calculated using Eq. (40), in which the reference value was obtained using 1024 × 512 grid. The results roughly show a first-order convergence, although the unified momentum equation was discretized using second-order schemes in space. It was conjectured that this reduction in accuracy was caused by a number of numerical issues, such the displacement extrapolation procedure applied, smeared interfaces, and the nature and complexity of the unified momentum equation (i.e., the Navier–Stokes equation and the elastodynamic equation are hybridized). The fluid-structure interface is diffused rather than sharp, and the accuracy reduction occurs near this smeared interface region. In addition, large structure deformation and vigorous interactions between fluid and structure are another cause of reduced accuracy. We believe that this accuracy problem could be remedied by using mesh adaptation near the interface.

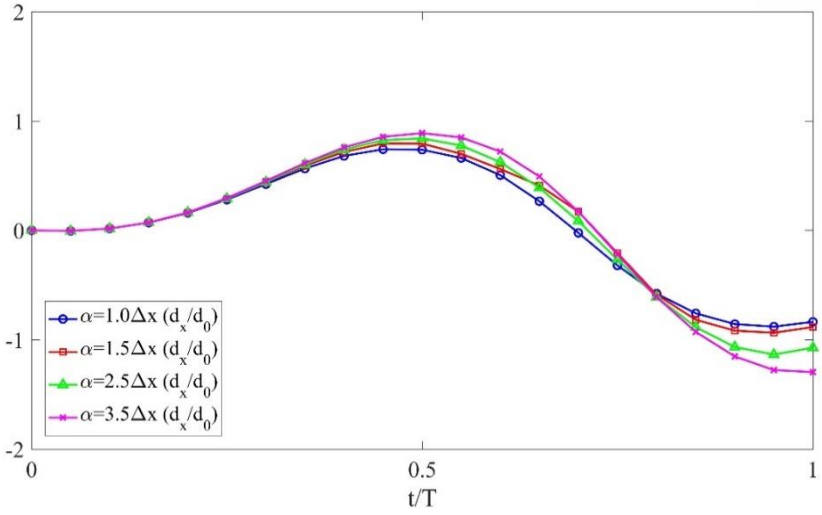

Figure 40. Normalized x-directional displacement of the rod tip versus normalized time for Case A with four different interface thickness.

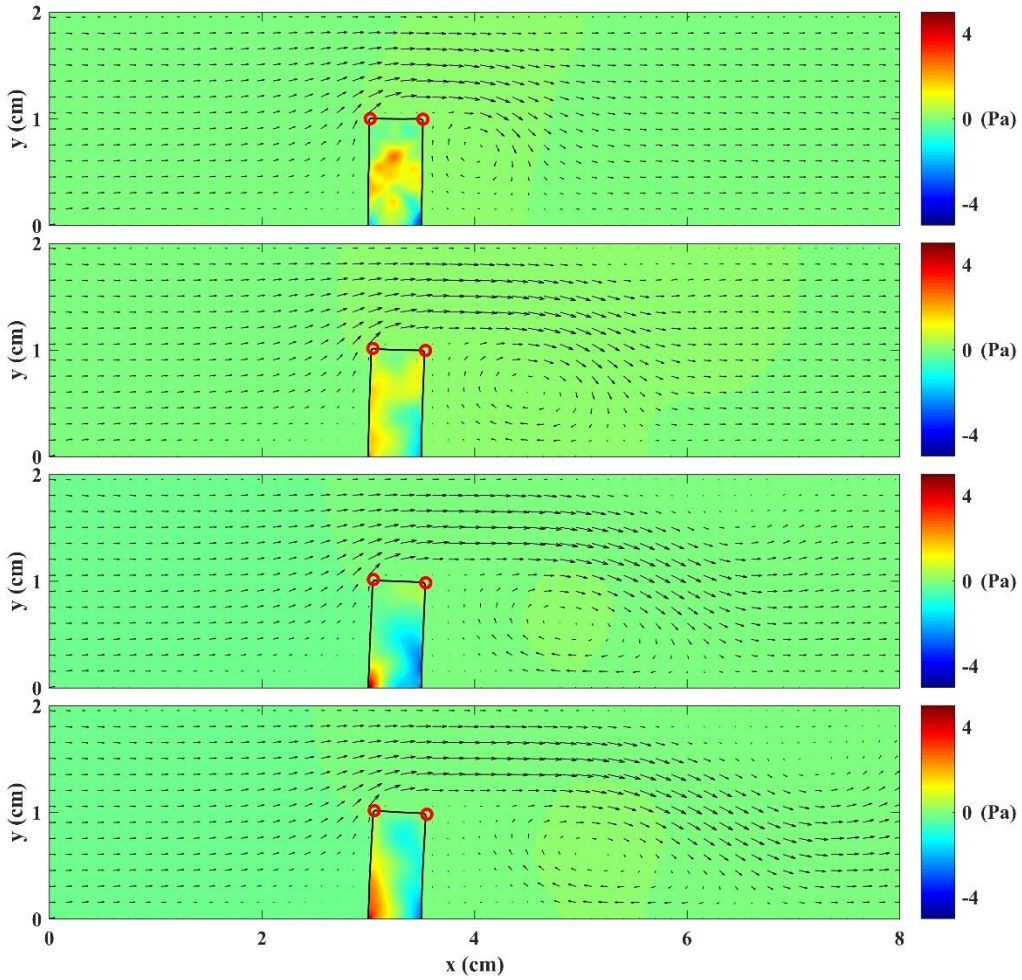

Figure 41. Shapes of the leaflet shown with the velocity and y-component normal stress (σ_{yy}) fields at t = 0.05, 0.1, 0.15, and 0.2 s where the red circles represent the upper corners of the leaflet obtained by Wang et al. [57].

In Figure 40, to investigate the effect of interface thickness, the simulation Case A of the flexible rod problem was performed by varying the interface thickness ($\alpha = 1.0\Delta x$, $1.5\Delta x$, $2.5\Delta x$, and $3.5\Delta x$). As more grid points used in the smearing interface, the sharp change in material properties become smoother and the stiffness of the system of equations is relieved. However, a thicker and overly diffused interface can lead to a less accurate result.

For validation purposes, the simulation result presented in Wang et al.'s study [57] was solved. In Wang et al.'s studies, the motions of a two-dimensional leaflet in a channel was solved by using numerical methods based on the immersed finite element method and the modified immersed finite element method where the coupling process of the original immersed finite element method was reversed [58]. In this work, the numerical result presented in [57] was used to verify the presented numerical method. In this numerical problem, a leaflet (1 cm in height and 0.5 cm in width) is positioned at 3 cm from the inlet and fixed at bottom of the channel (2 cm in height and 8 cm in width). The leaflet is modelled as a linear elastic material with $\rho = 1$ g/cm^3, $E = 1000$ dyn/cm^2, and $\nu = 0.3$, and the fluid is air with $\rho = 10^{-3}$ g/cm^3 and $\eta = 1.8 \times 10^{-4}$ g/cm·s. At the inlet, a constant velocity boundary condition ($u = 20$ cm/s) is applied. Figure 41 shows the simulation results obtained by the present study, where red circles represent the upper corners of the leaflet in Wang et al.'s result [57]. As shown, the simulation results are in good agreement with the results found in the literature.

3.3.3. Bouncing ball

As the third test example, a bouncing ball problem was simulated, and Figure 42 shows a schematic drawing of the problem with the coordinate system, boundary conditions, and dimensions. The container is filled with air at a density of 1 kg/m^3 and a viscosity of 2×10^{-5} kg/m·s. The dimensions of the container are 0.1 m × 0.1 m, and the diameter of the ball is 0.01 m. At the bottom of the container, a 0.02 m thick plate made of the same material as the ball is placed. Both the ball and floor have a density of 1,250 kg/m^3, Young's modulus of 10^6 N/m^2, and Poisson's ratio of 0.48. Owing to the symmetry, only the right half of the domain was used for the simulation. A no-slip boundary condition was applied at the top, bottom, and right boundaries, and the symmetry boundary condition was used at the left symmetry plane. Initially, the entire domain was stationary, and the gravitational force was applied to the entire domain. The acceleration due to gravity is 9.8 m/s^2.

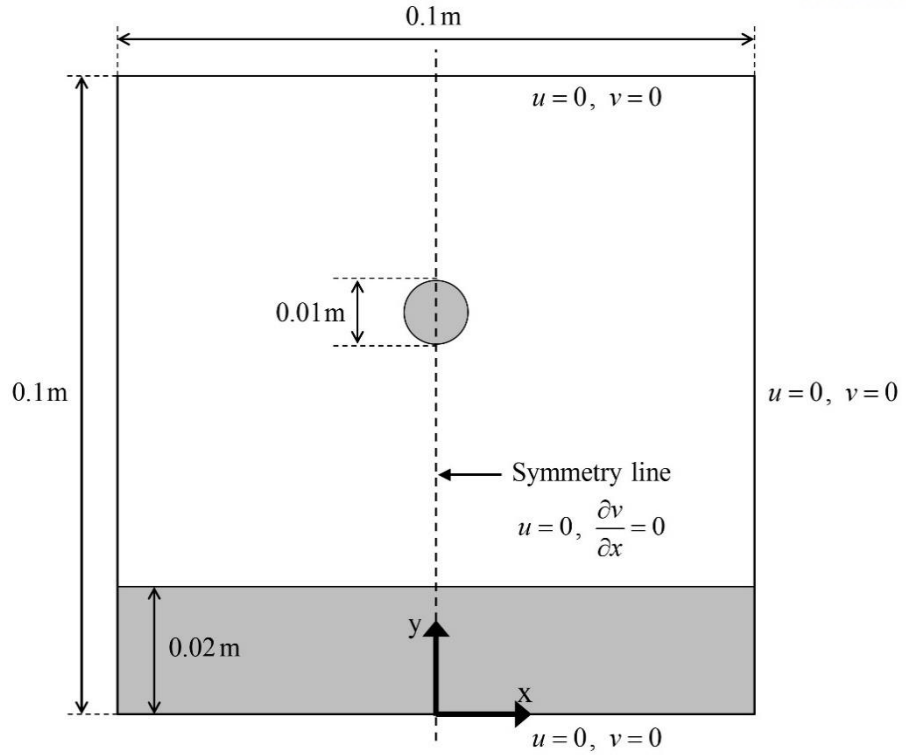

Figure 42. Schematic drawing of the bouncing ball problem. The coordinate system, boundary conditions, and dimensions are shown in the figure.

When applying the presented method to such a collision problem, we employed a wider smeared interface thickness than the previous two examples to avoid any numerical difficulties. Note that the actual interface is the zero-level set (ϕ = 0) evolved by the level set equation. During the collision process, however, the outer boundaries of the two structures ($\phi = \alpha$) first meet each other before a contact of the actual boundaries occurs. As the interfaces become closer, the elastic force increases and the ball eventually bounces back. If the smeared interface is too thin, two actual boundaries meet each other and the two structures merge together before the elastic force grows sufficiently for a bounce to occur. Owing to this issue, 3Δx was used for α in this problem (see Eq. (16)).

Table 2. Three simulation cases of the bouncing ball problem

Case	**Ball drop height**	***E***
A	0.06 m	10^6 N/m^2
B	0.08 m	10^6 N/m^2
C	0.08 m	2×10^6 N/m^2

In this study, three cases were simulated to see the effects of the ball drop height and the modulus of the structures, as summarized in Table 2. Case A is the reference case, and in Case B, the ball drop

height was increased by 33% from Case A, whereas in Case C, the modulus was doubled from Case B. Simulations were conducted on a 150 × 300 grid with a time step of 5×10^{-5} s.

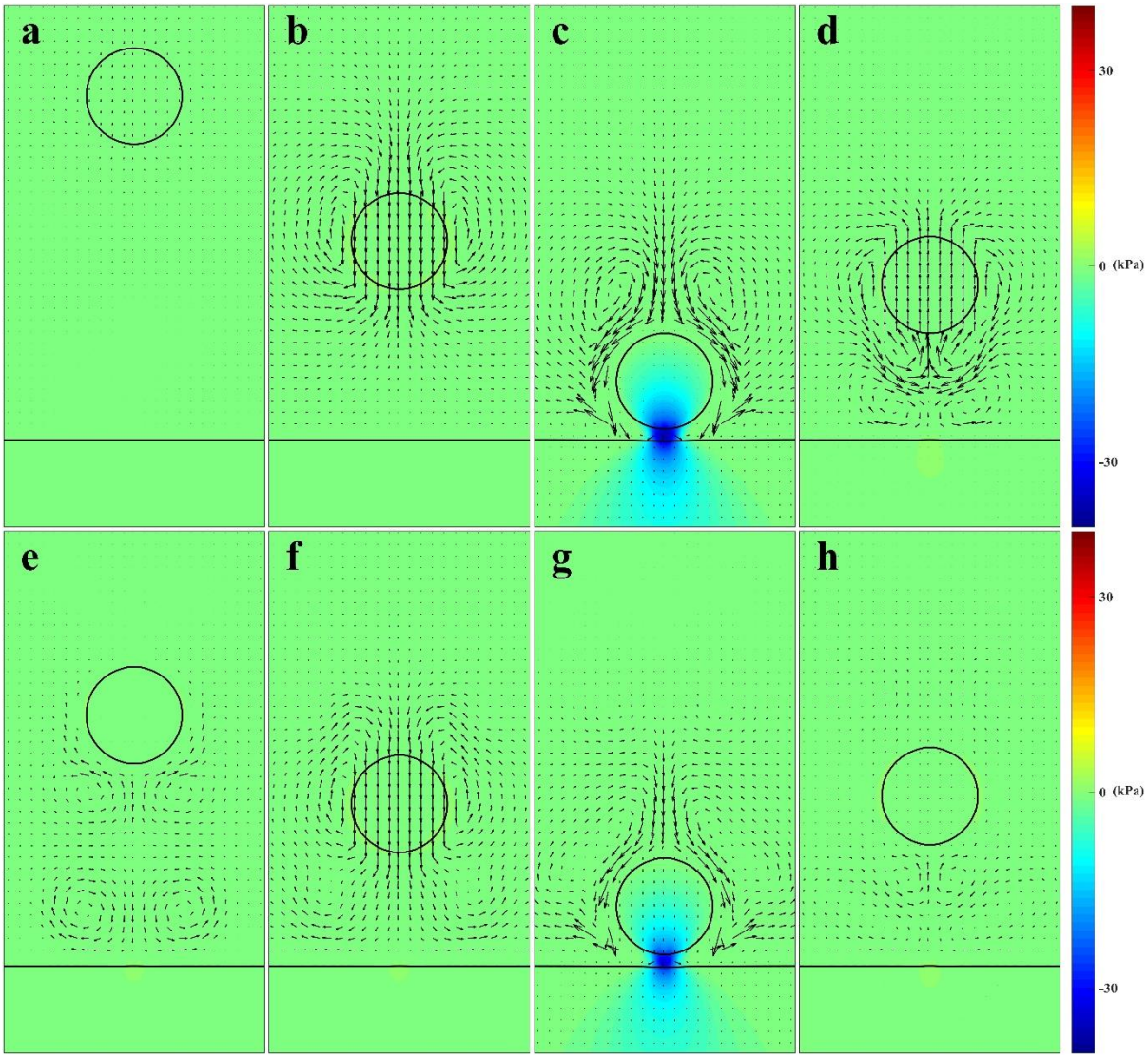

Figure 43. Results of Case A: Movement of the ball shown using the velocity and y-component normal stress (σ_{yy}) fields within the entire domain at t = (a) 0.01, (b) 0.06, (c) 0.083, (d) 0.104, (e) 0.156, (f) 0.202, (g) 0.224, and (h) 0.276 s.

Figure 43 shows the simulation results for Case A at t = 0.01, 0.06, 0.083, 0.104, 0.156, 0.202, 0.224, and 0.276 s, which are indicated using the y-component normal stress fields. Initially, the ball starts to fall under the gravitational pull, and over time is accelerated downward with a flow developing around the ball. When the ball collides with the floor at approximately t = 0.083 s (as shown in Figure 43. (c)), large compressive stresses are developed around the contact area. As the structures are compressed, elastic energy is stored and the ball bounces back, as shown in Figure 43.

(d). The upward movement of the ball becomes weakened owing to the gravitational pull and the ball reaches the maximum height at t = 0.156 s (Figure 43. (e)), which is smaller than the initial height. The ball then starts its second downward movement and collision, as shown in Figure 43. (f)–(h). Owing to the complex interaction between the fluid and structures, vorticities are formed around the ball. Upon the second collision, the compressive stresses are weaker than those in the first collision. The decrease in the maximum height of the ball after a collision is due to some of the kinetic energy being converted into elastic energy, which is used to deform the structures and is eventually dissipated through friction. If the frictional forces are assumed to be negligibly small, the coefficients of restitution for the first and second collisions (e_1 and e_2) are computed as $e_1 = \sqrt{h_1 / h_0}$ and $e_1 = \sqrt{h_2 / h_1}$, where h_0 is the initial drop height, h_1 is the maximum height after the first collision, and h_2 is the maximum height after the second collision. In Case A, e_1 is 0.851 and e_2 is 0.850. The coefficients of restitution after the first and second collisions are almost the same, which is reasonable because the energy loss from the interaction between the ball and air is small.

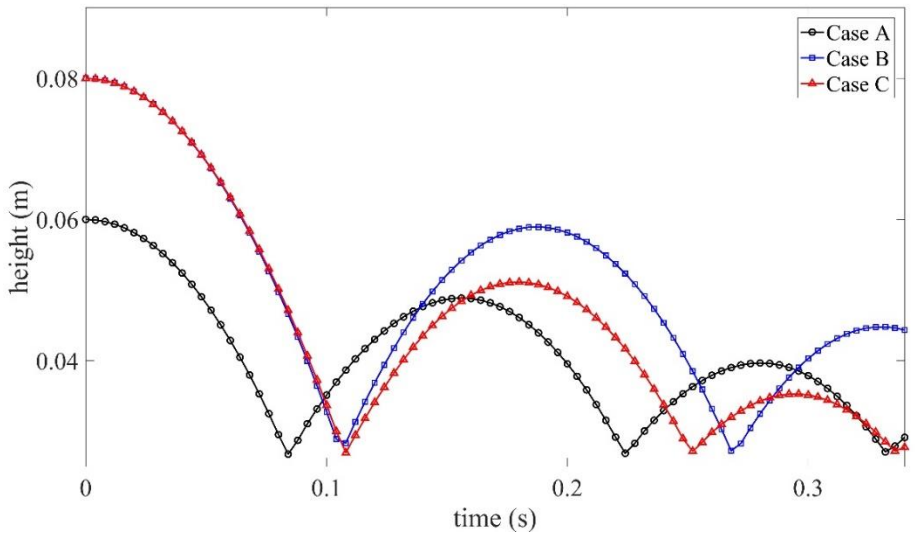

Figure 44. Height of the ball center versus time for Cases A–C.

The velocity and stress fields of Cases B and C are skipped, and Figure 44 shows the height of the ball plotted versus time for Cases A–C. As expected, the ball trajectories are parabolic, and the bounce height decreases as the number of collisions increases. In Case B, e_1 and e_2 were found to be 0.806 and 0.801, respectively. Note that the coefficients of restitution for the first and second collisions are sufficiently close (with a difference of less than 1%). In Case C, before the first collision, the interaction between the fluid and structures is identical to that of Case B. Upon collision, the ball is compressed by the impact and some of the kinetic energy of the ball is converted into elastic energy,

which is stored in the ball and absorbed by the floor. In Case C, the structures are stiffer than in Cases A and B, and consequently, the ball is less compressed. Therefore, the ball in Case C shows less bounces back, whereas the balls in Cases B and C have the same amount of kinetic energy when the balls hit the floor. In Case C, the coefficients of restitution for the two collisions (e_1 and e_2) are 0.720 and 0.706, respectively, which are also close. These values are much smaller than those of Cases A and B because of the increased stiffness. This implies that the presented method predicts the collision problems reasonably well.

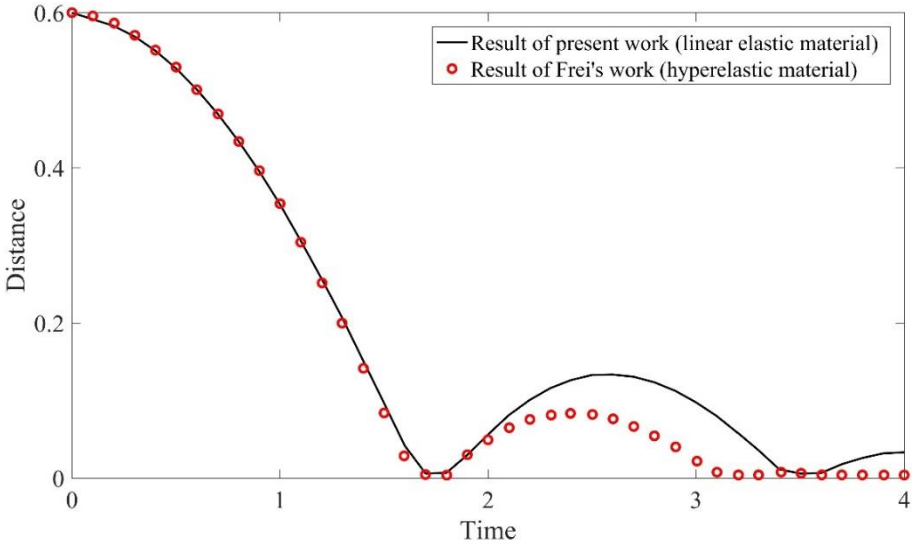

Figure 45. Distance of the ball from the bottom over time. Black solid line, results obtained by the presented method; red circles, results obtained by Frei [59]

In addition, the numerical method is validated by solving the bouncing ball problem presented in Frei's study [59], where the hyperelastic material model is applied to the solid ball. A ball of radius r = 0.4 is initially placed at x = 1, y = 1, in a rectangular container ($0 \le x \le 2$, $0 \le y \le 1.5$) and falls owing to gravity g = 1, where the gravitational force acts only on the structure. The ball has a density of ρ = 1,000 and Lame constants of $\mu = 2 \times 10^5$ and $\lambda = 8 \times 10^5$. The container is filled with a fluid with a density of ρ = 1,000 and a viscosity of η = 1. In Figure 45, the distance of the ball from the bottom is plotted versus time. Here, a linear elastic material model is used in the present study (black solid line) whereas a hyperelastic material model is used in previous studies (red circles). Before contact with the bottom occurs, the simulation results mostly coincide with Frei's results. However, owing to the different material model applied to the structure, the bounce heights of the ball differ from each other. For the hyperelastic ball, more energy is consumed in the deformation during the impact, and thus the bounce height is smaller than that of the linear elastic ball. In this problem, the collision occurs between the structure and the boundary, unlike in the previous problem in which the collision occurs between two structures, and the present method works well for both cases.

3.4. Conclusions

A novel, fully Eulerian method for the FSI problems of linear elastic solids and incompressible Newtonian fluids was presented and tested using various FSI problems. As demonstrated by the test examples, the proposed method is capable of not only predicting the dynamic interactions of fluids and structures, but also calculating the stress fields in the structures. Because this method is based on a unified momentum equation approach, which provides a strategy for hybridizing the momentum equations of solids and fluids into a single momentum equation structurally similar to a fluid momentum equation, a numerical method for the computational fluid dynamics can be employed.

4. Unified momentum equation approach for laser melting problem

This chapter includes the published contents:

H. Yeo, H. Ki*, Comput. Phys. Commun. 224 (2018) 230-244, Copyright © 2017 Elsevier B.V.

In this chapter, the numerical model for computing thermal residual stresses caused by laser melting process is presented. This numerical method is based on the unified momentum equation approach in Chapter 2 and Chapter 3.

4.1. Mathematical model

In this study, the material is assumed to be isotropic and a two-dimensional plane stress condition is used. Using these assumptions, we will derive the full governing equations in the following sections.

4.1.1. Unified momentum equation

To calculate thermal residual stresses, the unified momentum equation is slightly modified. The total strain tensor for structure is written as [60]

$$\boldsymbol{\varepsilon}_{tot} = \boldsymbol{\varepsilon}_e + \boldsymbol{\varepsilon}_t + \boldsymbol{\varepsilon}_v + \boldsymbol{\varepsilon}_p = \frac{1}{2}(\nabla \mathbf{d} + \nabla \mathbf{d}^T), \tag{41}$$

where $\boldsymbol{\varepsilon}_e$ is the elastic strain tensor, $\boldsymbol{\varepsilon}_t$ is the thermal strain tensor, $\boldsymbol{\varepsilon}_v$ is the strain tensor caused by volumetric change, $\boldsymbol{\varepsilon}_p$ is the plastic strain tensor, and $\mathbf{d}$ is the displacement vector. From Eq. (41), the elastic strain tensor is expressed as follows.

$$\boldsymbol{\varepsilon}_e = \frac{1}{2}(\nabla \mathbf{d} + \nabla \mathbf{d}^T) - \boldsymbol{\varepsilon}_t - \boldsymbol{\varepsilon}_v - \boldsymbol{\varepsilon}_p \tag{42}$$

Then, the coefficients and source term of unified momentum equation (Eq. (17)) is re-written as

$$\begin{aligned} \bar{\mu} &= \eta f_f + \mu \Delta t f_s \\ \bar{\lambda} &= \lambda \Delta t \, f_s \\ \bar{\mathbf{b}} &= -p\mathbf{I} \, f_f + \left\{ \mu\left(\nabla \mathbf{d}^o + \nabla \mathbf{d}^{oT}\right) + \lambda\left(\nabla \cdot \mathbf{d}^o\right)\mathbf{I} - 2\mu(\boldsymbol{\varepsilon}_t + \boldsymbol{\varepsilon}_v + \boldsymbol{\varepsilon}_p) - \left(\lambda \,\mathrm{Tr}(\boldsymbol{\varepsilon}_t + \boldsymbol{\varepsilon}_v + \boldsymbol{\varepsilon}_p)\right)\mathbf{I} \right\} f_s \end{aligned} \tag{43}$$

In this problem, solid, liquid, and mushy states can coexist in a computational cell, and the equation is expressed using the volume fractions of solid (f_s) and fluid (f_f). Here, the density is described in terms

of temperature. The unified momentum equation has been obtained in terms of velocity for all of solid, liquid and mushy states, such that a single numerical method for computational fluid dynamics can be used to solve the obtained momentum equation. In other words, this formulation is fully Eulerian for all phases, and the solid–liquid interface is traced automatically using the volume fraction information.

4.1.2. Solid-phase strain analysis

In this section, the strain terms in Eq. (41) will be examined. First, for an isotropic material, the thermal strain is written as [61]

$$\boldsymbol{\varepsilon}_t = \alpha(T - T_0)\mathbf{I}, \tag{44}$$

where α is the coefficient of thermal expansion, T is the temperature, T_0 is the ambient temperature.

The volumetric strain $\boldsymbol{\varepsilon}_v$ is the strain that is caused by the volume change when the material undergoes solid-state phase changes. For a heating process of steel, for example, the austenite transformation occurs above the A_3 temperature (920°C [62]), and a body centered cubic (b.c.c) structure changes into a face-centered cubic (f.c.c) structure, which causes a volume shrinkage. However, this transformation does not affect the residual stress development much [63] and was ignored in this chapter. To simplify the solid-state phase transformation phenomena, in this chapter, only the martensite transformation is considered, which is the most dominant mechanism and affects the volumetric strain most. This transformation occurs during a rapid cooling process, and the austenite phase is changed to the martensite phase, leading to an increase in volume. In this study, the Koistinen-Marburger equation for carbon steel [64] is adopted to calculate the volume fraction of martensite (f_m), which is written as

$$f_m = 1 - \exp\left[-0.011\left(M_s - T\right)\right] \quad \text{for} \, T \le M_s, \tag{45}$$

where M_s is the start temperature of the martensite transformation (440°C [62]). From this martensite volume fraction, the volumetric strain is calculated as

$$\boldsymbol{\varepsilon}_v = \theta f_m \mathbf{I}, \tag{46}$$

where θ is a material-specific constant and 1.5×10^{-3} is used for carbon steel [62].

In this study, the plastic strain $\boldsymbol{\varepsilon}_p$ is calculated using the rate-independent plastic model [65]. The von Mises yield criterion was used with a linear isotropic hardening rule where the yield function is expressed as follows [65].

$$f(\boldsymbol{\sigma}_s) = \left\| \boldsymbol{\sigma}_s - \frac{1}{3}\mathrm{Tr}(\boldsymbol{\sigma}_s)\mathbf{I} \right\| - \sqrt{\frac{2}{3}}\left(\sigma_Y + Ka\right) \tag{47}$$

Here, σ_Y is the yield stress, K is the isotropic hardening parameter, and a is the equivalent plastic strain. In the present study, the return mapping algorithm for plane stress is used to compute the

plastic strain [65]. In this algorithm, first, the yield criterion is checked by using Eq. (47) with a trial stress which is computed with the plastic strain of the previous time step. If the trial yield function is equal to or less than zero, there is no update for the plastic strain. In the case where the trial yield function is greater than zero, the plastic strain and equivalent plastic strain are updated as follows:

$$\boldsymbol{\varepsilon}_p = \Delta\gamma \mathbf{P}\boldsymbol{\Gamma}\left(\Delta\gamma\right)\boldsymbol{\sigma}_s^{trial} + \boldsymbol{\varepsilon}_p^o \tag{48}$$

$$a = \sqrt{\frac{2}{3}}\,\Delta\gamma\,\bar{f}\left(\Delta\gamma\right) + a^o \tag{49}$$

Here, $\boldsymbol{\sigma}_s^{trial}$ is the trial stress, $\boldsymbol{\varepsilon}_p^o$ is the plastic strain from the previous time step, and a^o is the equivalent plastic strain of the previous time step. Also, $\mathbf{P}$, $\boldsymbol{\Gamma}\left(\Delta\gamma\right)$, and $\boldsymbol{\sigma}_s^{trial}$ are given as

$$\mathbf{P} = \frac{1}{3}\begin{pmatrix} 2 & -1 & 0 \\ -1 & 2 & 0 \\ 0 & 0 & 6 \end{pmatrix},\ \boldsymbol{\Gamma}(\Delta\gamma) = \begin{pmatrix} \dfrac{3(1-\nu)}{3(1-\nu)+\Delta\gamma E} & 0 & 0 \\ 0 & \dfrac{1}{1+2\mu\Delta\gamma} & 0 \\ 0 & 0 & \dfrac{1}{1+2\mu\Delta\gamma} \end{pmatrix},\ \boldsymbol{\sigma}_s^{trial} = \begin{pmatrix} \sigma_{s,xx}^{trial} \\ \sigma_{s,yy}^{trial} \\ \sigma_{s,xy}^{trial} \end{pmatrix} \tag{50}$$

and $\bar{f}\left(\Delta\gamma\right)$ is written as

$$\bar{f}\left(\Delta\gamma\right) = \left\{ \frac{\left(\sigma_{s,xx}^{trial} + \sigma_{s,yy}^{trial}\right)^2}{6\left(1+\dfrac{E\Delta\gamma}{3(1-\nu)}\right)^2} + \frac{\frac{1}{2}\left(\sigma_{s,yy}^{trial} - \sigma_{s,xx}^{trial}\right)^2 + 2\left(\sigma_{s,xy}^{trial}\right)^2}{\left(1+2\mu\Delta\gamma\right)^2} \right\}^{\frac{1}{2}}, \tag{51}$$

where $\Delta\gamma$ is obtained by solving the following equation using the Newton's method.

$$\frac{1}{2}\bar{f}^2\left(\Delta\gamma\right) - \frac{1}{3}\left\{\sigma_Y + K\left(a^o + \sqrt{\frac{2}{3}}\Delta\gamma\,\bar{f}\left(\Delta\gamma\right)\right)\right\}^2 = 0 \tag{52}$$

Numerical details for obtaining the plastic strain can be found in [65].

4.1.3. Thermal analysis

In this study, an enthalpy-based energy equation with a convection term was used to calculate the temperature field, which is written as [66]

$$\frac{\partial H}{\partial t} + \nabla\cdot\left(\mathbf{u}H\right) = \nabla\cdot\left(k\nabla T\right) \tag{53}$$

where H is the enthalpy and k is the thermal conductivity. If specific heat c and density ρ are given as functions of temperature, the temperature-dependent enthalpy values for solid and liquid are calculated as

$$\begin{aligned} H_s &= \int_{T_{\text{ref}}}^{T} \rho c \, dT \\ H_f &= \int_{T_{\text{ref}}}^{T_s} \rho c \, dT + \rho L + \int_{T_l}^{T} \rho c \, dT \end{aligned}, \tag{54}$$

where T_{ref} is the reference temperature, L is the specific latent heat, T_s is the solidus temperature, and T_l is the liquidus temperature.

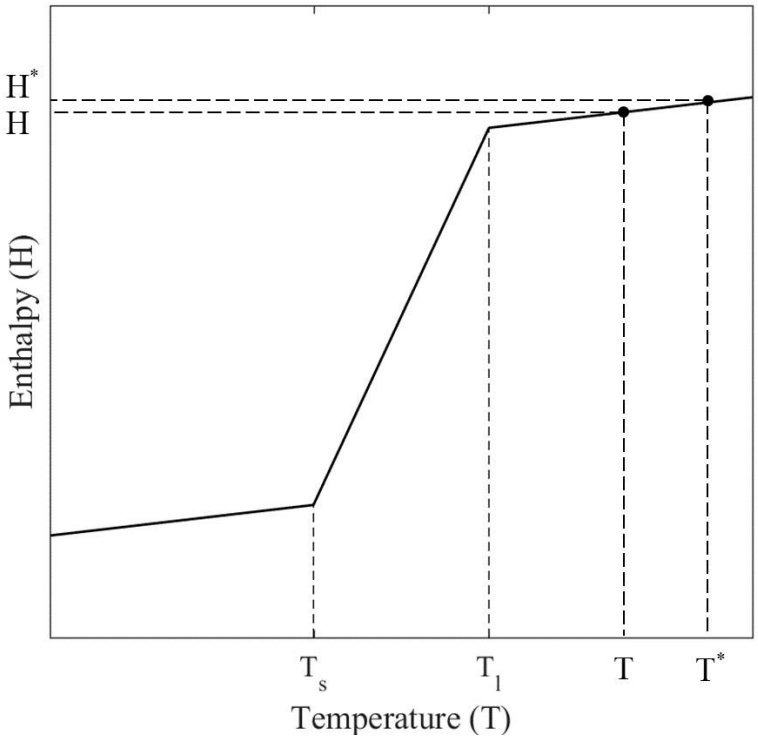

Figure 46. Enthalpy versus temperature for a material with a solid-liquid phase change.

Figure 46 shows a relationship between enthalpy and temperature near the melting temperature, and liquid and solid (mushy sate) can coexist between the liquidus and solidus temperatures. If a temperature value is given, liquid and solid volume fractions are obtained using liquidus and solidus temperatures as follows [66]:

$$f_f = \begin{cases} 0 & \text{if } T < T_s \\ \dfrac{T - T_s}{T_l - T_s} & \text{if } T_s \le T \le T_l \\ 1 & \text{if } T > T_l \end{cases} \tag{55}$$

$$f_s = 1 - f_f \tag{56}$$

Then, the enthalpy is expressed using volumes fractions as

$$H = H_s f_s + H_f f_f \tag{57}$$

4.2. Numerical algorithm

In this study, to simplify the algorithms, a two-dimensional plane stress assumption is employed, and the stress components involving the z-direction are set to zero. The overall algorithm is schematically shown in Figure 49.

4.2.1. Computational cells near the fluid-mushy zone interface

The unified momentum equation is discretized and solved in the same way as described in previous chapters. However, when evaluating the momentum fluxes (F_e, F_w, F_n, F_s in Eq. (19)) for a control volume near the fluid-mushy zone (or fluid-solid) interface, special care must be taken. Fluid velocity is much larger than solid velocity, which may cause numerical instabilities when velocities from both phases are used together to evaluate a velocity gradient. To resolve this issue, we considered a given momentum flux at a cell face as a *fluid* momentum flux if at least one of the solid volume fractions at four surrounding velocity locations are zero.

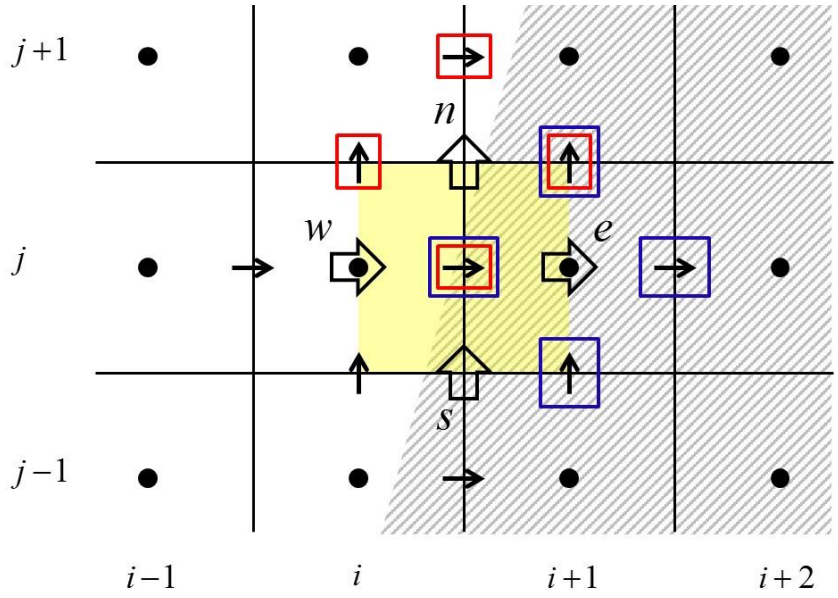

Figure 47. A u-velocity control volume near the fluid-mushy zone (or fluid-solid) interface, where the hatched region (right side) denotes the mushy zone (or solid) and the other region represents the fluid.

For example, let's consider a u-velocity control that is shown as a yellow square in Figure 47. In this figure, the hatched region on the right side represents a mushy zone (or solid region) and the left white-colored side is a fluid region. To evaluate the momentum flux at the north cell face of the control volume ($F_{i+1/2,j+1/2}$ in Eq. (19)), four solid volume fraction values surrounding the north cell face (which are shown as red boxes in Figure 47) need to be evaluated using interpolation as follows,

$$\begin{aligned} f_{s,(i,j+1/2)} &= 0.5\left(f_{s,(i,j)} + f_{s,(i,j+1)} \right) = 0 \\ f_{s,(i+1/2,j+1)} &= 0.5\left(f_{s,(i,j+1)} + f_{s,(i+1,j+1)} \right) > 0 \\ f_{s,(i+1/2,j)} &= 0.5\left(f_{s,(i,j)} + f_{s,(i+1,j)} \right) > 0 \\ f_{s,(i+1,j+1/2)} &= 0.5\left(f_{s,(i+1,j)} + f_{s,(i+1,j+1)} \right) > 0 \end{aligned}, \tag{58}$$

because volume fractions are defined at the locations represented by black solid circles. As shown from Eq. (58), the solid volume fraction at (i, j+1/2) is zero, so $F_{i+1/2,j+1/2}$ should be evaluated assuming that it is a pure fluid momentum flux, i.e., in Eq. (19),

$$\begin{aligned} \bar{\mu}_{i+1/2,\,j+1/2} &= \eta_{i+1/2,\,j+1/2} \\ \bar{b}_{i+1/2,\,j+1/2} &= 0 \end{aligned}. \tag{59}$$

In the case of the east-face momentum flux $F_{i+1,j}$, on the other hand, solid volume fractions at four surrounding velocity locations (shown as blue boxes in Figure 47) are evaluated as

$$\begin{aligned} f_{s,(i+1/2,j)} &= 0.5\left(f_{s,(i,j)} + f_{s,(i+1,j)} \right) > 0 \\ f_{s,(i+1,j+1/2)} &= 0.5\left(f_{s,(i+1,j)} + f_{s,(i+1,j+1)} \right) > 0 \\ f_{s,(i+1,j-1/2)} &= 0.5\left(f_{s,(i+1,j)} + f_{s,(i+1,j-1)} \right) > 0 \\ f_{s,(i+3/2,j)} &= 0.5\left(f_{s,(i+1,j)} + f_{s,(i+2,j)} \right) > 0 \end{aligned}, \tag{60}$$

and all of them are positive (meaning that they contain at least some amounts of solid). Therefore, the momentum flux $F_{i+1,j}$ is evaluated using Eq. (19) without any modification as

$$F_{i+1,j} = \left\{ \left(-\rho u u\right) + \left(2\bar{\mu} + \bar{\lambda}\right)\left(\frac{\partial u}{\partial x}\right) + \bar{\lambda}\left(\frac{\partial v}{\partial y}\right) + \bar{b} \right\}_{i+1,j} \Delta A_{i+1,j}$$

where

$$\begin{aligned} \bar{\mu}_{i+1,j} &= \eta_{i+1,j}\, f_{f,(i+1,j)} + \mu_{i+1,j} \Delta t f_{s,(i+1,j)} \\ \bar{\lambda}_{i+1,j} &= \lambda_{i+1,j} \Delta t\; f_{s,(i+1,j)} \\ \bar{b}_{i+1,j} &= -p_{i+1,j}\, f_{f,(i+1,j)} \\ &\quad + \left\{ \begin{array}{l} \left(2\mu_{i+1,j} + \lambda_{i+1,j}\right)\left(\dfrac{\partial d_x^o}{\partial x}\right)_{i+1,j} + \lambda_{i+1,j}\left(\dfrac{\partial d_y^o}{\partial y}\right)_{i+1,j} \\ -2\mu_{i+1,j}\left(\varepsilon_{t,xx} + \varepsilon_{v,xx} + \varepsilon_{p,xx}\right)_{i+1,j} - \left(\lambda_{i+1,j}\,\mathrm{Tr}(\boldsymbol{\varepsilon}_t + \boldsymbol{\varepsilon}_v + \boldsymbol{\varepsilon}_p)_{i+1,j}\right) \end{array} \right\} f_{s,(i+1,j)} \end{aligned}. \tag{61}$$

The momentum fluxes at the west and south cell faces ($F_{i,j}$ and $F_{i+1/2,j-1/2}$) can be evaluated in the same way. For the west momentum flux,

$$\begin{aligned} \bar{\mu}_{i,j} &= \eta_{i,j} \\ \bar{\lambda}_{i,j} &= 0 \quad \text{, and} \\ \bar{b}_{i,j} &= -p_{i,j} \end{aligned} \tag{62}$$

for the south face,

$$\begin{aligned} \bar{\mu}_{i+1/2,j-1/2} &= \eta_{i+1/2,j-1/2} \\ \bar{b}_{i+1/2,j-1/2} &= 0 \end{aligned} . \tag{63}$$

Using this method, momentum equations at any points inside the whole computational domain can be obtained.

4.2.2. Energy equation

To solve the energy equation in a finite volume framework, Eq. (53) is first integrated over a scalar control volume and the following equation is obtained.

$$\begin{aligned} \frac{\partial H}{\partial t}\Delta V_{i,j} = &\left\{k\left(\frac{\partial T}{\partial x}\right)-(uH)\right\}_{i+1/2,j}\Delta A_{i+1/2,j} \\ &-\left\{k\left(\frac{\partial T}{\partial x}\right)-(uH)\right\}_{i-1/2,j}\Delta A_{i-1/2,j} \\ &+\left\{k\left(\frac{\partial T}{\partial y}\right)-(vH)\right\}_{i,j+1/2}\Delta A_{i,j+1/2} \\ &-\left\{k\left(\frac{\partial T}{\partial y}\right)-(vH)\right\}_{i,j-1/2}\Delta A_{i,j-1/2} \end{aligned} , \tag{64}$$

Using a second-order central difference method in space and a first-order backward Euler method in time, Eq. (64) can be discretized as

$$\begin{aligned}\frac{H_{i,j}-H_{i,j}^{o}}{\Delta t}\Delta V_{i,j} = &\left\{k_{i+1/2,j}\left(\frac{T_{i+1,j}-T_{i,j}}{\Delta x}\right)-\left(uH\right)_{i+1/2,j}\right\}\Delta A_{i+1/2,j}\\ &-\left\{k_{i-1/2,j}\left(\frac{T_{i,j}-T_{i-1,j}}{\Delta x}\right)-\left(uH\right)_{i-1/2,j}\right\}\Delta A_{i-1/2,j}\\ &+\left\{k_{i,j+1/2}\left(\frac{T_{i,j+1}-T_{i,j}}{\Delta y}\right)-\left(vH\right)_{i,j+1/2}\right\}\Delta A_{i,j+1/2}\\ &-\left\{k_{i,j-1/2}\left(\frac{T_{i,j}-T_{i,j-1}}{\Delta y}\right)-\left(vH\right)_{i,j-1/2}\right\}\Delta A_{i,j-1/2}\end{aligned}, \tag{65}$$

Note that Eq. (65) involves both enthalpy $H_{i,j}$ (on the left hand side) and temperatures ($T_{i,j}$, $T_{i+1,j}$, $T_{i-1,j}$, $T_{i,j+1}$, $T_{i,j-1}$,) at the current time step, so in order to solve it implicitly the enthalpy must be expressed in terms of the corresponding temperature using the relationship between them as schematically shown in Figure 46. As shown in Figure 46, the enthalpy can be expressed as a function of temperature, i.e., $H_{i,j}=H(T_{i,j})$, and can be approximated as [66]

$$H_{i,j} \approx H_{i,j}^{*} + \left.\frac{dH}{dT}\right|_{H_{i,j}^{*}} \left(T_{i,j}-T_{i,j}^{*}\right), \tag{66}$$

where dH/dT is the slope of the enthalpy-temperature graph (See Figure 46). In this study, Eq. (66) is solved together with Eq. (65) using an iterative method by considering the variables with a superscript * as previous iteration step variables, and then Eq. (65) can be cast into the following standard discretized form:

$$a_{i,j}T_{i,j} = \sum\nolimits_{nb} a_{nb}T_{nb} + S_{i,j} \tag{67}$$

4.2.3. Extending the displacement field to newly solidified regions

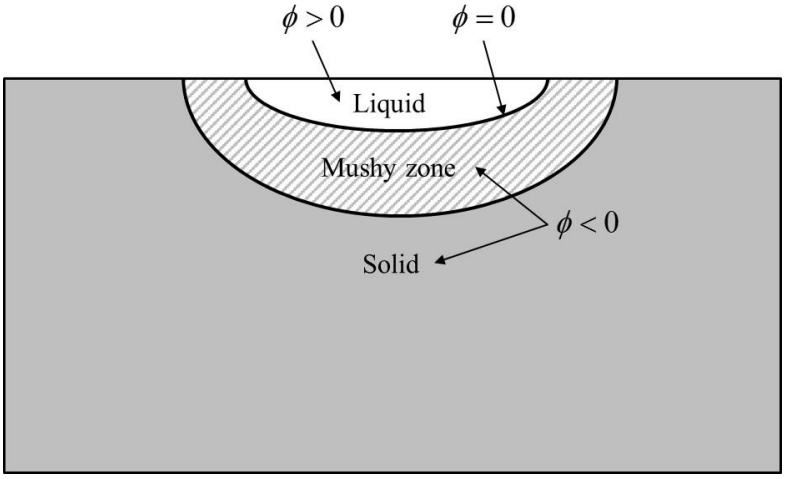

Figure 48. A problem where a mushy zone exists between solid and liquid regions. Level set function ϕ is defined with the zero level set ($\phi = 0$) located at the liquid-mushy zone interface.

When an originally fluid cell becomes a solid or mushy zone cell due to solidification, a proper value of displacement must be assigned there because otherwise the elastic strain cannot be properly evaluated. In order to solve this problem, we extended the displacement field of the nearby solid or mushy zone to newly solidified regions by employing a level set based method [46]. We defined a level set function ϕ as a signed normal distance from the fluid-mushy zone interface (T=T_l) as follows:

$$\phi = \begin{cases} +\text{distance}, & \text{for } T > T_l \\ 0, & \text{for } T = T_l \\ -\text{distance}, & \text{for } T < T_l \end{cases} \tag{68}$$

Using the level set function, the displacement field was copied from the neighboring mushy and solid regions to the fluid region by solving the following equation [53]:

$$\frac{\partial \mathbf{d}}{\partial \tau} + U(f_s)\mathbf{n} \cdot \nabla \mathbf{d} = 0 \tag{69}$$

Here, τ is the fictitious time and U is the unit Heaviside function.

$$U = \begin{cases} 1, & \text{if } f_s = 0 \\ 0, & \text{if } f_s > 0 \end{cases} \tag{70}$$

Only a few iterations are required for Eq. (69) because in one small time step mushy zone (or solid) cells can appear only very near the interface.

In this study, the actual liquid-mushy zone interface was not moved by using the level set method, but by updating the fluid volume fraction (Eq. (55)) after the energy equation is solved. The level set function was only used for extending the displacement field. However, when the liquid-mushy zone interface moves due to melting and solidification, the level set function still needs to be reinitialized according to its definition of signed distance function. For reinitialization, in this study, the following well-known equation was solved [46].

$$\frac{\partial \phi}{\partial \tau} = \mathrm{S}(\phi_0)\left(1 - |\nabla \phi|\right) \tag{71}$$

Here, S(ϕ_0) represents the sign of a temporary level set function ϕ_0, which is defined as

$$\mathrm{S}(\phi_0) = \frac{\phi_0}{\sqrt{\phi_0^2 + \varepsilon^2}}, \tag{72}$$

where the sign of ϕ_0 can be correctly determined from the temperature field (See Eq. (68)) and $\varepsilon = \Delta x$ was used in this study. The implementation details can be found in [46]. Using this method, the displacement field is extended to the adjacent fluid region in the direction perpendicular to the interface and the displacement field becomes continuous across the interface.

Note that, in this study, plastic strain and equivalent plastic strain terms were set to zero for newly formed solid cells because plasticity history is lost upon melting.

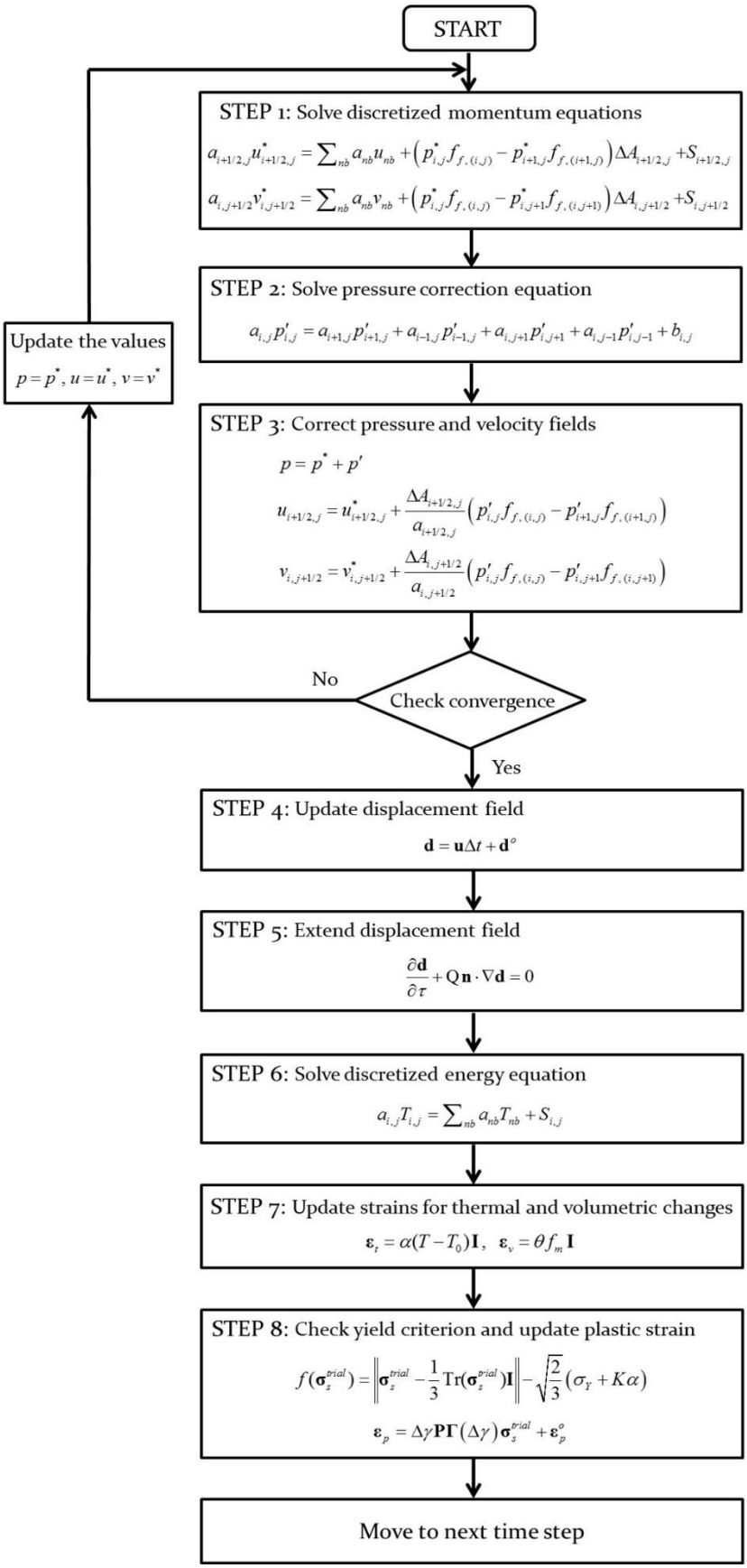

Figure 49. Overall numerical algorithm used in this study

4.3. Numerical examples

To test the proposed numerical method, a two-dimensional laser heating problem was considered, where a carbon steel sheet was heated by a laser beam with a spatially Gaussian energy distribution (See Figure 50). When a high-intensity laser beam is irradiated on the top surface of a material, the material gets heated up, and melting occurs from the irradiated surface and the melting front propagates inward. When the laser beam is turned off, now the melting stops and the molten liquid becomes re-solidified as the heat is removed due to conduction, convection and radiation until the entire specimen is cooled down to the room temperature.

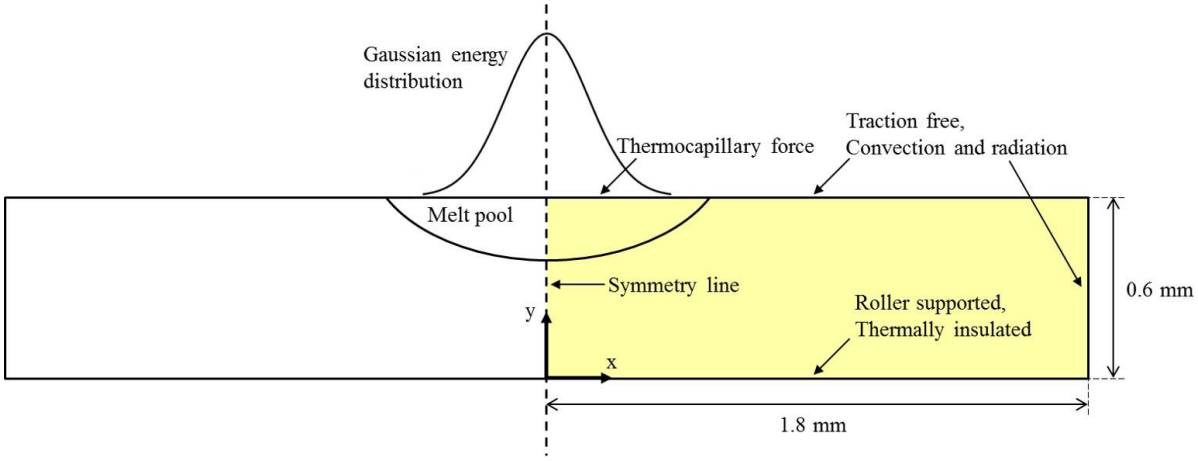

Figure 50. Schematic drawing of the validation problem. Boundary conditions are shown at the corresponding locations and only the right half was used as the actual computational domain due to symmetry (a yellow-colored region).

A schematic view of the problem is shown in Figure 50. In this study, a 3.6 mm × 0.6 mm carbon steel specimen is heated at the center of the top surface, and due to symmetry, only the right half is taken as the computational domain employing a symmetry boundary condition on the left side. The Gaussian laser beam is modeled as a heat flux at the top surface, which is mathematically written as

$$q_{laser} = \frac{2P}{\pi R_b^2} \exp\left(-\frac{2x^2}{R_b^2} \right), \tag{73}$$

and is implemented as a boundary condition for the energy equation. Here, P is the laser power, and R_b is the beam radius. In this study, a laser beam with a laser power of 4 kW and a beam diameter of 0.25 mm is assumed as a heating source. Heat losses due to convection and radiation are considered at the top and right boundaries using

$$q_{loss} = h\left(T_s - T_0\right) + \varepsilon\sigma\left(T_s^4 - T_0^4\right), \tag{74}$$

where h is the convection heat transfer coefficient (50 W/m^2·K), T_s is the surface temperature, T_0 is the ambient temperature (20°C), ε is the emissivity (0.2), and σ is the Stefan-Boltzmann constant (5.67×10^{-8} W/m^2·K^4). The bottom surface is assumed thermally insulated.

For the momentum equations, boundary conditions are selectively applied depending on the state at the given boundary location. Basically, a symmetry boundary condition is applied to the left side, the bottom side is assumed to be roller-supported, and at top and right sides, traction free boundary conditions are employed. Once liquid appears on the boundary due to melting, the thermocapillary effect is accounted for by implementing the following equation,

$$\boldsymbol{\sigma}_f \cdot \mathbf{n} = \nabla_s T \frac{d\gamma}{dT}, \tag{75}$$

where $\mathbf{n}$ is the surface unit normal vector, ∇_s is the surface gradient, and γ is the surface tension. As well known, surface tension is a function of temperature, and when a temperature gradient exists on the melt pool surface, a force is generated, pulling the liquid to a lower temperature region [67].

In this study, POSTEN80 steel is assumed as the specimen material, and the mechanical and thermal properties of the steel are taken from [62] and are summarized in Table 3 and Figure 51. The minimum values of Young's modulus and the yield stress at the liquidus temperature are set to 5 GPa and 5 MPa, respectively [62] (See Figure 51).

Table 3. Material properties of POSTEN80

Property	**Value**
Poisson's ratio (ν)	0.3
Coefficient of thermal expansion (α)	1.2×10^{-5}/K
A_3 temperature	920°C
M_s temperature	440°C
Specific latent heat (L)	270 kJ/kg
Solidus temperature (T_s)	1450°C
Liquidus temperature (T_l)	1500°C
Viscosity (η) ([67])	4.25×10^{-3} kg/m·s
dγ/dT ([67])	4.5×10^{-4} N/m·K

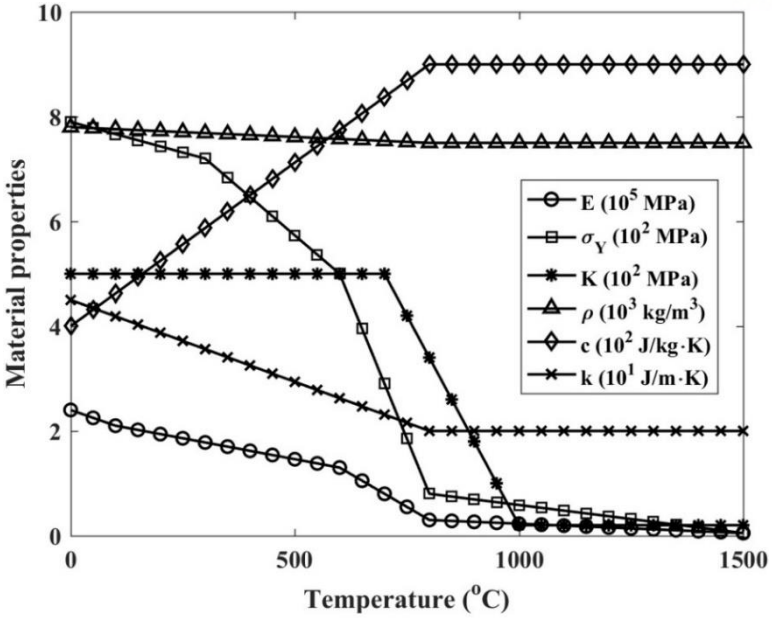

Figure 51. Temperature-dependent properties of POSTEN80 (taken from [62])

In this study, this problem was tested on a 180×60 uniform Cartesian grid. Time step was determined such that the maximum change in enthalpy in one time step is 252500 kJ/m^3, which corresponds to temperature change of 30°C for liquid phase. The maximum time step was set to 0.05 s.

4.3.1. Effect of solid strain terms and fluid flow on residual stress development

In this section, we first investigated the effect of thermal strain, volumetric strain, plastic strain, and fluid flow on residual stress development by adding those terms in the momentum equations as summarized in Table 4. As shown in the table, first, thermal strain was only considered, and then plastic and volumetric strains were successively added to the momentum equations. For the first three cases, fluid flow was simulated, but in Case D, it was not in order to understand the effect of fluid flow. For all cases, a laser heating time of 0.03 s was assumed.

Table 4. Four simulations performed to study the effect of various strains and fluid flow

Case	ε_t	ε_p	ε_v	Fluid flow
A	O	X	X	O
B	O	O	X	O
C	O	O	O	O
D	O	O	O	X

Figure 52 and Figure 53 present the stress and temperature fields simulated using the condition shown in Case A. Figure 52 shows normal stress components in *x*- and *y*-directions right after the laser heating is finished, i.e., at the end of a 0.03 s laser pulse, together with the corresponding temperature distribution. Note that in Figure 52, stress fields are shown with the velocity fields. As the temperature increases due to the laser heating, the steel becomes soft and eventually molten in the heating zone where almost zero stress is observed. In the surrounding region, compressive stresses (both in *x*- and *y*-directions) are formed to resist the expansion of the heating area. To balance the overall stress state of the structure, *x*-directional tensile stresses are developed in the bottom region and *y*-directional tensile stresses appear right outside the middle region. Due to the thermocapillary force, a melt flow is developed from the top surface, which eventually forms recirculating zones. Also, the temperature field in Figure 52. (c) appears to be strongly affected by the melt flow. Figure 53 shows the stress and temperature distributions when the steel specimen has been completely cooled down to the ambient temperature. As expected, no residual stress is observed because volumetric strain (due to martensitic transformation) and plastic strain were not considered.

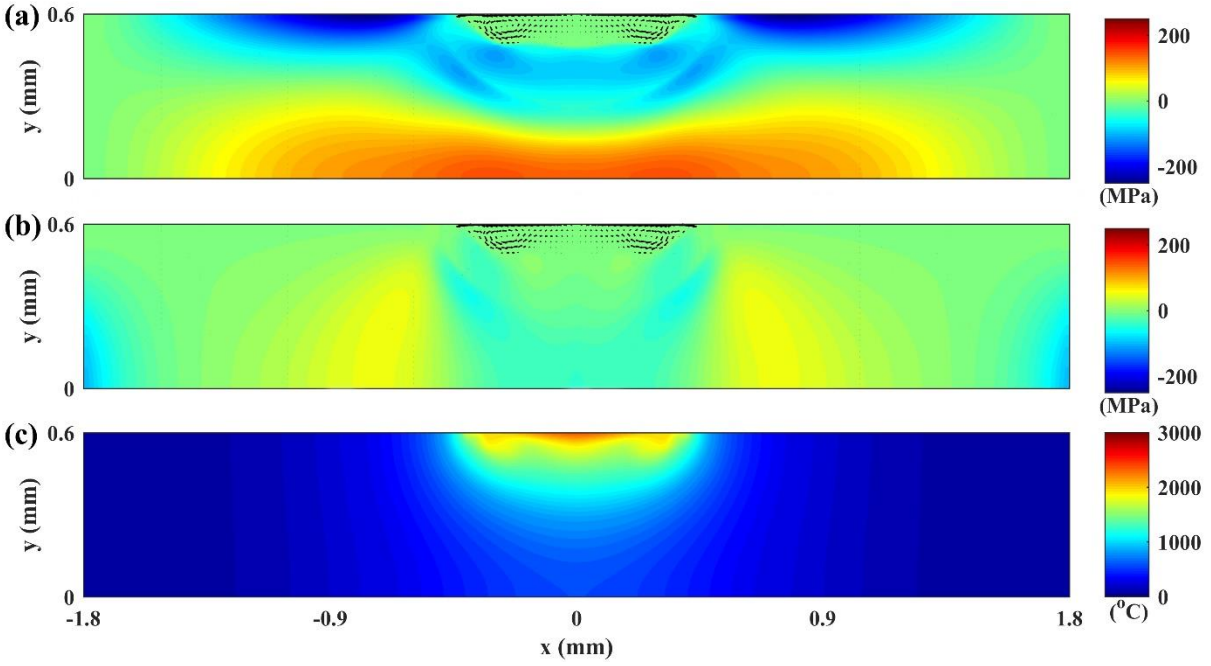

Figure 52. Stress and temperature fields for Case A right after the laser heating (laser pulse) is finished. (a) Normal stress in the x-direction, (b) Normal stress in the y-direction, (c) Temperature

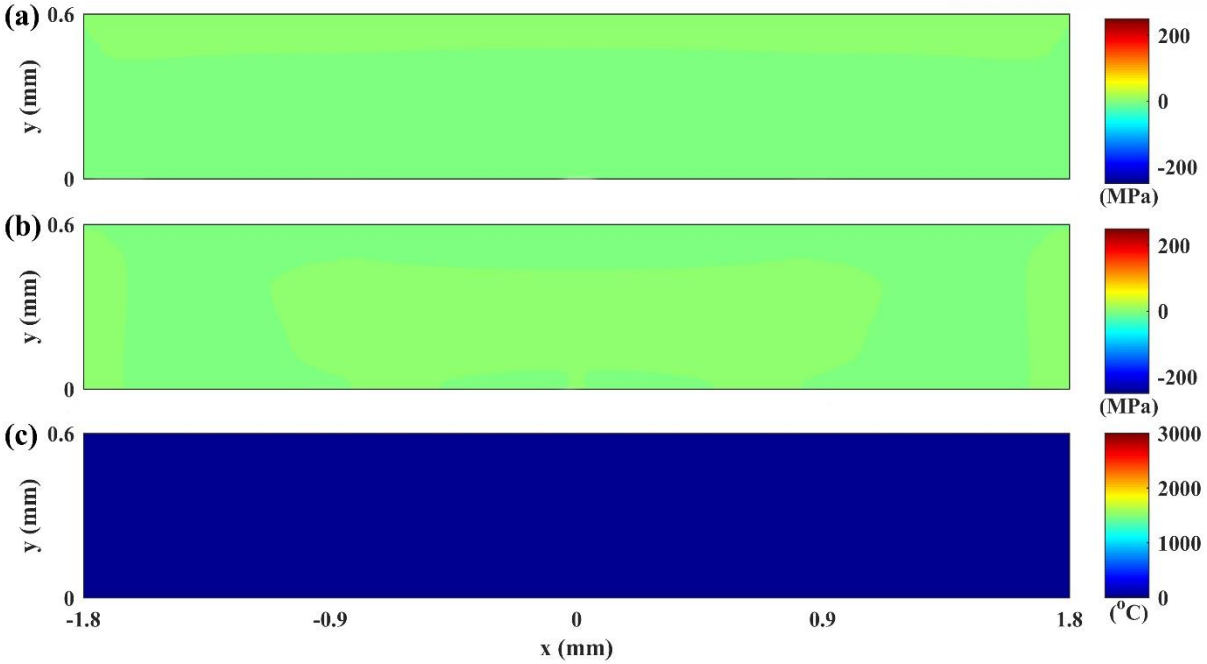

Figure 53. Stress and temperature fields for Case A after the material has been completely cooled down to the ambient temperature. (a) Normal stress in the x-direction, (b) Normal stress in the y-direction, (c) Temperature

Figure 54 and Figure 55 show the stress and temperature fields for Case B, which were obtained by adding the plastic strain to the previous simulation. Figure 54 presents normal stress components in *x*- and *y*-directions and the corresponding temperature distribution right after the laser heating is finished. As shown, the overall stress distributions are similar to those in Case A, i.e., compressive stresses are formed near the heating zone and tensile stresses are generated below to maintain the force balance. The main difference is that now due to the plastic strain which is in effect near the heating region, the stress level there has been much lowered. For example, the compressive stresses near the melt pool in Figure 54. (a)(Case B) are shown to be considerably decreased compared to those shown in Figure 52. (a)(Case A). Figure 55 shows the stress and temperature distributions when the steel specimen has been completely cooled down to the ambient temperature. As shown, the influence of plastic strain can be clearly noticed as residual stresses are developed inside the steel specimen. When temperature goes down, the thermally expanded material starts to contract again and the generated plastic strain (which has reduced the compressive stress level during the heating process) now induces tensile stresses in the heated region as shown in Figure 55. (a),(b). Also, compressive stresses are formed outside the tensile stress region. Note that the magnitude of the final residual stresses appears to be larger than what is shown in Figure 54 because the steel becomes softened at elevated temperatures.

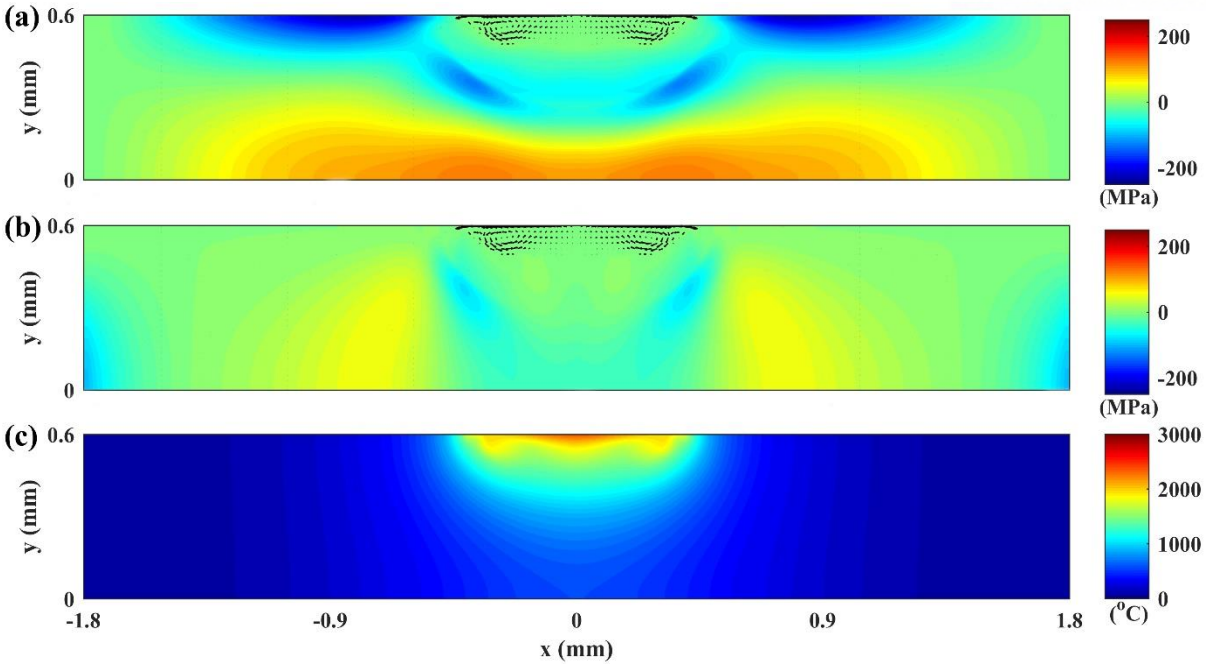

Figure 54. Stress and temperature fields for Case B right after the laser heating (laser pulse) is finished. (a) Normal stress in the x-direction, (b) Normal stress in the y-direction, (c) Temperature

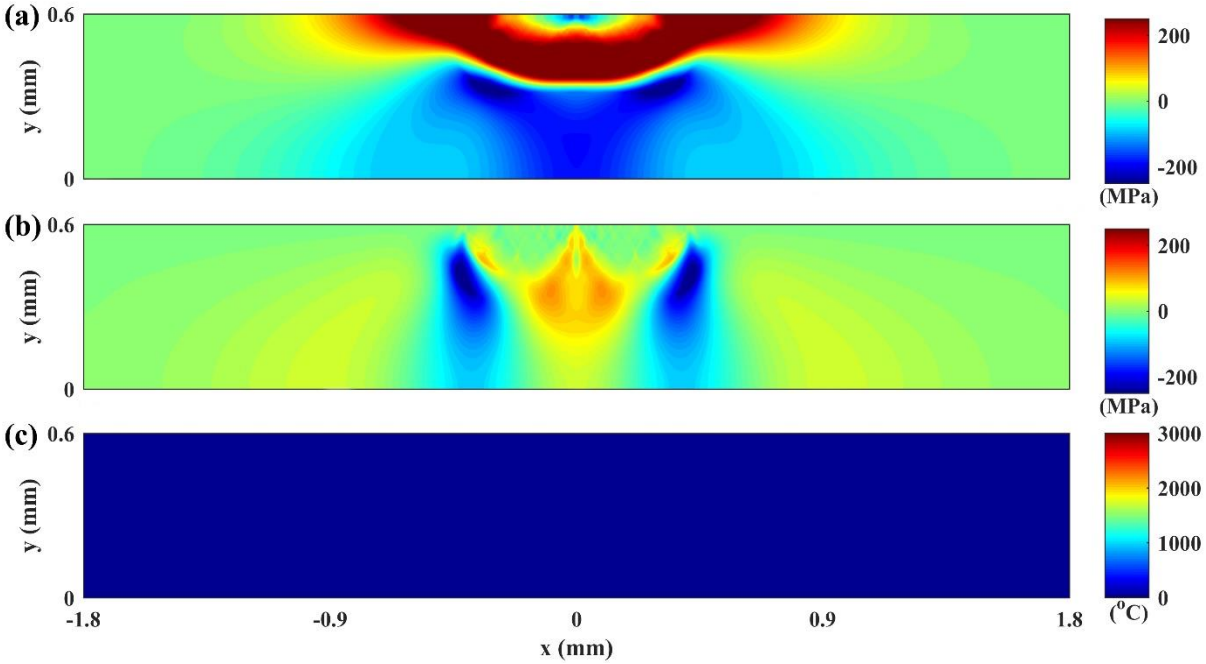

Figure 55. Stress and temperature fields for Case B after the material has been completely cooled down to the ambient temperature. (a) Normal stress in the x-direction, (b) Normal stress in the y-direction, (c) Temperature

In Figure 56 and Figure 57, the stress and temperature fields for Case C are presented, which were obtained by additionally considering the volumetric strain due to martensite phase transformation. In this simulation, therefore, all major physical phenomena for residual stress development were accounted for. Figure 56 presents normal stress components in *x*- and *y*-directions and the corresponding temperature distribution right after the laser heating is finished. During the heating process, apparently, stress distributions are the same as those shown in Figure 54 (Case B) because martensite forms only during the cooling process. As the temperature decreases and martensite forms, the steel expands and the resulting volume increase counteracts the volume contraction due to the temperature drop. Consequently, the martensitic transformation tends to mitigate residual stresses, and therefore, the overall stress level in Figure 57 is apparently lower in comparison to that in Figure 55. In Figure 57. (d), the distribution of martensite after cooling is shown as a red-colored region, and in Figure 57. (a), (b), the boundary of this region can be observed.

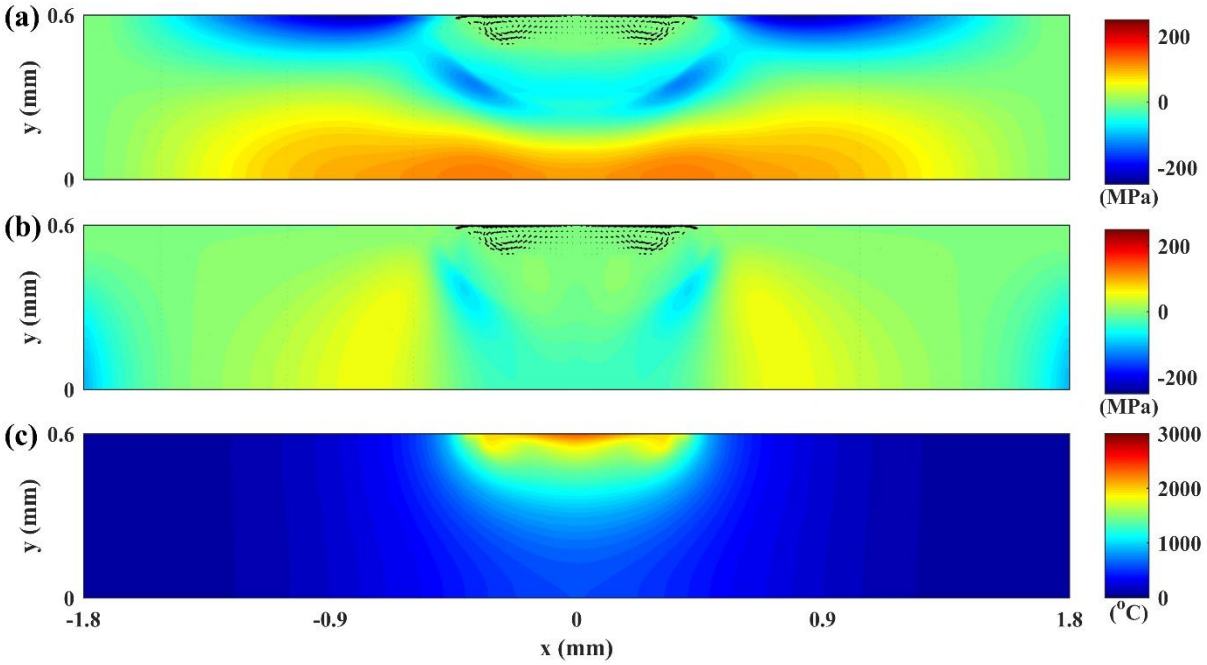

Figure 56. Stress and temperature fields for Case C right after the laser heating (laser pulse) is finished. (a) Normal stress in the x-direction, (b) Normal stress in the y-direction, (c) Temperature

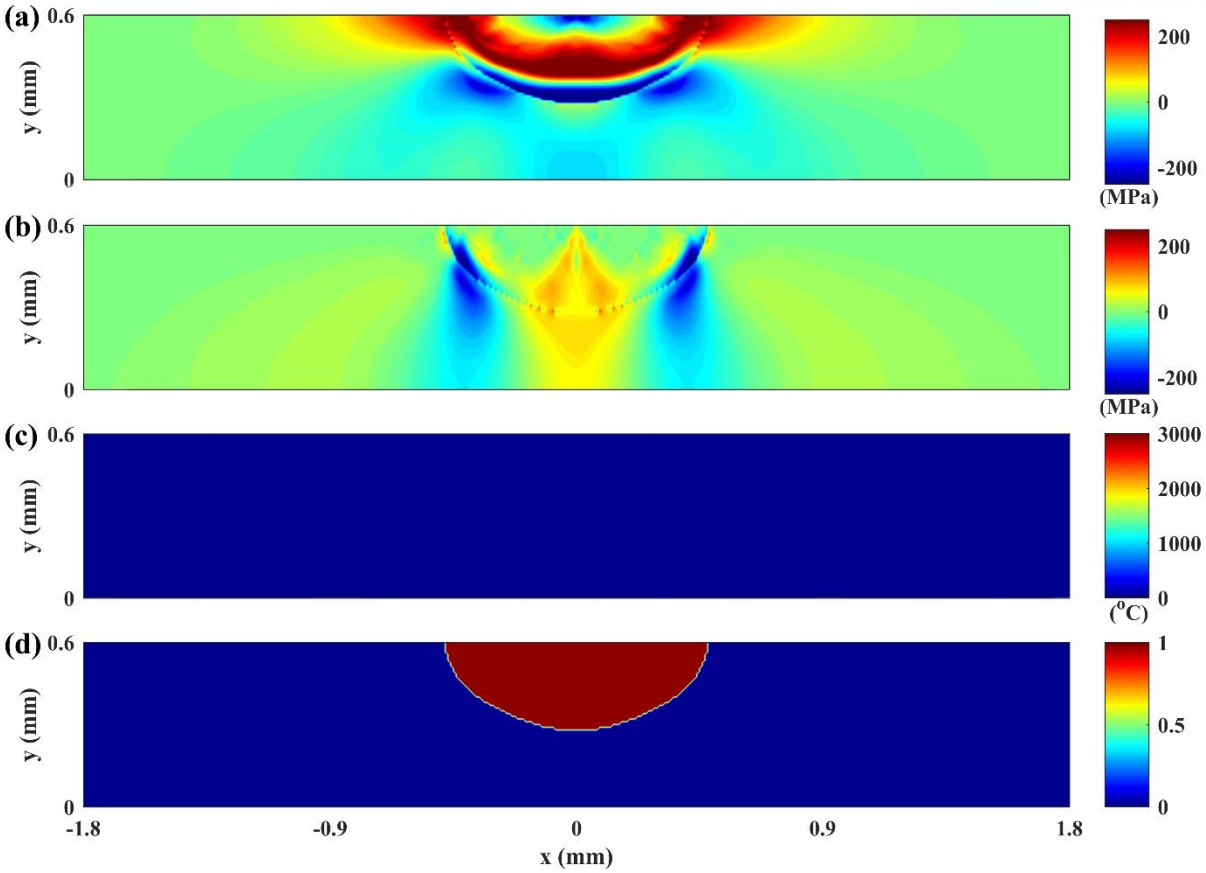

Figure 57. Stress, temperature, and martensite distributions for Case C after the material has been completely cooled down to the ambient temperature. (a) Normal stress in the x-direction, (b) Normal stress in the y-direction, (c) Temperature, (d) Martensitic phase distribution (represented as a red-colored region)

In Case D, the effect of melt flow was studied by neglecting solid-liquid phase changes and fluid flow from Case C. However, all the major causes for residual stress development were considered. Figure 58 and Figure 59. (a-c) show the stress and temperature fields, and in Figure 59. (d), the distribution of martensite after cooling is shown as a red-colored region. Compared with Case C, the biggest difference is that the temperature distribution (Figure 58. (c)) and the martensite region (Figure 59. (d)) both become circular (i.e., deeper but narrower compared to Case C) when flow motions are ignored. The flow is mainly in the horizontal direction, so this result is not surprising. Therefore, considering the fluid flow is critical for the accurate prediction of residual stresses.

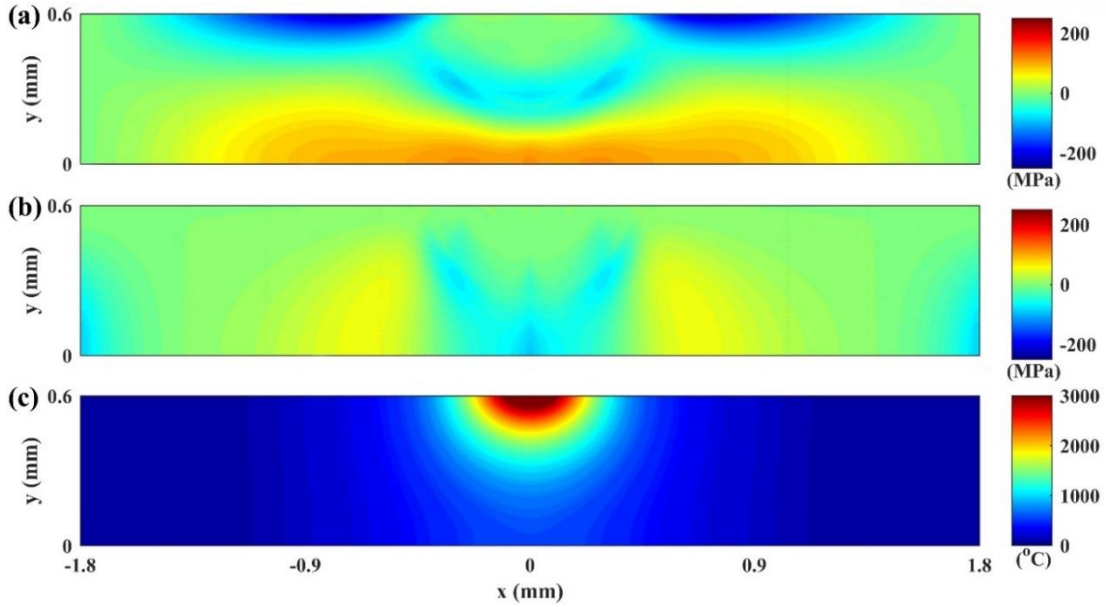

Figure 58. Stress and temperature fields for Case D right after the laser heating (laser pulse) is finished. (a) Normal stress in the x-direction, (b) Normal stress in the y-direction, (c) Temperature

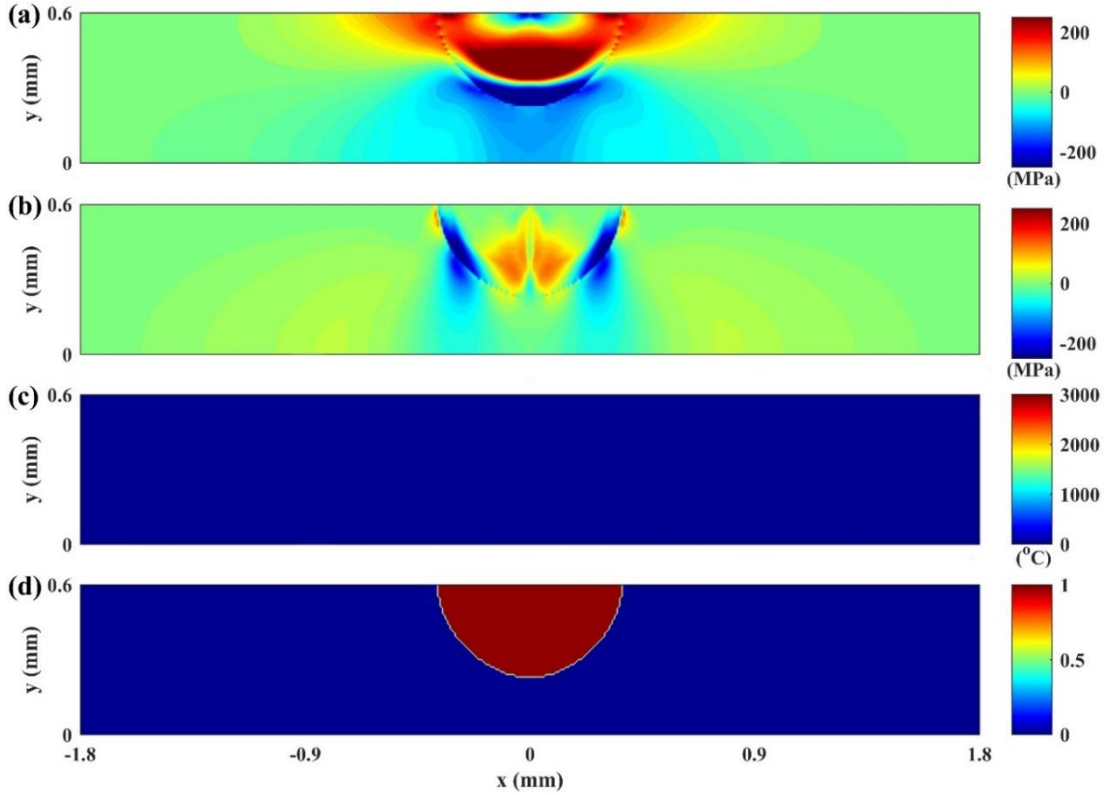

Figure 59. Stress, temperature, and martensite distributions for Case D after the material has been completely cooled down to the ambient temperature. (a) Normal stress in the x-direction, (b) Normal stress in the y-direction, (c) Temperature, (d) Martensitic phase distribution (represented as a red-colored region)

4.3.2. Effect of laser heating time on residual stress development

So far, laser heating time has been fixed at 0.03 s for all simulations. In this section, to study the effect of laser heating time, we simulated with a laser heating time of 0.05 s, also considering all of strain terms and fluid flow. In Figure 60~Figure 61, simulation results for the longer heating time (0.05 s) are presented. Compared with Figure 56~Figure 57 (0.03 s heating time results), we can notice that almost everything, including the melt pool size, the size of martensite formation region, and the range of the developed stress field, is proportional to the heating time although overall distributions are similar in shape. When the laser beam irradiates for 0.05 s, residual stresses are substantially stronger and more widely distributed as more energy is supplied to the material. Note that the amount of laser energy is proportional to the heating time because the laser power is fixed in this study. Also, the martensite region has reached the bottom of the specimen in this case.

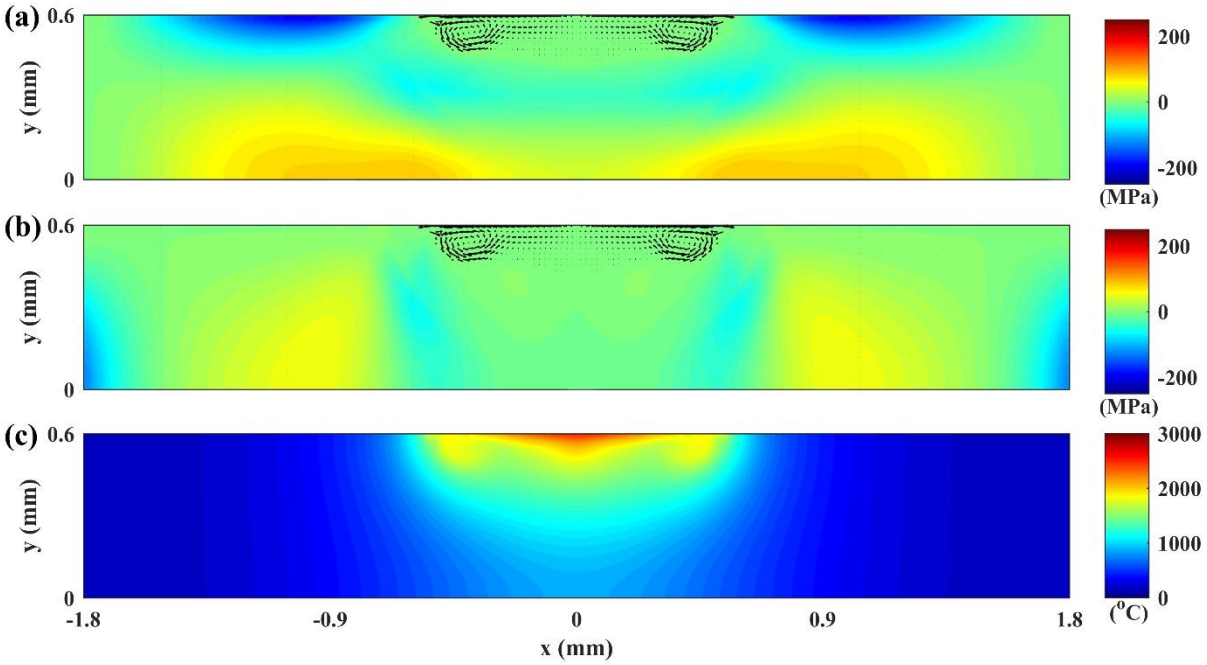

Figure 60. Stress and temperature fields right after the laser heating (laser pulse) is finished. A laser heating time of 0.05 s was used. (a) Normal stress in the x-direction, (b) Normal stress in the y-direction, (c) Temperature

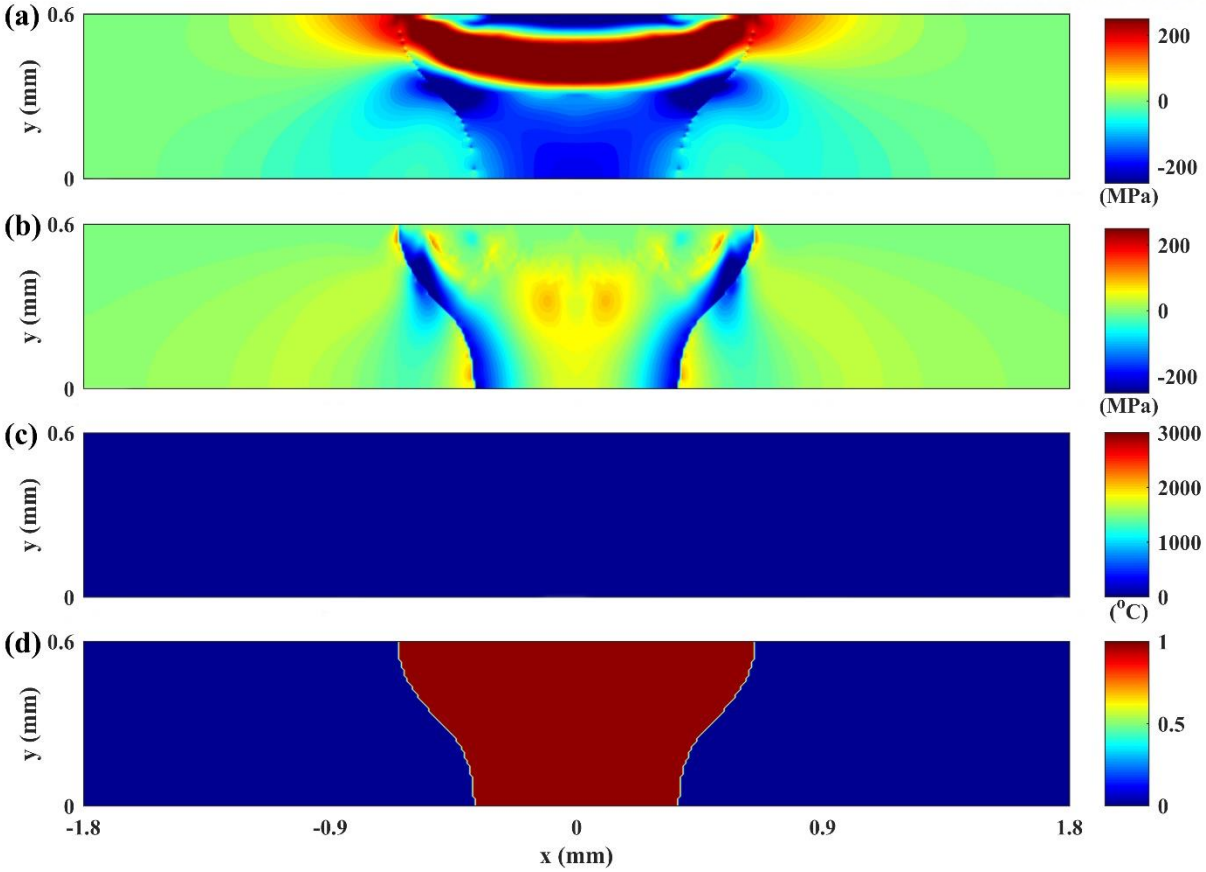

Figure 61. Stress, temperature, and martensite distributions after the material has been completely cooled down to the ambient temperature. A laser heating time of 0.05 s was used. (a) Normal stress in the x-direction, (b) Normal stress in the y-direction, (c) Temperature, (d) Martensitic phase distribution (represented as a red-colored region)

4.3.3. Effect of mushy zone size on residual stress development

As explained before, this method is capable of dealing with mushy zones, together with solid and liquid phases, as a single continuum. To investigate the influence of the mushy zone size on residual stress development, we artificially varied the mushy zone size by using different liquidus temperatures of 1460°C and 1550°C. As shown in Table 3, the actual liquidus temperature is 1500°C, but by using a smaller or larger liquidus temperature value, we can artificially generate a narrower or wider mushy zone, respectively. (The solidus temperature is kept at 1450°C.) Figure 62 presents fluid volume fraction distributions at 0.055 s (during the cooling period) obtained with three liquidus temperatures, 1460, 1500 and 1550 °C. As expected, the mushy zone is widened as the liquidus temperature increases and the results are stable regardless of the mushy zone size. For the three cases, final residual stresses (both *x* and *y* normal stress components) along the vertical central line (x=0) are compared in Figure 63. Because the mushy zone is much softer than the solid, a larger strain is formed

in the mushy zone during melting and solidification. Consequently, the mushy zone size affects the residual stress distribution as shown in Figure 63.

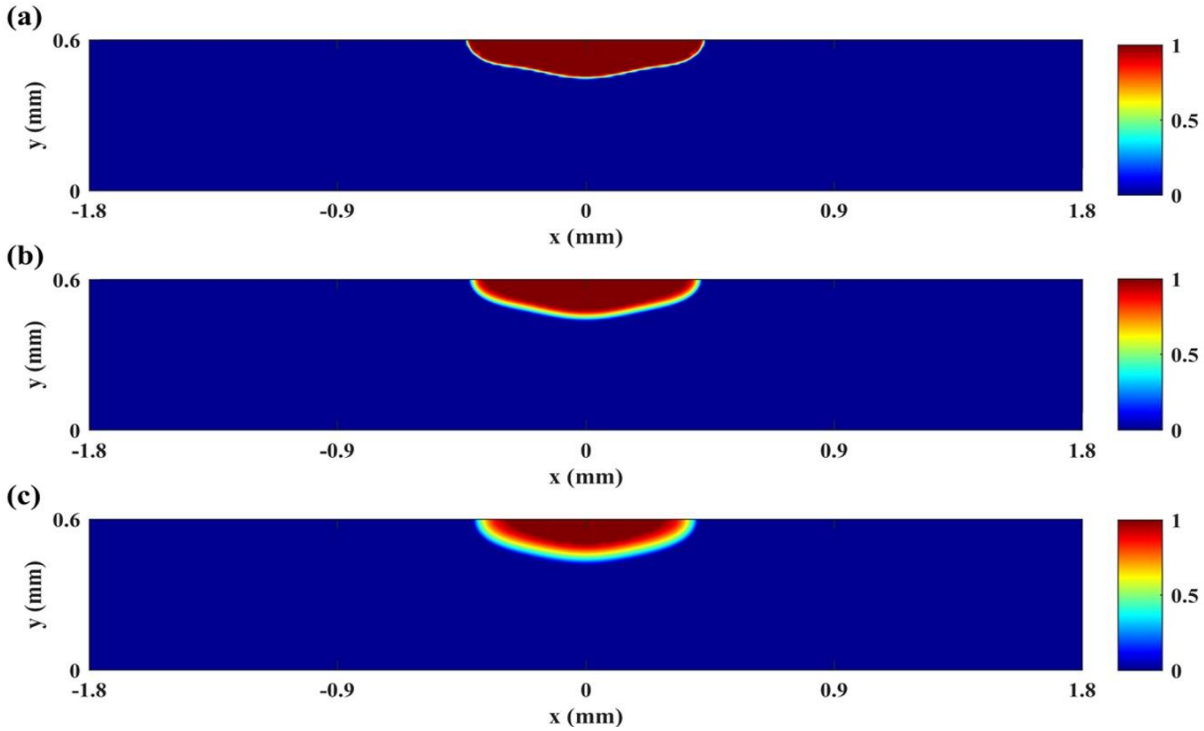

Figure 62. Fluid volume fraction distributions obtained with a liquidus temperature of (a) 1460 ºC, (b) 1500 ºC, (c) 1550 ºC

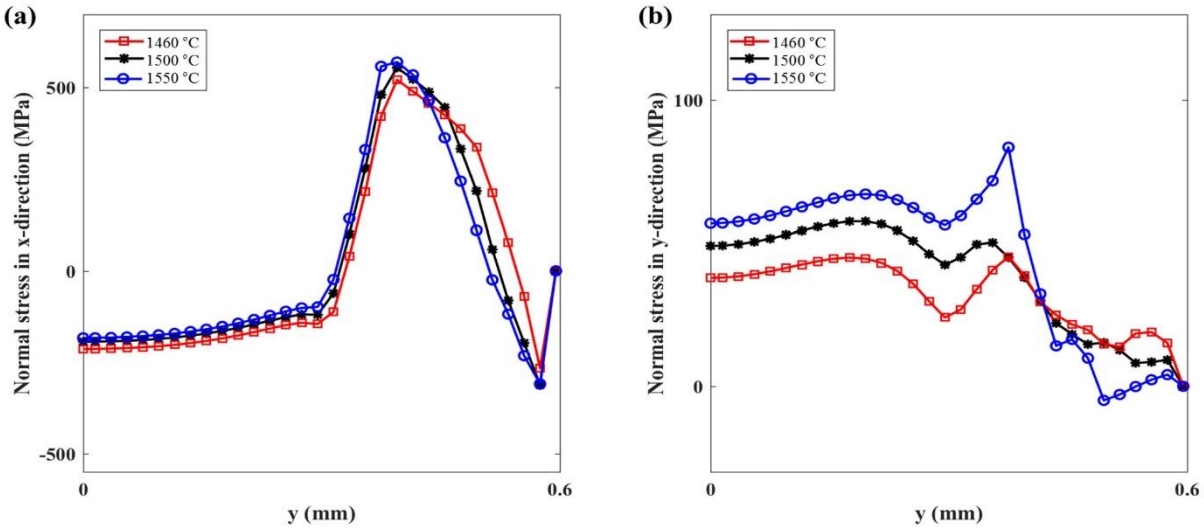

Figure 63. Final residual stress distributions along the vertical central line (x=0) obtained with liquidus temperatures of 1460, 1500 and 1550ºC. (a) Normal stress in the *x*-direction, (b) Normal stress in the *y*-direction

4.3.4. Validation of numerical algorithm

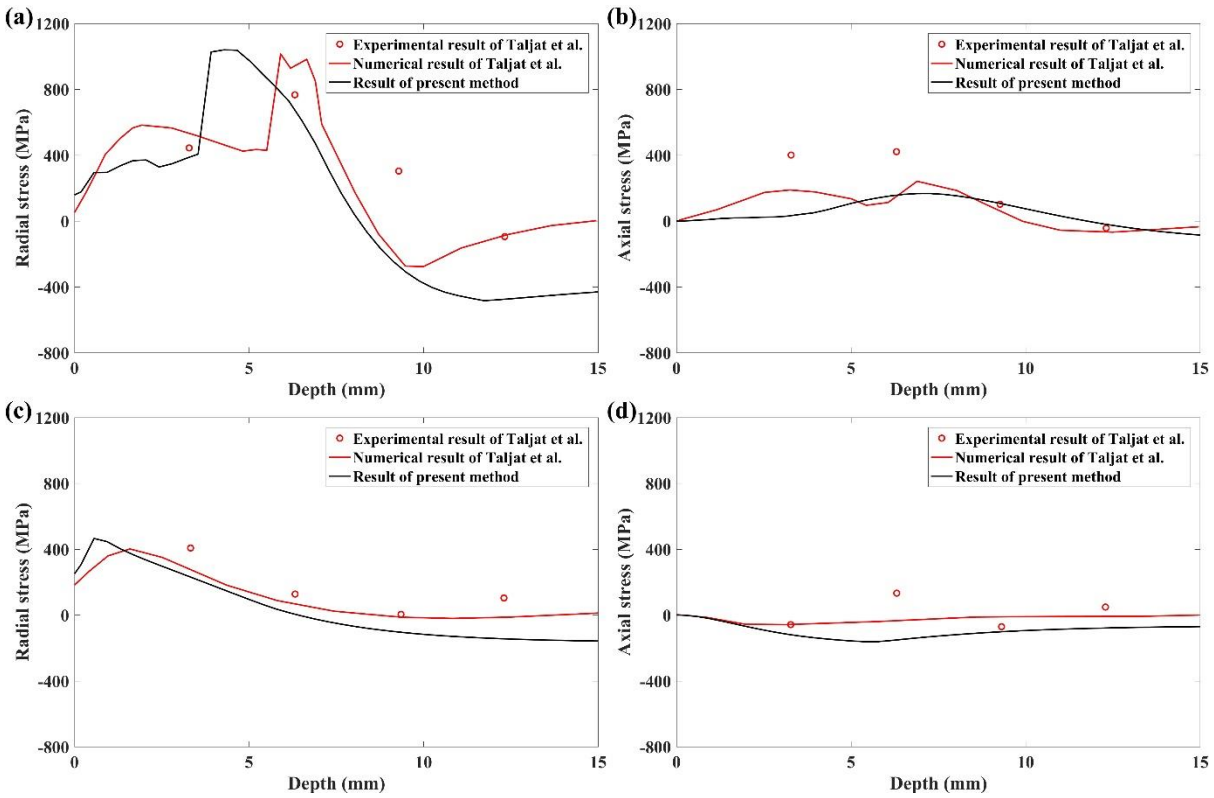

Figure 64. Comparison of axial and radial stresses using Taljat et al. [68]'s results. (a) Radial stress along the centerline, (b) Axial stress along the centerline, (c) Radial stress at a distance of 10 mm from the centerline, (d) Axial stress at a distance of 10 mm from the centerline.

We have validated our model by using Taljat et al.'s [68] work, where a HY-100 steel disk was heated by an autogenous gas tungsten arc welding process and the residual stress was investigated both numerically and experimentally. They used a finite element method, and a cylindrical coordinate system was employed.

We solved the same problem using the present method, and the details, such as material properties and problem description, can be found in [68]. Figure 64 shows the residual stresses in the radial and axial directions. Here, the black solid lines represent the results obtained by the present method, and the red solid lines and the red circles denote the numerical and experimental results of Taljat et al. [68], respectively. In Figure 64. (a) and (b), the radial and axial residual stresses are plotted along the center of the disk in the depth direction, starting from the top surface, and in Figure 64. (c) and (d), the residual stresses at a distance of 10 mm from the centerline are plotted in the depth direction. Overall, radial residual stresses are shown to be more prominent than axial stresses, especially at the centerline, and both components decrease in the depth direction. As shown, all three results are reasonably

similar, although it is hard to say which one is more accurate because even experimentally measured residual stresses are not necessarily accurate. However, we can say that residual stresses predicted by the presented numerical algorithm is physically realistic and at least qualitatively accurate.

4.4. Conclusions

A novel numerical method for computing thermal residual stresses was presented. In this method, a unified momentum equation that treats solid, liquid and mushy states as a single continuum was formulated from a standpoint of fluid–structure interaction. Because of this unique characteristic, this method is capable of calculating residual stresses as the material undergoes melting and solidification, and liquid and solid phases interact with each other during the phase change. This method was successfully tested with a laser heating problem, where a carbon steel sheet was heated by a Gaussian laser beam, and we believe that this method can be easily applied to many other similar problems.

5. Unified momentum equation approach for laser heat treatment

This chapter includes following contents:

H. Yeo, M. Son, S. Oh, H. Ki*, (2020), in preparation.

In this chapter, the unified momentum equation approach is improved to predict residual stresses caused by actual laser heat treatment. A three-dimensional numerical model is used, and the laser heat treatment experiment is performed to verify the numerical results.

5.1. Experimental procedure

A 50×30×8 mm^3 AH36 carbon steel is used for laser heat treatment experiment and the chemical composition of the material is shown in Table 5.

Table 5. Chemical composition of AH36 (wt.%)

C	Si	Mn	P	S	Cr	Ni	Cu	Nb	Ti	V	Al
0.157	0.392	1.501	0.014	0.003	0.030	0.010	0.015	0.002	0.003	0.003	0.042

The heat source is a 2 kW fiber laser with 4.4 mm × 3.7 mm rectangular top-hat profile (IPG YLS-2000). The wavelength is 1070 nm and the focal length is 250 mm. Figure 65 shows the schematic drawing of the laser heat treatment experiment where the laser beam scans the center of the specimen by 30 mm with a constant speed. Experiments are carried out on a total of three process conditions which are presented in Table 6.

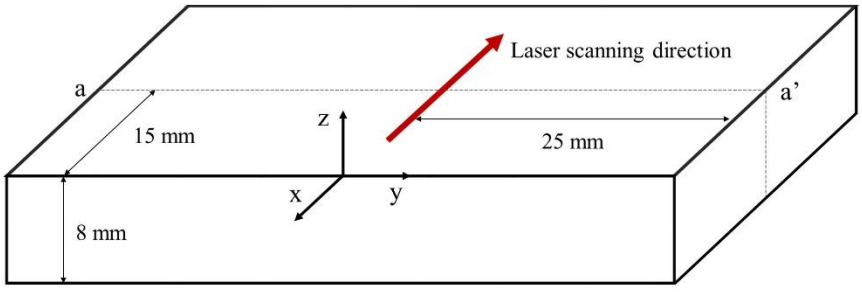

Figure 65. Schematic drawing of laser heat treatment experiment

Table 6. Process conditions of laser heat treatment experiment

Case	**Laser power (*P*)**	**Scanning speed (U_s)**
A	1850 W	5 mm/s
B	650 W	2 mm/s
C	600 W	0.2 mm/s

The residual stress distribution induced by laser heat treatment is measured using the contour method [69]. Using this method, a full two-dimensional map of residual stresses acting in a normal direction to the cross section can be obtained [70]. The specimens are cut into two parts by the wire electric discharge machining (WEDM) along the line a-a' shown in Figure 65. Then, the cutting surfaces are deformed due to the relaxation of residual stresses. Using the deformation data of cutting surfaces, the distribution of residual stresses is calculated by the finite element analysis. The microstructures on the cutting surfaces such as austenite, martensite, and bainite are investigated by using the optical microscopy. The specimens are polished with diamond powder and etched with 10% of Nital solution.

5.2. Mathematical model

In this section, the mathematical models for mechanical, thermal, and metallurgical analysis are presented. Numerical models are derived using the actual laser experimental conditions and properties of AH36 carbon steel.

5.2.1. Mechanical analysis

The total strain tensor of structures is defined as

$$\boldsymbol{\varepsilon}_{tot} = \boldsymbol{\varepsilon}_e + \boldsymbol{\varepsilon}_t + \boldsymbol{\varepsilon}_p + \boldsymbol{\varepsilon}_v + \boldsymbol{\varepsilon}_{trip} = \frac{1}{2}\left(\nabla \mathbf{d} + \nabla \mathbf{d}^T\right) \tag{76}$$

where $\boldsymbol{\varepsilon}_e$, $\boldsymbol{\varepsilon}_t$, $\boldsymbol{\varepsilon}_p$, $\boldsymbol{\varepsilon}_v$, and $\boldsymbol{\varepsilon}_{trip}$ are the elastic, thermal, plastic, phase transformation induced volumetric, and phase transformation induced plastic strain tensors. Here, the phase transformation induced plastic strain is added for accurate prediction of residual stresses. Each strain terms are calculated as follows:

- Thermal strain

In Eq. (44), the coefficient of thermal expansion is dependent on the phase and calculated by the linear mixture law.

$$\alpha = \sum_{i=1}^{n} \alpha_i f_i \tag{77}$$

Here, α_i and f_i are the coefficient of thermal expansion of phase i and the volume fraction of phase i. The coefficients of thermal expansion of AH36 are 1.495×10^{-5} /K for ferrite, 2.447×10^{-5} /K for austenite, 1.438×10^{-5} /K for bainite and pearlite, and 1.404×10^{-5} /K for martensite [71].

- Plastic strain

For the plastic strain, the von Mises yield criterion is used with kinematic hardening rule [65]

$$\mathrm{f} = \left\|\mathrm{dev}\left[\boldsymbol{\sigma}\right] - \boldsymbol{\beta}\right\| - \sqrt{\frac{2}{3}}\sigma_Y \tag{78}$$

where dev[$\boldsymbol{\sigma}$] is the stress deviator and $\boldsymbol{\beta}$ is the back stress. Then, to satisfy the yield criterion, the plastic strain is developed and calculated using the rate-independent plastic model. The evolution of the plastic strain and the back stress is represented by following equations [65]

$$\dot{\boldsymbol{\varepsilon}}_p = \gamma \frac{\mathrm{dev}\left[\boldsymbol{\sigma}\right] - \boldsymbol{\beta}}{\left\|\mathrm{dev}\left[\boldsymbol{\sigma}\right] - \boldsymbol{\beta}\right\|} \text{ and } \dot{\boldsymbol{\beta}} = \gamma \frac{2}{3} H' \frac{\mathrm{dev}\left[\boldsymbol{\sigma}\right] - \boldsymbol{\beta}}{\left\|\mathrm{dev}\left[\boldsymbol{\sigma}\right] - \boldsymbol{\beta}\right\|} \tag{79}$$

where γ is the plastic parameter and H' is the strain hardening parameter. The strain hardening parameter is calculated as 700 MPa using the yield strength, ultimate tensile stress, and elongation

values from Mill test results.

- Phase transformation induced volumetric strain

Due to the solid-state phase transformation during heating and cooling, the volumetric strain is caused and expressed as

$$\boldsymbol{\varepsilon}_v = \left(\varepsilon_{fa} f_a + \varepsilon_{af} f_f + \varepsilon_{ab} f_b + \varepsilon_{am} f_m\right)\mathbf{I} \tag{80}$$

where ε_{fa}, ε_{af}, ε_{ab}, and ε_{am} are the volume change due to the complete transformation of ferrite to austenite, austenite to ferrite, austenite to bainite, and austenite to martensite. In the literature [71], ε_{fa} and ε_{af} are dependent on the heating rate and the values of AH36 expressed as

$$\begin{aligned} \varepsilon_{fa} &= a \cdot AC1\left(HR\right) + b \\ \varepsilon_{af} &= a \cdot T_{ff}\left(HR\right) + b \end{aligned} \tag{81}$$

where a and b are linear fitting coefficients and T_{ff} is the finish temperature of the ferrite transformation. ε_{ab} and ε_{am} of AH36 are 5.57×10^{-3} and 8.21×10^{-3} [71].

- Phase transformation induced plastic strain

The solid-state phase transformation also leads to the phase transformation induced plastic strain which is described by the Greenwood-Johnson mechanism and the Magee mechanism [72]. In this work, the transformation induced plastic strain is computed by following equation.

$$\boldsymbol{\varepsilon}_{trip} = 3K(1-f_i)\Delta f_i \,\mathrm{dev}\left[\boldsymbol{\sigma}\right] + \boldsymbol{\varepsilon}^{o}_{trip} \tag{82}$$

Here, K is the material specific constant (4.18×10^{-5} MPa^{-1} for austenite to bainite transformation 5.08×10^{-5} MPa^{-1} for austenite to martensite transformation from [73]) and $\boldsymbol{\varepsilon}^{o}_{trip}$ is the phase transformation induced plastic strain from the previous time step.

Then, the coefficients and source term of unified momentum equation (Eq. (17)) is re-written as

$$\begin{aligned} \bar{\mu} &= \eta f_f + \mu \Delta t f_s \\ \bar{\lambda} &= \lambda \Delta t \, f_s \\ \bar{\mathbf{b}} &= -p\mathbf{I}\, f_f + \left\{\mu\left(\nabla \mathbf{d}^{o} + \nabla \mathbf{d}^{oT}\right) + \lambda\left(\nabla \cdot \mathbf{d}^{o}\right)\mathbf{I} - 2\mu(\boldsymbol{\varepsilon}_t + \boldsymbol{\varepsilon}_v + \boldsymbol{\varepsilon}_p + \boldsymbol{\varepsilon}_{trip}) - \left(\lambda \,\mathrm{Tr}(\boldsymbol{\varepsilon}_t + \boldsymbol{\varepsilon}_v + \boldsymbol{\varepsilon}_p + \boldsymbol{\varepsilon}_{trip})\right)\mathbf{I}\right\} f_s \end{aligned} \tag{83}$$

where η is 6×10^{-3} kg/m·s [74] and the temperature and microstructure dependent mechanical properties of AH36 are shown in Figure 66.

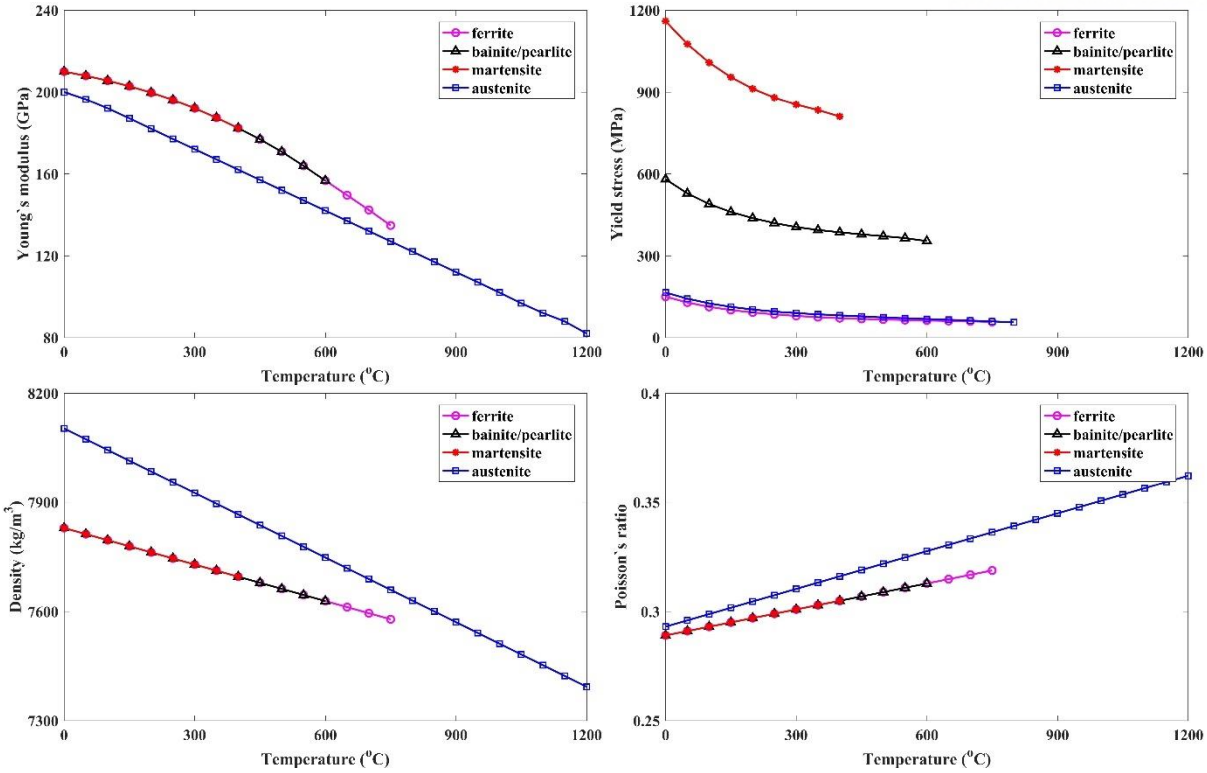

Figure 66. Temperature and microstructure dependent Young's modulus (E), yield stress (σ_Y), density (ρ), and Poisson's ratio (v) of AH36 (taken from [71])

The mechanical boundary conditions are as follows. As mentioned previously, the symmetry boundary condition is applied to the (x, 0, z) plane in Figure 65. If melting occurs, the thermocapillary force is applied to the melt pool surface.

$$\boldsymbol{\sigma}_f \cdot \mathbf{n} = \nabla_s T \frac{d\gamma}{dT} \tag{84}$$

Here, the surface tension gradient is -3×10^{-4} N/m·K [75]. For the other surfaces, following traction free boundary condition is applied.

$$\boldsymbol{\sigma} \cdot \mathbf{n} = 0 \tag{85}$$

5.2.2. Thermal analysis

The same numerical method presented in Chapter 4 is used. In Eq. (53), the thermal conductivity (k) is 37 J/m·K for solids and 26 J/m·K for liquids [74]. In Eq. (54), specific heats for solid and liquid, specific latent heat, solidus temperature, and liquidus temperature are 470 J/kg·K, 697 J/kg·K, 247 kJ/kg, 1415 ºC, and 1518 ºC, respectively [74].

The thermal boundary conditions are as follows. The symmetry boundary condition is applied to the (x, 0, z) plane in Figure 65 and right half part is considered in the numerical analysis. At the top

surface, the moving laser heat source and heat loss due to the convection and radiation are considered.

$$k\frac{\partial T}{\partial n} = q_{\text{laser}} - h\left(T - T_0\right) - \varepsilon\sigma\left(T^4 - T_0^4\right) \tag{86}$$

Here, $\partial T/\partial n$ is temperature gradient along the surface normal direction, convection heat transfer coefficient is 50 W/m^2·K, emissivity is 0.79 [76], and ambient temperature is 20°C. The moving laser heat source with rectangular top-hat profile is written as

$$q_{\text{laser}} = \begin{cases} \dfrac{\eta_a P}{L_x L_y} & \text{for } -\dfrac{L_x}{2} \le x - U_s t \le \dfrac{L_x}{2}, \text{ and } -\dfrac{L_y}{2} \le y \le \dfrac{L_y}{2} \\ 0 & \text{for others} \end{cases} \tag{87}$$

where η_a, L_x, and L_y are absorption coefficient, and laser beam dimensions in x (3.7 mm) and y (4.4 mm) directions. For the other lateral surfaces, the convection boundary condition is employed.

$$k\frac{\partial T}{\partial n} = -h\left(T - T_0\right) \tag{88}$$

5.2.3. Metallurgical analysis

The solid-state phase transformation plays an important role in the residual stresses. According to the phases, the thermal and mechanical properties are changed, and phase transformation induced volumetric and plastic strains are also caused. The initial microstructure of the AH36 steel used in the experiment is 30% ferrite and 70% pearlite which are determined by using the yield strength values of each phase and Mill test results [71]. During the heating process, the ferrite and pearlite phases are transformed to the austenite between the AC1 and AC3 temperatures, and the austenite fraction is calculated as

$$f_a = \frac{T - AC1}{AC3 - AC1} \tag{89}$$

The $AC1$ and $AC3$ temperatures depend on the heating rate and expressed as the fitted power functions using experimental data [74].

$$\begin{aligned} AC1 &= a\left(HR_{\max}\right)^b + c \\ AC3 &= d\left(HR_{\max}\right)^e + AC1 \end{aligned} \tag{90}$$

Here, a, b, c, d, and e are constants of the fitted power function, and $HR_{\max}$ is the maximum heating rate. After the heating process, the material undergoes a cooling and austenite transformed to martensite, bainite, or pearlite according to the cooling rate. The phase transformation in the cooling cycle including the maximum phase fraction and transformation start temperature is determined by using the continuous cooling transformation (CCT) diagram shown in Figure 4. The cooling rate is

calculated as

$$-\frac{875\,^{o}\mathrm{C}-T}{t_{@875\,^{o}\mathrm{C}}-t} \tag{91}$$

where 875 °C is the reference temperature in CCT diagram and $t_{@875\,^{o}\mathrm{C}}$ is the time at reference temperature. For fast cooling rate, austenite transforms to martensite, and martensite fraction is calculated by following the Koistinen-Marburger equation [64]

$$f_m = f_{a0}\left[1-\exp\left\{-0.011\left(T_{ms}-T\right)\right\}\right] \tag{92}$$

where f_{a0} is the austenite fraction when the transformation begins and T_{ms} is the start temperature of the martensite transformation.

The overall numerical procedure is the same as in Figure 49. This unified momentum equation approach has following advantages.

- The stress development during the thermal process is calculated from a viewpoint of fluid-structure interaction (FSI). The effects of fluid flow on temperature, solid-state phase, and stress development can be accurately taken into account.
- Thermal, metallurgical, and mechanical models are fully coupled in this method where temperature, solid-state phase, and stress fields are computed at the same time and interact each other.

5.3. Numerical and experimental results

In this section, the experimental and numerical results of the laser heat treatment process are presented and compared with each other. The residual stress, temperature, and solid-state phase are intensively analyzed. Using the presented numerical model, simulations are performed for same process conditions as laser heat treatment experiment shown in Table 6.

The numerical results of Case A are demonstrated in Figure 67~Figure 70 where two simulation results are plotted in one figure (left half: numerical results considering fluid flow, right half: numerical results without considering fluid flow). To examine the influences of the fluid flow caused from melting, large heat input is applied in Case A. Traditionally, in order to account for the effects of fluid flow on temperature or stress development, previous studies of predicting residual stresses used following methods instead of considering fluid flow directly. Thermal conductivity was artificially increased [60], molten element was excluded from the stress analysis [77], or an assumption that a material tends to behave more like a solid or liquid based on the mechanical coherence point was introduced [78].

Figure 67 and Figure 68 show the top view of stress, solid-state phase, and temperature distributions for Case A during the laser process and after the material has been completely cooled down to the ambient temperature. The black arrows indicate the fluid flow in the melt pool. In the laser heating zone, the carbon steel softens and melts due to high temperatures, resulting in very low stress levels. Compressive stresses are developed near the heating zone to resist the expansion by heating. To maintain the force balance, tensile stresses are formed on the sides. During this heating process, initial phase is transformed to austenite phase. In the temperature field, much higher temperatures are observed in the numerical result without fluid flow, since convection due to the fluid flow does not occur. After the laser heating is finished, the material is cooled down and the austenite is transformed to martensite because the cooling rate of Case A is very fast. The formation of martensitic phase alleviates the volume shrinkage due to the cooling and generate the compressive stress.

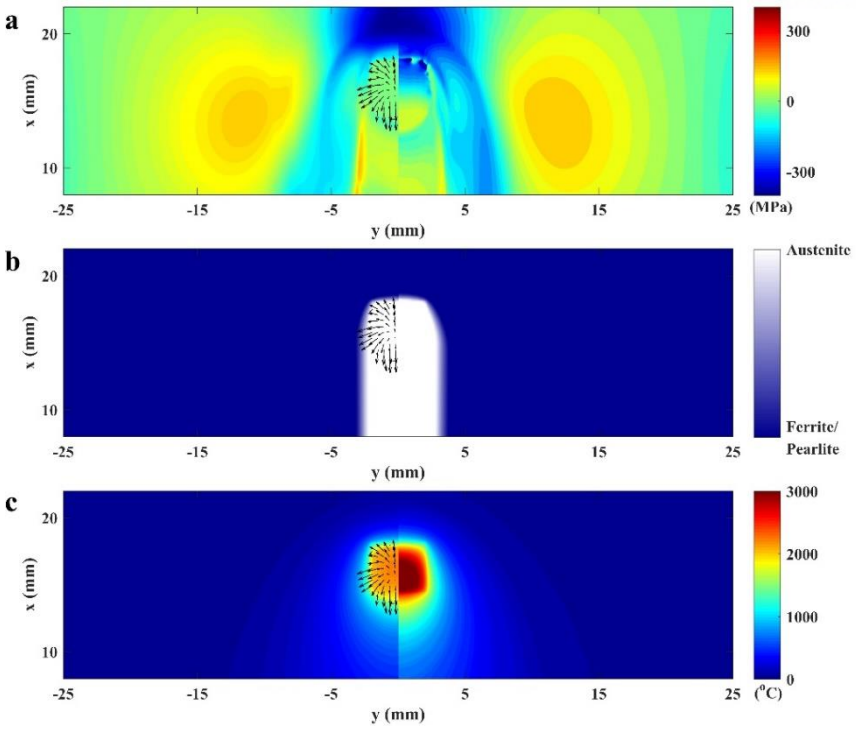

Figure 67. Numerical results considering fluid flow (left) and without considering fluid flow (right) for Case A at the top surface during the laser process. (a) Normal stress in the x-direction, (b) Solid-state phase, (c) Temperature.

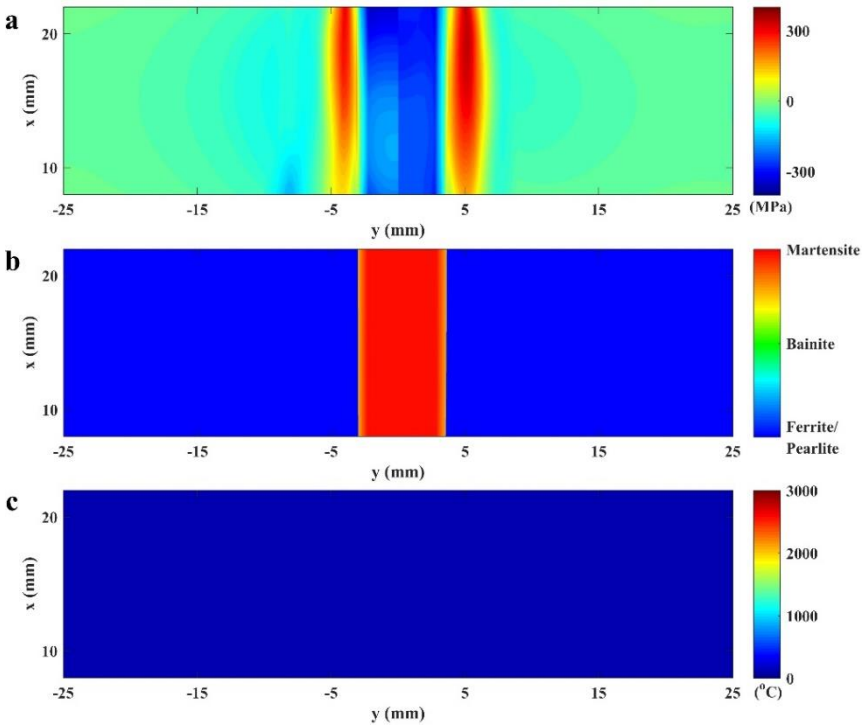

Figure 68. Numerical results considering fluid flow (left) and without considering fluid flow (right) for Case A at the top surface after the material has been completely cooled down to the ambient temperature. (a) Normal stress in the x-direction, (b) Solid-state phase, (c) Temperature.

In Figure 69 and Figure 70, the cross-section view of stress, solid-state phase, and temperature distributions for Case A is presented. The temperature distribution is further enlarged to closely observe the fluid flow in the melt pool. The figures in the cross-section show more clearly the differences between the numerical results with and without fluid flow. In the results considering fluid flow, the shape of HAZ is long in the horizontal direction due to melt flow driven by thermocapillary force. On the other hand, if the fluid flow is not taken into account, the shape of HAZ becomes circular and deep. Changes in temperature distribution affect the solid-state phase transformation and eventually alters residual stress distribution. In addition, the fluid-structure interactions in the mushy zone during melting and solidification influences stress development.

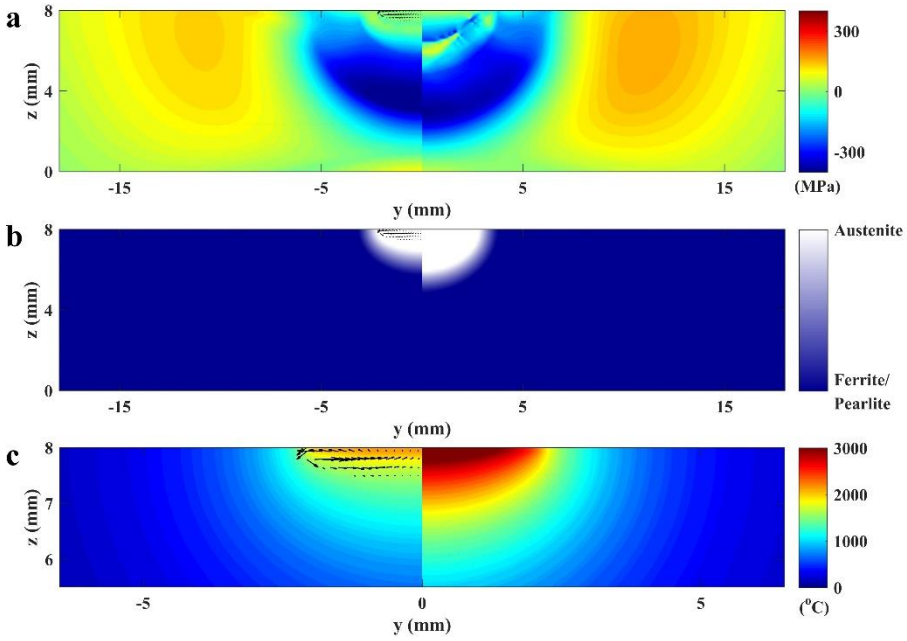

Figure 69. Numerical results considering fluid flow (left) and without considering fluid flow (right) for Case A at the cross-section during the laser process. (a) Normal stress in the x-direction, (b) Solid-state phase, (c) Temperature.

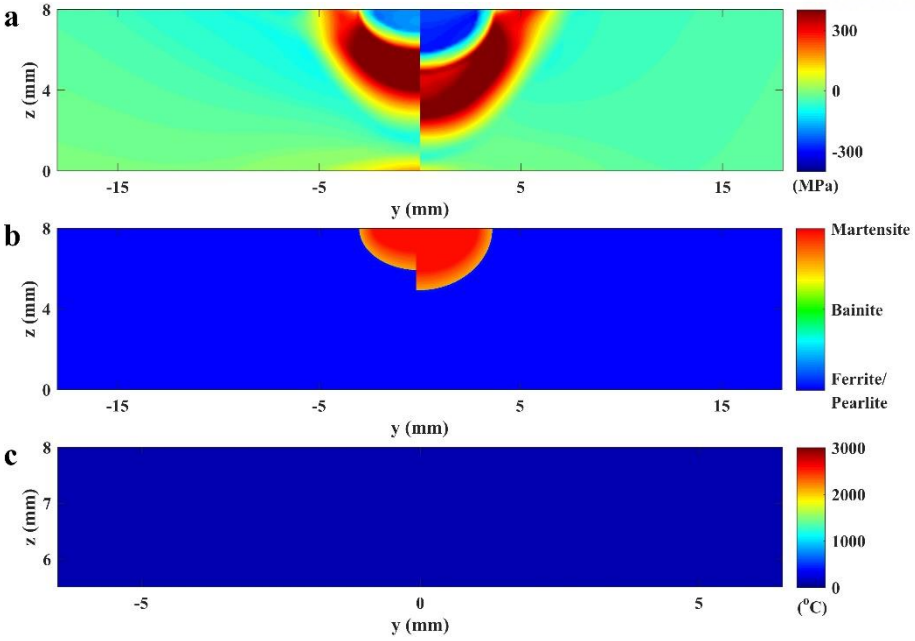

Figure 70. Numerical results considering fluid flow (left) and without considering fluid flow (right) for Case A at the cross-section after the material has been completely cooled down to the ambient temperature. (a) Normal stress in the x-direction, (b) Solid-state phase, (c) Temperature.

In Figure 71, the solid-state phase distribution of numerical results for Case A is compared with the experimental measurements by optical microscopy at the cross-section. In the numerical result, martensite, bainite, and ferrite/pearlite (initial phase) phases are represented as red, green, and blue colors. Two black solid lines indicate solidus temperature and A1 temperature where the solid-state transformation begins. At the bottom of the figure, high magnification optical micrographs are presented to observed solid-state phases. In Case A, only the austenite to martensite transformation occurs after laser irradiation is finished due to the rapid cooling rate. At the position a, the martensite is well observed. As it goes down, the size of the martensitic phase becomes smaller and the ferrite/pearlite phase fraction increases while the martensite phase fraction decreases as shown at the position b. At the position c, no solid-state phase transformation occurs and only the initial phase exists. Figure 72 shows residual stresses (normal stress in the x-direction) of numerical results and experimental measurements for Case A. The black solid and dotted lines present the numerical results with and without fluid flow. The red solid line is the experimental result. The residual stresses are compared along the z-direction at the centerline and along the y-direction at a distance of 2.4 mm from the top surface. The numerical result without considering fluid flow do not fit well with the experimental measurement since the size of HAZ is deeper than actual result.

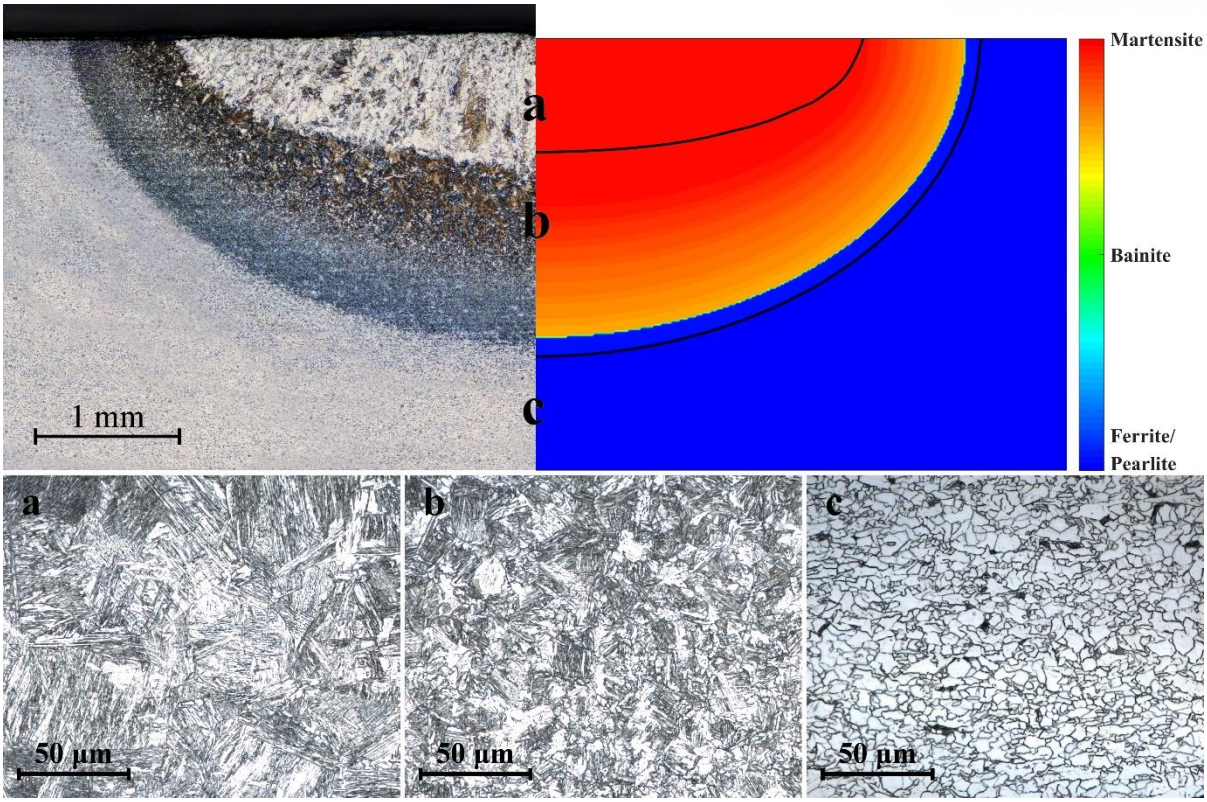

Figure 71. Optical micrograph of cross-section (left) and simulation result of solid-state phase (right) for Case A. High magnification optical micrographs at positions a, b, and c are at the bottom of the figure.

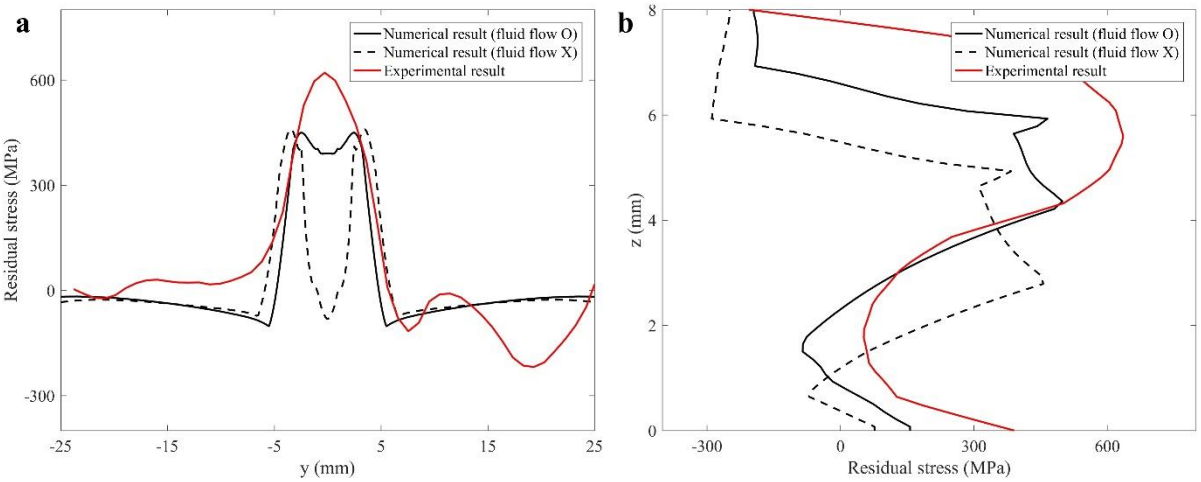

Figure 72. Comparison of residual stresses obtained by numerical simulation and experimental measurement at cross-section for Case A. (a) along the z-direction at the centerline, (b) along the y-direction at a distance of 2.4 mm from the top surface.

Optical micrograph and solid-state phase distribution obtained by numerical simulation for Case B are shown in Figure 73. In this case, the applied laser intensity is lower, and the scanning speed is slower than Case A. The big difference from Case A is the smaller size of HAZ but the cooling rate is still fast and only the austenite to martensite transformation is observed. Similar to Case A, as it goes down, the size of the martensitic phase becomes smaller and martensite phase fraction decreases. Figure 74 shows residual stress distributions of numerical and experimental results for Case B. Because of the different sizes of HAZ, the two turning points (z=5.7 mm, 2.2 mm) shown in Figure 74. (b) are located above than in Case A (z=5.6 mm, 1.8 mm). Also, the maximum magnitude of residual stress in Case B is smaller than in Case A.

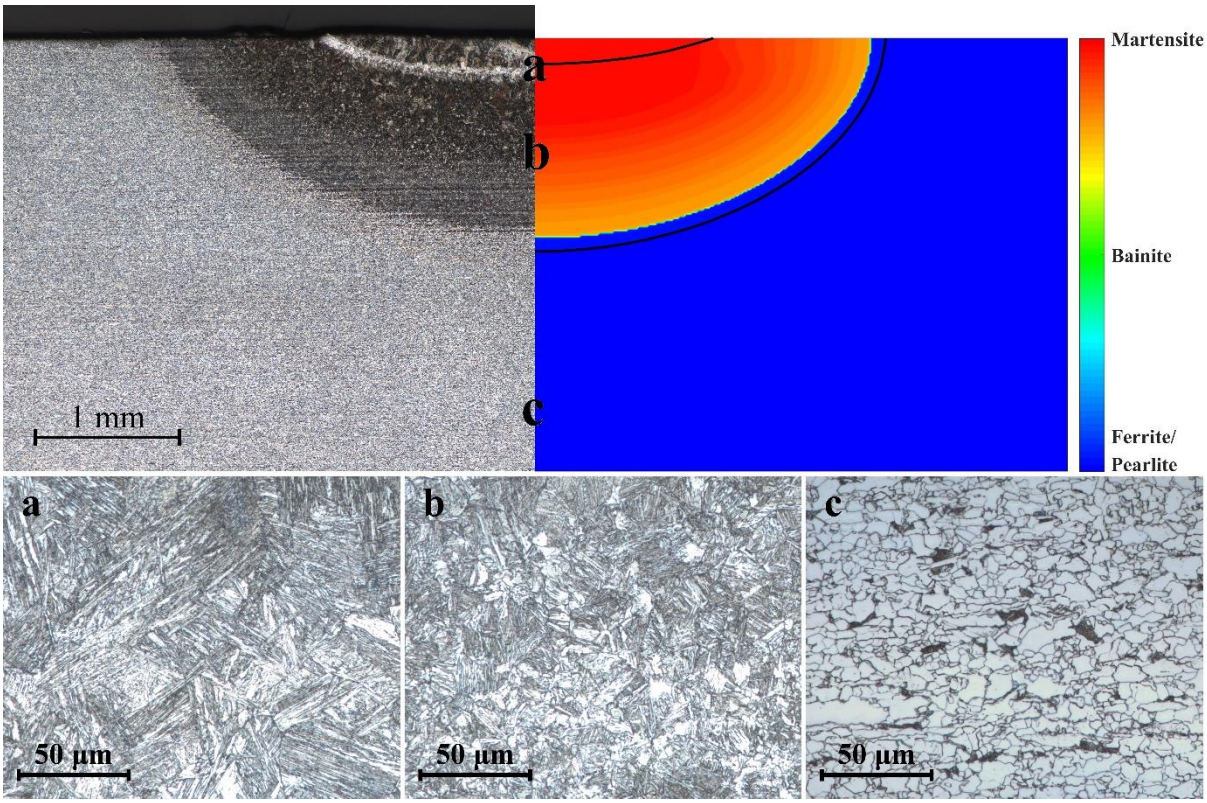

Figure 73. Optical micrograph of cross-section (left) and simulation result of solid-state phase (right) for Case B. High magnification optical micrographs at positions a, b, and c are at the bottom of the figure.

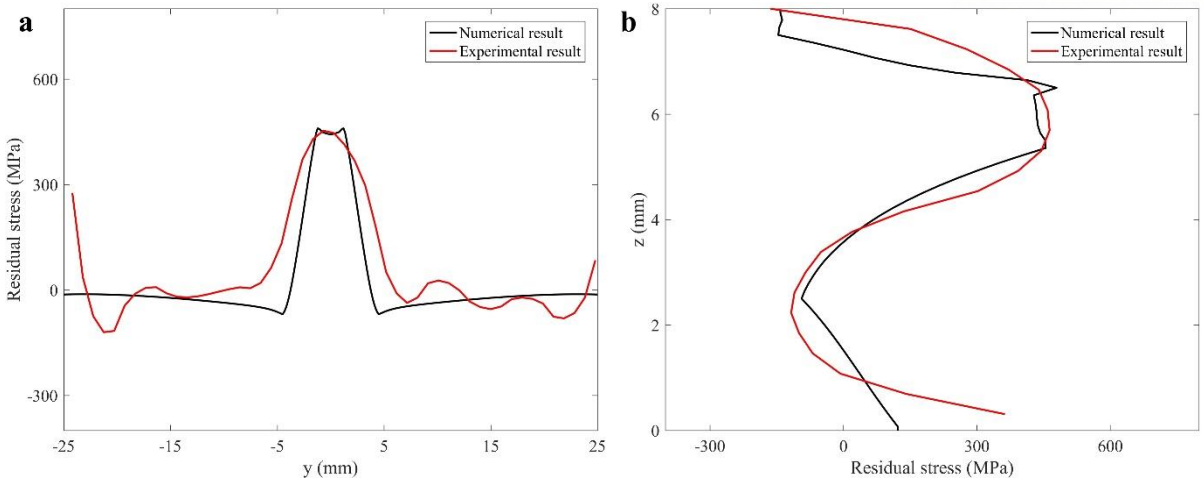

Figure 74. Comparison of residual stresses obtained by numerical simulation and experimental measurement at cross-section for Case B. (a) along the z-direction at the centerline, (b) along the y-direction at a distance of 2.4 mm from the top surface.

Figure 75 shows the optical micrograph and the numerical result of solid-state phase distribution for Case C. The laser scanning speed of Case C is very slow compared to previous cases and it takes a long time for the material to cool down. Consequently, in this case, the austenite to bainite transformation also takes place and the martensite and bainite coexist in the HAZ. In the numerical result, the martensite and bainite fractions are 31 % and 69 % at the point of surface center. In Figure 76, the residual stresses for Case C obtained by experiment and numerical simulation are compared. The overall trend of the residual stress distribution is similar to the previous cases, but low stress level is observed.

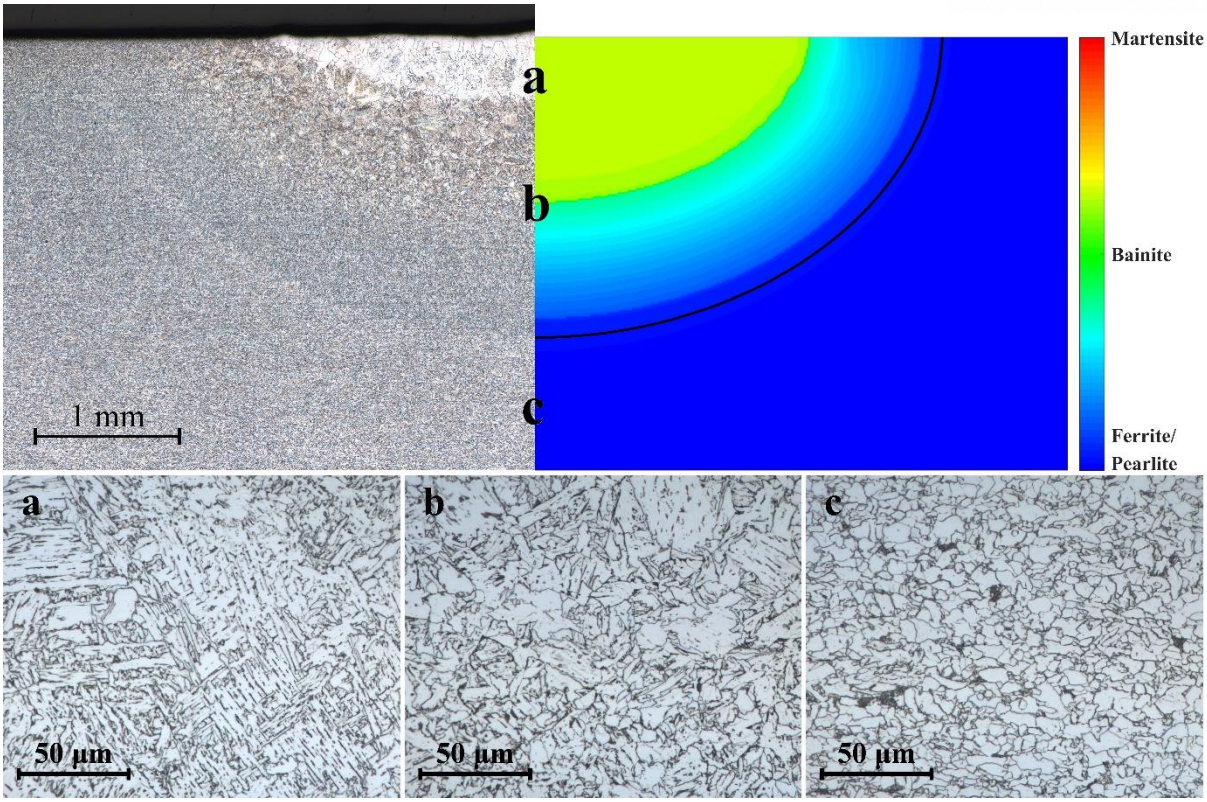

Figure 75. Optical micrograph of cross-section (left) and simulation result of solid-state phase (right) for Case C. High magnification optical micrographs at positions a, b, and c are at the bottom of the figure.

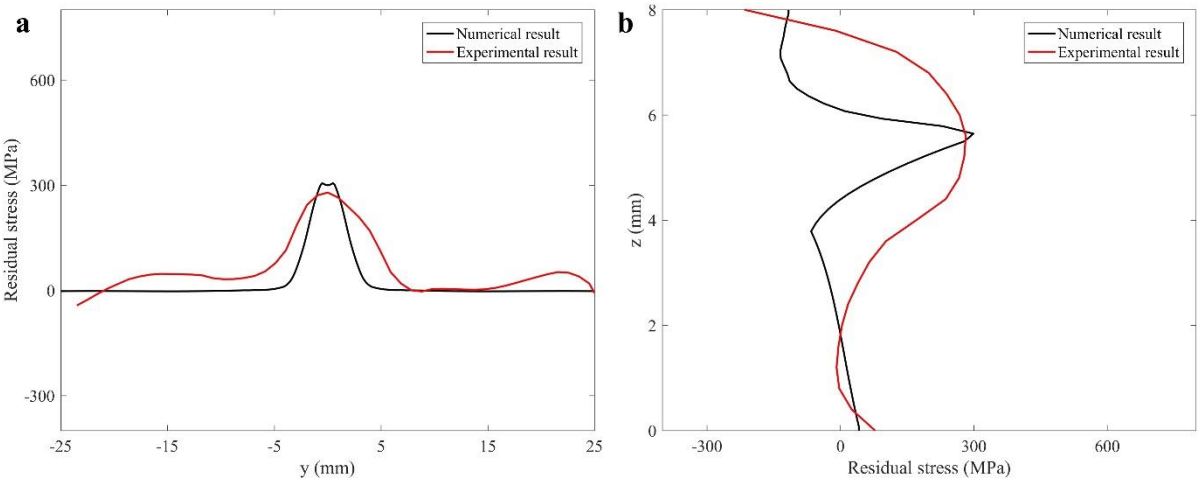

Figure 76. Comparison of residual stresses obtained by numerical simulation and experimental measurement at cross-section for Case C. (a) along the z-direction at the centerline, (b) along the y-direction at a distance of 2.4 mm from the top surface.

5.4. Conclusions

In this study, the 3-D numerical model was presented to accurately predict residual stresses of the laser heat treatment process. The evolution of microstructures and residual stresses during the laser heat treatment process was investigated numerically and experimentally. In the present work, thermal, metallurgical, and mechanical models were strongly coupled, and interactions between solid, liquid, and mushy state caused from melting and solidification were also included. The numerical model tested on three process conditions to examine the various residual stress distributions and solid-state phase transformations. The good agreement was found between numerical results and experimental results.

6. Summary and future works

In this paper, we present a novel monolithic numerical model for FSI problems. The unified momentum equation is derived to treat fluid, structure, and mixture of fluid and structure as a single continuum. The unified momentum equation is a velocity-based formulation and discretized in a finite volume framework to accurately account for the momentum change around a computational cell. The governing equations can be solved by a proper numerical method for computational fluid dynamics and SIMPLE algorithm is used in this study. This numerical approach is first applied to stationary interface FSI problems and then to moving interface FSI problems by employing the level set method combined with a displacement field extension procedure. The moving interface is described in a fully Eulerian way to avoid the difficulties caused by grid handling. Various FSI problems are considered and the proposed FSI numerical model is successfully verified by solving validation problems in the literatures. The unified momentum equation is further improved and applied to computing thermal residual stresses. Due to the characteristics of unified momentum equation, the interactions of solid and liquid during melting and solidification are effectively considered in the residual stress development. This numerical method is successfully applied to two-dimensional laser melting problem of carbon steel. Lastly, the unified momentum equation approach is extended to three-dimensions and the laser heat treatment process of AH36 carbon steel is considered. Using the unified momentum equation approach, tight coupling of thermal, metallurgical, and mechanical models is obtained. The laser heat treatment experiments are also performed to validate the numerical method. The numerical results agree well with the experimental results.

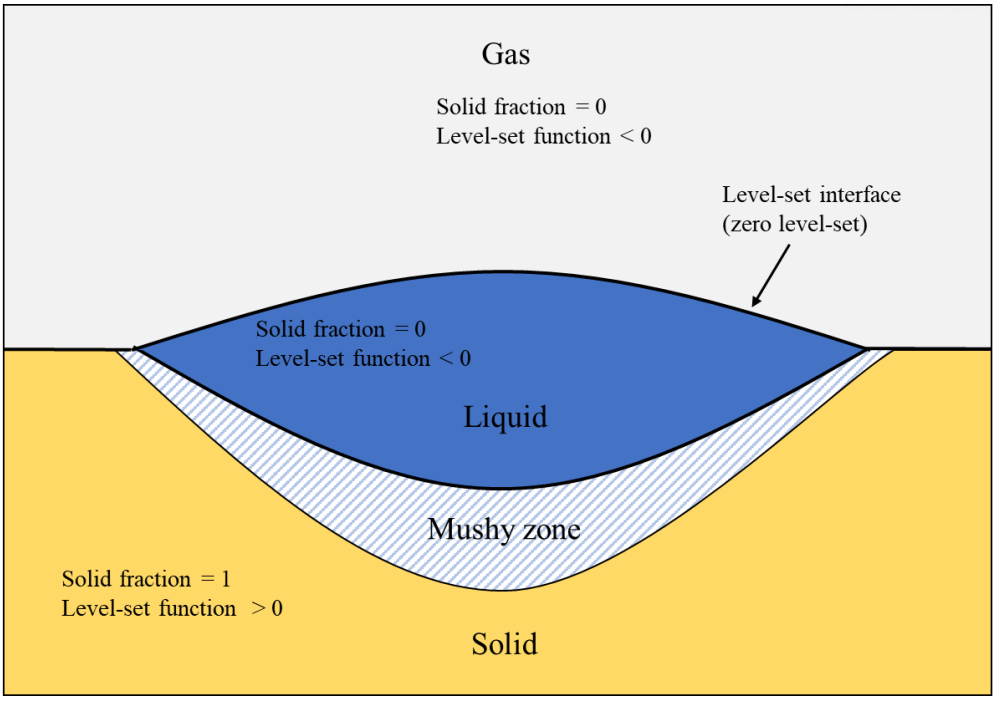

Figure 77. Schematic drawing of computational domain

We believe that the unified momentum equation approach can be easily applied to other laser processing such as laser cladding and laser welding. In these laser processing, the fluid-structure interactions take place actively and the proposed numerical method can be effectively employed. In order to simulate these laser processing, some improvements of numerical model are required. Now the boundary of processing material is moving, and it is necessary to adopt a suitable numerical method such as the level set method to describe the solid-gas or liquid-gas interface. The schematic drawing of computational domain is shown in Figure 77 where the gas phase is now included in the computational domain. In the liquid-gas interface, the interfacial forces such as capillary force and thermocapillary force act and accurate implementation of theses interfacial forces are significant. In addition, to accurately simulate laser welding process, the numerical models for multiple deflections, evaporation, and recoil pressure are required.

REFERENCES

[1] H. Ki, S. So, Process map for laser heat treatment of carbon steels, Optics & Laser Technology, 44 (2012) 2106-2114.

[2] H. Ki, S. So, S. Kim, Laser transformation hardening of carbon steel sheets using a heat sink, Journal of Materials Processing Technology, 214 (2014) 2693-2705.

[3] G.P. Dinda, A.K. Dasgupta, J. Mazumder, Laser aided direct metal deposition of Inconel 625 superalloy: Microstructural evolution and thermal stability, Materials Science and Engineering: A, 509 (2009) 98-104.

[4] K. Shah, I.u. Haq, A. Khan, S.A. Shah, M. Khan, A.J. Pinkerton, Parametric study of development of Inconel-steel functionally graded materials by laser direct metal deposition, Materials & Design (1980-2015), 54 (2014) 531-538.

[5] J. Kim, S. Oh, M. Son, H. Ki, A study of keyhole behavior and weldability in zero-gap laser welding of zinc-coated steel sheets at subatmospheric pressures, Journal of Materials Processing Technology, 249 (2017) 135-148.

[6] N. Farabi, D.L. Chen, J. Li, Y. Zhou, S.J. Dong, Microstructure and mechanical properties of laser welded DP600 steel joints, Materials Science and Engineering: A, 527 (2010) 1215-1222.

[7] Y. Bazilevs, M.C. Hsu, Y. Zhang, W. Wang, X. Liang, T. Kvamsdal, R. Brekken, J.G. Isaksen, A fully-coupled fluid-structure interaction simulation of cerebral aneurysms, Computational Mechanics, 46 (2009) 3-16.

[8] D. Kamensky, M.C. Hsu, D. Schillinger, J.A. Evans, A. Aggarwal, Y. Bazilevs, M.S. Sacks, T.J. Hughes, An immersogeometric variational framework for fluid-structure interaction: application to bioprosthetic heart valves, Comput Methods Appl Mech Eng, 284 (2015) 1005-1053.

[9] M.-C. Hsu, I. Akkerman, Y. Bazilevs, Finite element simulation of wind turbine aerodynamics: validation study using NREL Phase VI experiment, Wind Energy, 17 (2014) 461-481.

[10] K.-J. Paik, P.M. Carrica, D. Lee, K. Maki, Strongly coupled fluid–structure interaction method for structural loads on surface ships, Ocean Engineering, 36 (2009) 1346-1357.

[11] G. Hou, J. Wang, A. Layton, Numerical Methods for Fluid-Structure Interaction — A Review, Communications in Computational Physics, 12 (2015) 337-377.

[12] C. Farhat, K.G. van der Zee, P. Geuzaine, Provably second-order time-accurate loosely-coupled solution algorithms for transient nonlinear computational aeroelasticity, Computer Methods in Applied Mechanics and Engineering, 195 (2006) 1973-2001.

[13] P. Causin, J.F. Gerbeau, F. Nobile, Added-mass effect in the design of partitioned algorithms for fluid–structure problems, Computer Methods in Applied Mechanics and Engineering, 194 (2005) 4506-4527.

[14] H.G. Matthies, R. Niekamp, J. Steindorf, Algorithms for strong coupling procedures, Computer

Methods in Applied Mechanics and Engineering, 195 (2006) 2028-2049.

[15] B. Hübner, E. Walhorn, D. Dinkler, A monolithic approach to fluid–structure interaction using space–time finite elements, Computer Methods in Applied Mechanics and Engineering, 193 (2004) 2087-2104.

[16] M. Heil, An efficient solver for the fully coupled solution of large-displacement fluid–structure interaction problems, Computer Methods in Applied Mechanics and Engineering, 193 (2004) 1-23.

[17] P.B. Ryzhakov, R. Rossi, S.R. Idelsohn, E. Oñate, A monolithic Lagrangian approach for fluid–structure interaction problems, Computational Mechanics, 46 (2010) 883-899.

[18] A. Franci, E. Oñate, J.M. Carbonell, Unified Lagrangian formulation for solid and fluid mechanics and FSI problems, Computer Methods in Applied Mechanics and Engineering, 298 (2016) 520-547.

[19] K. Sugiyama, S. Ii, S. Takeuchi, S. Takagi, Y. Matsumoto, A full Eulerian finite difference approach for solving fluid–structure coupling problems, Journal of Computational Physics, 230 (2011) 596-627.

[20] P. Le Tallec, J. Mouro, Fluid structure interaction with large structural displacements, Computer Methods in Applied Mechanics and Engineering, 190 (2001) 3039-3067.

[21] E. Kuhl, S. Hulshoff, R. de Borst, An arbitrary Lagrangian Eulerian finite-element approach for fluid-structure interaction phenomena, International Journal for Numerical Methods in Engineering, 57 (2003) 117-142.

[22] M. Engel, M. Griebel, Flow simulation on moving boundary-fitted grids and application to fluid-structure interaction problems, International Journal for Numerical Methods in Fluids, 50 (2006) 437-468.

[23] C.S. Peskin, Numerical analysis of blood flow in the heart, Journal of Computational Physics, 25 (1977) 220-252.

[24] C.S. Peskin, The immersed boundary method, Acta Numerica, 11 (2003) 479-517.

[25] R. Mittal, G. Iaccarino, Immersed Boundary Methods, Annual Review of Fluid Mechanics, 37 (2005) 239-261.

[26] T. Dunne, An Eulerian approach to fluid-structure interaction and goal-oriented mesh adaptation, International Journal for Numerical Methods in Fluids, 51 (2006) 1017-1039.

[27] T. Richter, A Fully Eulerian formulation for fluid–structure-interaction problems, Journal of Computational Physics, 233 (2013) 227-240.

[28] S. Ii, X. Gong, K. Sugiyama, J. Wu, H. Huang, S. Takagi, A Full Eulerian Fluid-Membrane Coupling Method with a Smoothed Volume-of-Fluid Approach, Communications in Computational Physics, 12 (2015) 544-576.

[29] P. He, R. Qiao, A full-Eulerian solid level set method for simulation of fluid–structure

interactions, Microfluidics and Nanofluidics, 11 (2011) 557-567.

[30] K. Kamrin, C.H. Rycroft, J.-C. Nave, Reference map technique for finite-strain elasticity and fluid–solid interaction, Journal of the Mechanics and Physics of Solids, 60 (2012) 1952-1969.

[31] P. Sun, J. Xu, L. Zhang, Full Eulerian finite element method of a phase field model for fluid–structure interaction problem, Computers & Fluids, 90 (2014) 1-8.

[32] J. Gattu, H. Ki, Computation of flow-induced stresses in a structure using a hybrid momentum equation approach, International Journal of Theoretical and Applied Multiscale Mechanics, 1 (2009) 118-133.

[33] H. Yeo, H. Ki, A Unified Momentum Equation Approach for Computing Flow-Induced Stresses in Structures with Arbitrarily-Shaped Stationary Boundaries, Communications in Computational Physics, 22 (2017) 39-63.

[34] H. Yeo, H. Ki, A unified momentum equation approach for computing thermal residual stresses during melting and solidification, Computer Physics Communications, 224 (2018) 230-244.

[35] H. Yeo, H. Ki, Unified momentum equation approach for fluid–structure interaction problems involving linear elastic structures, Journal of Computational Physics, 415 (2020).

[36] S.A. Tsirkas, P. Papanikos, T. Kermandis, Numerical simulation of the laser welding process in butt-joint specimens, Journal of Materials Processing Technology, 134 (2003) 59-69.

[37] N.S. Bailey, W. Tan, Y.C. Shin, Predictive modeling and experimental results for residual stresses in laser hardening of AISI 4140 steel by a high power diode laser, Surface and Coatings Technology, 203 (2009) 2003-2012.

[38] F. Kong, S. Santhanakrishnan, R. Kovacevic, Numerical modeling and experimental study of thermally induced residual stress in the direct diode laser heat treatment of dual-phase 980 steel, The International Journal of Advanced Manufacturing Technology, 68 (2013) 2419-2430.

[39] M. Yaakoubi, M. Kchaou, F. Dammak, Simulation of the thermomechanical and metallurgical behavior of steels by using ABAQUS software, Computational Materials Science, 68 (2013) 297-306.

[40] Y. Chew, J.H.L. Pang, G. Bi, B. Song, Thermo-mechanical model for simulating laser cladding induced residual stresses with single and multiple clad beads, Journal of Materials Processing Technology, 224 (2015) 89-101.

[41] J.X. Fang, S.Y. Dong, Y.J. Wang, B.S. Xu, Z.H. Zhang, D. Xia, P. He, The effects of solid-state phase transformation upon stress evolution in laser metal powder deposition, Materials & Design, 87 (2015) 807-814.

[42] N. Nazemi, J. Urbanic, M. Alam, Hardness and residual stress modeling of powder injection laser cladding of P420 coating on AISI 1018 substrate, The International Journal of Advanced Manufacturing Technology, 93 (2017) 3485-3503.

[43] M. Zain-ul-abdein, D. Nélias, J.-F. Jullien, D. Deloison, Experimental investigation and finite

element simulation of laser beam welding induced residual stresses and distortions in thin sheets of AA 6056-T4, Materials Science and Engineering: A, 527 (2010) 3025-3039.

[44] E.D. Derakhshan, N. Yazdian, B. Craft, S. Smith, R. Kovacevic, Numerical simulation and experimental validation of residual stress and welding distortion induced by laser-based welding processes of thin structural steel plates in butt joint configuration, Optics & Laser Technology, 104 (2018) 170-182.

[45] J. Ahn, E. He, L. Chen, R.C. Wimpory, S. Kabra, J.P. Dear, C.M. Davies, FEM prediction of welding residual stresses in fibre laser-welded AA 2024-T3 and comparison with experimental measurement, The International Journal of Advanced Manufacturing Technology, 95 (2018) 4243-4263.

[46] M. Sussman, P. Smereka, S. Osher, A level set approach for computing solutions to incompressible two-phase flow, Journal of Computational Physics, 114 (1994) 146-159.

[47] S.V. Patankar, Numerical heat transfer and fluid flow, (1980).

[48] U. Ghia, K.N. Ghia, C.T. Shin, High-Re solutions for incompressible flow using the NavierStokes equations and a multigrid method, Journal of Computational Physics, 48 (1982) 387-411.

[49] R. Glowinski, G. Guidoboni, T.W. Pan, Wall-driven incompressible viscous flow in a two-dimensional semi-circular cavity, Journal of Computational Physics, 216 (2006) 76-91.

[50] O. Desjardins, V. Moureau, H. Pitsch, An accurate conservative level set/ghost fluid method for simulating turbulent atomization, Journal of Computational Physics, 227 (2008) 8395-8416.

[51] E. Olsson, G. Kreiss, A conservative level set method for two phase flow, Journal of Computational Physics, 210 (2005) 225-246.

[52] E. Olsson, G. Kreiss, S. Zahedi, A conservative level set method for two phase flow II, Journal of Computational Physics, 225 (2007) 785-807.

[53] T.D. Aslam, A partial differential equation approach to multidimensional extrapolation, Journal of Computational Physics, 193 (2004) 349-355.

[54] J.A. Sethian, Level Set Methods and Fast Marching Methods, second ed., Cambridge University Press, Cambridge, UK, (1999).

[55] E. Hachem, S. Feghali, R. Codina, T. Coupez, Anisotropic adaptive meshing and monolithic Variational Multiscale method for fluid–structure interaction, Computers & Structures, 122 (2013) 88-100.

[56] Z. Yu, A DLM/FD method for fluid/flexible-body interactions, Journal of Computational Physics, 207 (2005) 1-27.

[57] X. Wang, C. Wang, L.T. Zhang, Semi-implicit formulation of the immersed finite element method, Computational Mechanics, 49 (2011) 421-430.

[58] X. Wang, L.T. Zhang, Modified Immersed Finite Element Method For Fully-Coupled Fluid-Structure Interations, Comput Methods Appl Mech Eng, 267 (2013).

[59] S. Frei, Eulerian finite element methods for interface problems and fluid–structure interactions (Ph.D. thesis), University of Heidelberg, (2016).

[60] D. Deng, FEM prediction of welding residual stress and distortion in carbon steel considering phase transformation effects, Materials & Design, 30 (2009) 359-366.

[61] N.E. Dowling, Mechanical Behavior of Materials (4th Edition), Pearson, Boston, MA, (2012).

[62] C.-H. Lee, K.-H. Chang, Prediction of residual stresses in high strength carbon steel pipe weld considering solid-state phase transformation effects, Computers & Structures, 89 (2011) 256-265.

[63] A.H. Yaghi, T.H. Hyde, A.A. Becker, W. Sun, Finite element simulation of welding and residual stresses in a P91 steel pipe incorporating solid-state phase transformation and post-weld heat treatment, The Journal of Strain Analysis for Engineering Design, 43 (2008) 275-293.

[64] D.P. Koistinen, R.E. Marburger, A general equation prescribing the extent of the austenite-martensite transformation in pure iron-carbon alloys and plain carbon steels, Acta Metallurgica, 7 (1959) 59-60.

[65] J.C. Simo, T.J.R. Hughes, Computational Inelasticity, Springer, Berlin Heidelberg New York, (1998).

[66] C.R. Swaminathan, V.R. Voller, A general enthalpy method for modeling solidification processes, Metallurgical Transactions B: Process Metallurgy, 23 (1992) 651-664.

[67] H. Ki, P.S. Mohanty, J. Mazumder, Modeling of laser keyhole welding: Part I. Mathematical modeling, numerical methodology, role of recoil pressure, multiple reflections, and free surface evolution, Metallurgical and Materials Transactions A-Physical Metallurgy and Materials Science, 33 (2002) 1817-1830.

[68] B. Taljat, B. Radhakrishnan, T. Zacharia, Numerical analysis of GTA welding process with emphasis on post-solidification phase transformation effects on residual stresses, Materials Science and Engineering A, 246 (1998) 45-54.

[69] F. Hosseinzadeh, J. Kowal, P.J. Bouchard, Towards good practice guidelines for the contour method of residual stress measurement, The Journal of Engineering, 2014 (2014) 453-468.

[70] M.B. Prime, Cross-sectional mapping of residual stresses by measuring the surface contour after cut, Journal of Engineering Materials and Technology, 123 (2001) 162-168.

[71] J. Cheon, S.-J. Na, Prediction of welding residual stress with real-time phase transformation by CFD thermal analysis, International Journal of Mechanical Sciences, 131-132 (2017) 37-51.

[72] F.D. Fischer, G. Reisner, E. Werner, K. Tanaka, G. Cailletaud, T. Antretter, A new view on transformation induced plasticity (TRIP), International Journal of Plasticity, 16 (2000) 723-748.

[73] Y. Nagasaka, J.K. Brimacombe, E.B. Hawbolt, I.V. Samarasekera, B. Hernandez-Morales, S.E.

Chidiac, Mathematical model of phase transformations and elasto-plastic stress in the water spray quenching of steel bars, Metallurgical Transactions A, 24 (1993) 795-808.

[74] J. Cheon, D.V. Kiran, S.-J. Na, Thermal metallurgical analysis of GMA welded AH36 steel using CFD–FEM framework, Materials & Design, 91 (2016) 230-241.

[75] J. Cheon, D.V. Kiran, S.-J. Na, CFD based visualization of the finger shaped evolution in the gas metal arc welding process, International Journal of Heat and Mass Transfer, 97 (2016) 1-14.

[76] S. Oh, H. Ki, Prediction of hardness and deformation using a 3-D thermal analysis in laser hardening of AISI H13 tool steel, Applied Thermal Engineering, 121 (2017) 951-962.

[77] X. Richard Zhang, X. Xu, Finite element analysis of pulsed laser bending: The effect of melting and solidification, Journal of Applied Mechanics, 71 (2004) 321-326.

[78] J. Sengupta, S.L. Cockcroft, D.M. Maijer, A. Larouche, Quantification of temperature, stress, and strain fields during the start-up phase of direct chill casting process by using a 3D fully coupled thermal and stress model for AA5182 ingots, Materials Science and Engineering: A, 397 (2005) 157-177.